School of Science and Engineering
Department of Imaging and Applied Physics
Curtin Institute of Radio Astronomy
International Centre for Radio Astronomy Research

The High Time Resolution Dynamic Radio Sky

Divya Palaniswamy

This thesis is presented for the Degree of
Master of Philosophy (Physics)
of
Curtin University

November 2014

To the best of my knowledge and belief this thesis contains no material previously published by any other person except where due acknowledgement has been made. This thesis contains no material which has been accepted for the award of any other degree or diploma in any university.

Divya Palaniswamy

Preface

The research work and the papers produced during the course of this MPhil have had due contributions from my supervisors and co-authors. The observations presented in this thesis were made using the 26 m radio telescope located at the Mount Pleasant Radio Observatory operated by University of Tasmania.

Publications directly resulting from the work done for this thesis is as follows:

D. Palaniswamy, R. B. Wayth, C. M. Trott, J. N. McCallum, S. J. Tingay, and C. Reynolds (2014). A search for fast radio bursts associated with gamma-ray bursts. The Astrophysical Journal 790 (1), 63.

Other publications during the course of my MPhil are:

D. Palaniswamy, N. D. R. Bhat, S. J. Tingay, S. Ellingsen, R. B. Wayth, C. M. Trott. Detection of radio pulsations at 22 GHz from the Magnetar PSR J1745-2900 in the archival data from 2011. Astronomers Telegram, May 2013.

C. M. Trott, S. J. Tingay, R. B. Wayth, D. R. Thompson, A. T. Deller, W. F. Brisken, K. L. Wagstaff, W. A. Majid, S. Burke-Spolaor, J.-P. R. Macquart, and **D. Palaniswamy** (2013, April). A Framework for Interpreting Fast Ra- dio Transients Search Experiments: Application to the V-FASTR Experiment. 767, 4.

D. R. Thompson, S. Burke-Spolaor, A. Deller, W. A. Majid, **D. Palaniswamy**, S. J. Tingay, K. L. Wagstaff, R. B. Wayth: Real-Time Adaptive Event Detection in Astronomical Data Streams. IEEE Intelligent Systems 29(1): 48-55 (2014).

Acknowledgements

It is a great pleasure to convey my gratitude to all who have given their invaluable support, both professional and personal, through the journey of my postgraduate school. First and foremost, I would like to thank my supervisors Professor. Steven Tingay, Dr. Randall Wayth and Dr. Cathryn Trott for giving me the opportunity to work at the Curtin University and ICRAR. Their patience and guidance were invaluable with what turned out to be a more challenging project than I first supposed! Its being a privilege to work with them.

This thesis would not be possible without the work and effort put forth by Dr. Jamie McCallum and Dr. Simon Ellingsen from University of Tasmaina, who scheduled the observations and data aggregation for the research presented in this thesis. I would also like to extend my thanks to Stuart Weston and team for setting up the 12 m radio dish for GRB observations at Warkworth Radio Observatory. I am very grateful for their work, time and effort. A special thanks to Dr. Cormac Reynolds, for countless discussions, helpful tips on analysis of the data and thoughtful advice.

I am also thankful to many others in ICRAR and other institutions, with whom I had the pleasure of discussing my work through random discussions in the corridor or in official meetings. In particular, I thank Dr. Jean-Pierre Macquart and Dr. N. D. Ramesh Bhat for useful discussions on FRBs, Pulsars and Magnetars; Dr. Peter Curran for useful discussions and suggestion on the GRB X-ray light curves and analysis; Aidan Hotan and Bruce Stansby for providing the Vela data. I also thank Dr. Steve Ord, Dr. Hayley Bignall, Dr. Nadia Kudryavtseva and Dr. Nathan Clarke for useful discussions.

A warm thanks to all my fellow postgraduate students past and present, including Hayden Rampadarath, Jun Yi Koay (Kevin), Aziz Jiwani, Chittawan Choeysakul, Tim Colegate, John Goldsmith, Bruce Stansby, Samuel Oronsaye,

Balwinder Arora Singh and Thomas Russell. A special thanks to Tanya Jones, Rachel Kennedy, Tina Sallis, Angela Dunleavy, Roselina Stone and Emily Bromfield for excellent administrative support. I appreciate Kirsten Gottschalk and Pete Wheeler for giving me an opportunity to be involved in outreach activities. A very special thanks to John Goldsmith who helped me discover my passion for photography and for teaching me some of the basic aspects of astrophotography.

And, of course, I could have not made through this journey without the love and support from family and lifetime friends. Dr. Soobash Daiboo thanks to you, for having seen me through thick and thin. Dad, thanks for your encouragement and Mom, thanks for listening and being supportive even when I am speaking of most foreign things. Thanks also to my siblings Naveen, Nandish and Deepthi for being there for me.

I would like to acknowledge the Curtin University for providing the financial support through the Curtin Strategic International Research Scholarship. I have made use of various resources during my work, including the 26 m radio telescope located at the Mount Pleasant Radio Observatory, the Swift Science Data Centre located at the University of Leicester, UK; the Curtin University Parallel Processor for Astronomy (CUPPA) located at Curtin University for data processing. This study was also supported by iVEC through the use of advanced computing resources located at iVEC@Curtin.

Abstract

This thesis mainly focuses on searches for Fast Radio Bursts (FRBs). FRBs are short duration ($\sim$ 1 ms), highly dispersed radio pulses from astronomical sources. The physical interpretation for FRBs remains unclear, but is thought to involve highly compact objects hosted in galaxies at cosmological distances. We have conducted targeted experiments of extragalactic sources and Galactic regions, searching for the characteristic signatures of FRBs. This thesis summarises the outcomes of the present work, challenges faced, and methodologies developed to meet those challenges.

The first part of this thesis we discuss the observations of Gamma-ray Bursts (GRBs) and the search for FRBs associated with GRBs. Detections for eight Fast Radio Bursts (FRBs) have recently been reported. It has been suggested that a fraction of FRBs could be physically associated with GRBs. Recent radio observations of GRBs have reported the detection of two highly-dispersed short duration radio pulses using a 12 m radio telescope at 1.4 GHz. Motivated by this result, we have performed a systematic and sensitive search for FRBs associated with GRBs. We have observed five GRBs at 2.3 GHz using a 26 m radio telescope located at the Mount Pleasant Radio Observatory, Hobart. The radio telescope was automated to rapidly respond to Gamma-ray Coordination Network notifications from the Swift satellite and slew to the GRB position within $\sim$ 140 s. The data were searched for pulses up to 5000 pc cm^{-3} in dispersion measure and pulse widths ranging from 640 μs to 25.60 ms. We did not detect any events $\geq 6\sigma$. A statistical analysis of our data shows that events detected above 5σ are consistent with thermal noise fluctuations. A joint analysis of our data with previous experiments shows that previously claimed detections of FRBs from GRBs are unlikely to be astrophysical. Our results are in line with the lack of consistency noted between the recently presented FRB event rates and GRB event rates.

Finally, we report results from a survey at 22 GHz searching for FRBs within the central parsec of our Galaxy using the 26 m Hobart radio telescope. This is the highest frequency used to search for FRBs at the Galactic Centre to date. Six hours of data were searched for pulses up to a dispersion measure of 10000 $\mathrm{pc\,cm^{-3}}$ and pulse widths ranging from $64\mu\mathrm{s} - 4\mathrm{ms}$ covering a substantial search volume for FRBs. We detected three events above our 6σ detection threshold. An analysis of the events indicates no convincing evidence that the events are astrophysical.

Contents

List of Figures

List of Tables

Chapter 1

Introduction

What is actual is actual only for one time. And only for one place.
-T. S. Eliot

1.1 Motivation for the Present Work

One frontier for observational astrophysics is the temporal domain with high time resolution (of order milliseconds - seconds), where the physics and astrophysics of compact objects and dynamic regions in the Universe are probed. Varied techniques and approaches to observing the dynamic Universe have produced new and sometimes surprising results. For instance, increasing observation time, field-of-view, and temporal resolution has led to the discovery of pulsars (Hewish et al., 1968), Rotating Radio Transients (RRATs: McLaughlin et al. (2006)), and giant pulses (Lundgren et al., 1995). One of the most exciting discoveries in recent times has been detections of isolated, single, short duration, highly dispersed bursts of radio emission from unknown progenitors hosted in galaxies at cosmological distances. These events have popularly become known as Fast Radio Bursts (FRBs: Thornton et al. (2013)).

In this thesis, we focus our research on searching for FRBs from our Galaxy and extragalactic objects. The first part of this thesis focuses on the search for FRBs possibly associated with gamma-ray bursts (GRBs). The second part of this thesis focuses on the search for FRBs from the central parsec of our Galaxy.

In the following sections an overview of the motivations behind this thesis is given, with introductory material related to FRBs, GRBs, and other aspects of this field. An overview of the scope of the thesis is also provided.

1.2 The Dynamic Radio Sky

Some objects in the Universe are variable and violent in nature. Over previous decades, astronomers have observed a range of objects that show recurrent or transient variability; some classes of object exhibit both quiescent and bursting behaviours (Camilo et al., 2006) and other classes exhibit brief single outbursts (Ghirlanda et al., 2006). These time variable objects are popularly known as transients - bursts, flares and pulses that occur on time scales measured from fractions of a second to months. Transients occur where extreme physical conditions exist. At radio wavelengths, transients provide an opportunity to probe the environments of the transient objects and to study the behaviour of the objects themselves (Cordes et al., 2004; Macquart, 2011; Cordes, 2013).

A number of non-repeating fast transients have been detected at radio wavelengths (McLaughlin et al., 2006; Lorimer et al., 2007; Keane et al., 2012; Thornton et al., 2013; Spitler et al., 2014). However, transients remain largely unexplored at radio wavelengths, due to the very large parameter space they may occupy and the need for monitoring observations over a wide range of cadences (Bhat, 2011). The lack of continuous all-sky monitoring capabilities, long term targeted surveys, limited fields-of-view, and the massive amount of signal processing required, have hindered the detection and characterisation of radio transients. However, the current state-of-the-art in radio telescope technology represents a significant advance in recent years. On-going advances in communication and information technologies and high performance computing techniques have overcome some of these limitations. Current and future telescopes at radio wavelengths such as: the Karl G. Jansky Very Large Array (JVLA; EVLA Perley et al. (2011)); the Westerbork Synthesis Radio Telescope focal plane array, (Apertif Verheijen et al. (2008)); the Very Large Baseline Array (VLBA; Napier et al. (1994); Stankiewicz (2010)); the Parkes radio telescope (Staveley-Smith et al., 1996); the Murchison Widefield Array (MWA; Tingay et al. (2013)); and the Low Frequency Array (LOFAR; van Haarlem et al. (2013)), have demonstrated significant capabilities for processing massive datasets, performing continuous observations, obtaining instantaneous wide fields-of-view and achieving better sensitivity, leading to better exploration of the dynamic radio sky.

Radio transients are broadly classified into *fast* and *slow* (Figure 1.1). The former are usually defined as lasting $\lesssim 1\,s$ and the latter are defined as lasting $\gtrsim 1\,s$. Slow transients are usually found by conventional imaging techniques (for example Bell et al. (2014)), while fast transients are most commonly found by

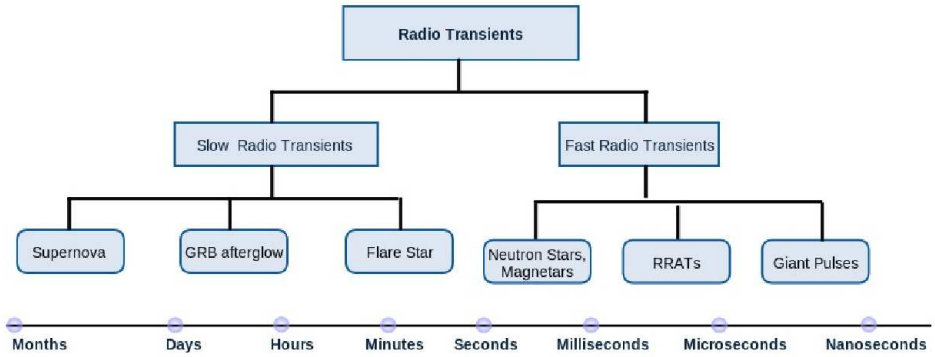

Figure 1.1: The dynamic radio sky is divided into two classes based on duration: "slow" radio transients; and "fast" radio transients. Events that occur on timescales of days to months like supernovae and GRB afterglows are classified as slow radio transients. Events that occur on timescales ranging from seconds to fractions of seconds like pulses from pulsars, magnetars, RRATs and giant pulses are classsifed as fast radio transients.

analysing the high time resolution time-series data (for example Wayth et al. (2011)). Transients can also be classified based on emission mechanism: short radio transients are known to originate from coherent processes; while the longer-lived radio transients are due to incoherent processes (Bhat, 2011). Figure 1.2 shows a clear distinction in the transient emission process. The boundary between the coherent and incoherent emission is $\sim 10^{12}$K, due to inverse Compton cooling (Readhead, 1994). Flare stars (Richards et al., 2003), Supernovae (Weiler et al., 2010) and GRB afterglows (Gehrels et al., 2009) are examples of slow radio transients that exhibit variations over long durations. The well-known examples for fast radio transients are pulsars (Hewish et al., 1968) and related phenomena such as RRATs (McLaughlin et al., 2006), giant pulses (Lundgren et al., 1995), and magnetar flares (Camilo et al., 2006) which are Galactic in origin. In the past few years, there has been a growing number of detections of fast radio transients. The detection of eight isolated highly dispersed radio pulses has sparked high interest in the field (Lorimer et al., 2007; Keane et al., 2012; Thornton et al., 2013; Spitler et al., 2014; Burke-Spolaor and Bannister, 2014). Thornton et al. (2013) coined the term Fast Radio Burst (FRB). In this work I concern myself only with FRBs.

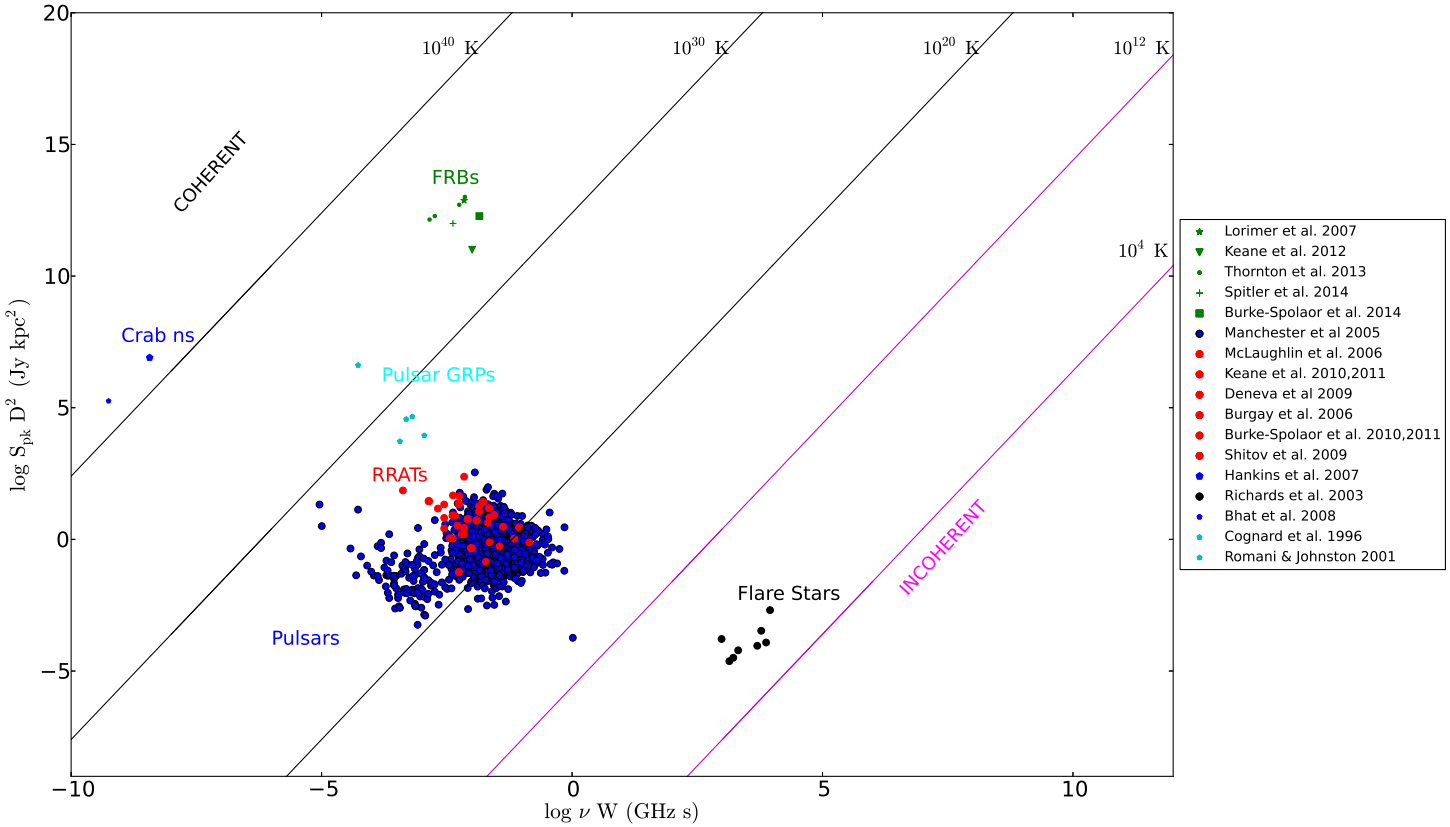

Figure 1.2: The transient phase space of known transients. This is a plot of radio luminosity $L = S\,D^2$ verses $\nu\,W$, where S is the flux density, D is the distance, ν is the observing frequency and W is the pulse width. The lines represent the constant minimum brightness temperature, $T_B = SD^2/2k(\nu W)^2$ K, where k is the Boltzmann constant. Due to inverse Compton cooling, the boundary between coherent and incoherent emission is $\sim 10^{12}$ K (Readhead, 1994). Plotted are pulsars (Manchester et al., 2005), RRATs (McLaughlin et al., 2006; Shitov et al., 2009; Burgay et al., 2006; Deneva et al., 2009; Keane et al., 2010; Burke-Spolaor and Bailes, 2010; Burke-Spolaor et al., 2011), pulsar 'giant radio pulses' (Cognard et al., 1996; Romani and Johnston, 2001), FRBs (Lorimer et al., 2007; Keane et al., 2012; Thornton et al., 2013; Spitler et al., 2014; Burke-Spolaor and Bannister, 2014), Crab giant pulses (Hankins and Eilek, 2007; Bhat et al., 2008), and Flare stars (Richards et al., 2003).

1.2.1 Fast Radio Bursts

FRBs are short duration ($\sim$ ms), highly dispersed radio pulses from astronomical sources (Lorimer et al., 2007; Keane et al., 2012; Thornton et al., 2013; Spitler et al., 2014; Burke-Spolaor and Bannister, 2014). The physical interpretation of FRBs remains unclear. Figure 1.3 shows the positions on the sky of all eight FRBs detected so far, as a function of dispersion measure (DM pc cm^{-3}) and Galactic latitude ($|\mathrm{b}|^{\circ}$) (Manchester et al., 2005; Lorimer et al., 2007; Keane et al., 2012; Thornton et al., 2013; Spitler et al., 2014; Burke-Spolaor and Bannister, 2014). The characteristics of the FRBs detected thus far can be summarised as follows:

- They are one-off events, no repeated bursts have been reported at the same position thus far;
- The dispersion measures are high, DM $\gtrsim 300 - 1000\,\mathrm{pc\,cm^{-3}}$, implying that FRBs are at cosmological distances, with redshifts $z > 0.5 - 1$;
- The typical flux density is $\mathrm{S}_{\nu} \sim$ Jy, implying energies of $\sim 10^{38} - 10^{40}\,\mathrm{erg}$, assuming isotropic emission;
- The typical widths are $\delta t \sim ms$, which indicates that the emission regions are highly compact, $\mathrm{c}\delta\mathrm{t}(1+\mathrm{z})^{-1} \lesssim 1500(1+\mathrm{z})^{-1}$ km (here we assume $\delta\mathrm{t} = 5\,\mathrm{ms}$);
- No progenitor or host galaxy counterparts have been identified, as the FRBs have never been adequately localised.

Identifying FRBs and their progenitors offers potential insights into a variety of astrophysical phenomena such as: stellar evolution (Cordes et al., 2004); understanding the extreme states of matter (Cordes et al., 2004); detecting and probing the intervening medium (Macquart and Koay, 2013); mechanisms of particle accelerations (Cordes et al., 2004); possibility of Extraterrestrial civilizations (Cordes et al., 2004); or perhaps identification of a new class of compact objects (Cordes, 2013).

The Discovery of FRBs

In 2001, a systematic survey was performed to search for radio pulsars in the Magellanic Clouds (Manchester et al., 2006) using the 20 cm multi-beam receiver installed on the Parkes radio telescope. In 2007, Lorimer et al. (2007) re-processed

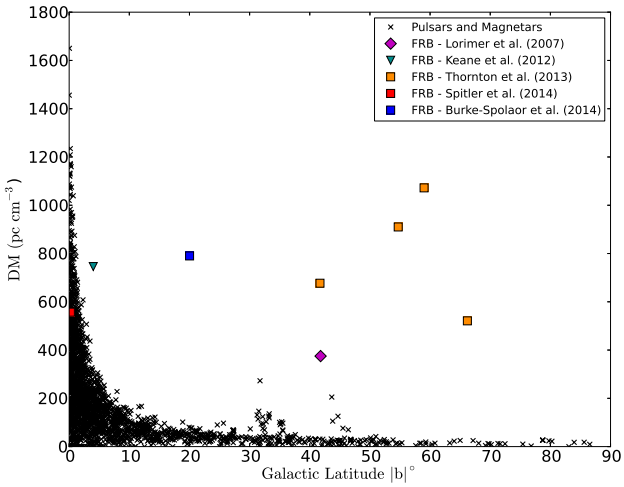

Figure 1.3: The distribution of the normal pulsars (black crosses) (Manchester et al., 2005) and eight FRBs reported by Lorimer et al. (2007); Keane et al. (2012); Thornton et al. (2013); Spitler et al. (2014); Burke-Spolaor and Bannister (2014).

the data, searching for single, dispersed pulses, and reported the discovery of an unusual short duration radio pulse; they discovered a single pulse of duration $\sim$ 5 ms at a DM of 375 pc cm^{-3} (Figure 1.4a). The high dispersion measure of the pulse implies the source of the burst to be at a cosmological distance. The observed width (δt $\sim$ 5 ms) of the pulse indicated that the emission region was highly compact. The total emitted energy of the burst was estimated at $\sim 10^{40}$ ergs, assuming the distance is cosmological and the emission from the source was isotropic. Lorimer et al. (2007) inferred an event rate of 50 day^{-1} Gpc^{-3}, assuming an isotropic distribution of the sources on the sky and proposed that the implied rates of occurrence were compatible with GRB rates. However, there are no recorded GRB events near the pulse location.

In the meantime, a similar single pulse was discovered by Keane et al. (2012) from archival data (Manchester et al., 2001) recorded with the same telescope. The pulse properties were similar to those reported by Lorimer et al. (2007), with a short time scale ($\sim$ 7 ms) and high DM (745 pc cm^{-3}). Figure 1.4b shows the pulse as a function of observing time and frequency. Recent analysis of the pulse has suggested it is Galactic in origin (Bannister and Madsen, 2014a).

Recently, four highly dispersed pulses have been detected at Parkes by Thornton et al. (2013). The FRBs were detected with DMs in the range 553 to 1103

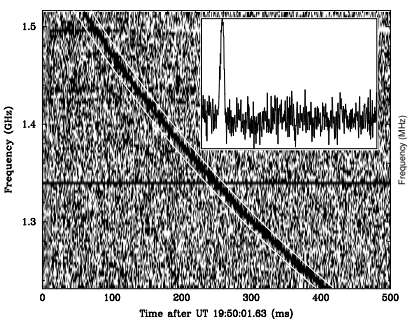

(a) Lorimer et al. (2007)

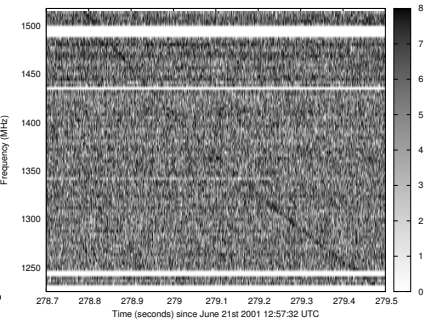

(b) Keane et al. (2012)

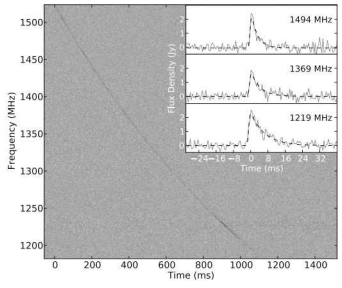

(c) Thornton et al. (2013)

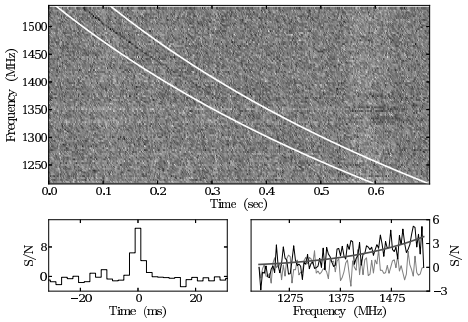

(d) Spitler et al. (2014)

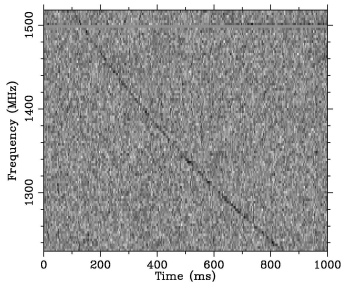

(e) Burke-Spolaor and Bannister (2014)

Figure 1.4: a: The dynamic spectrum (power in each spectral and temporal channel) of the highly dispersed single radio pulse (FRB) detected by Lorimer et al. (2007); b: The dynamic spectrum for the single radio pulse detected by Keane et al. (2012). Figure from (Keane et al., 2012); c: The dynamic spectrum of the FRB detected by Thornton et al. (2013). Figure from (Thornton et al., 2013); d: top panel: Dynamic spectrum for the FRB discovered by Spitler et al. (2014). Lower left panel shows the dedispersed pulse profile averaged across the bandpass and lower right panel compares the on-pulse spectrum (black) with an off-pulse spectrum (light grey), and for reference a curve showing the fitted spectral index ($\alpha = 10$) is also overplotted (medium grey). Figure from Spitler et al. (2014); e: Dynamic spectrum for the FRB discovered by Burke-Spolaor and Bannister (2014). Figure from Burke-Spolaor and Bannister (2014).

pc cm^{-3} (Figure 1.4c). Based on their properties, Thornton et al. (2013) infer an FRB event rate (R_{FRB}) to be $10^{-3}\,yr^{-1}\,galaxy^{-1}$ in the comoving sample volume which contains $\sim 10^9$ late type galaxies, which is $\sim 10^3$ times larger than GRB rates ($R_{GRB} = 10^{-6}\,yr^{-1}\,galaxy^{-1}$). Using the inconsistency in the event rates and, in particular, with no known GRB events coincident with the FRBs, Thornton et al. (2013) rules out GRBs as possible progenitors for most FRBs.

All six FRBs mentioned above were detected by the 64-m Parkes radio telescope and its 13-beam receiver. Recently, Spitler et al. (2014) reported the discovery of another highly dispersed pulse by the 300 m Arecibo radio telescope. This pulse is the first FRB discovered from a geographical location other than Parkes. This FRB was found at low Galactic latitude ($b = -0°.2$) with a DM of 557.4 pc cm^{-3} and pulse width ~ 3 ms. Despite the low Galactic latitude, the high DM suggests an extragalactic origin.

Most recently, Burke-Spolaor and Bannister (2014) reported a new FRB detection in archival Parkes radio telescope data (Edwards et al., 2001a; Jacoby et al., 2009a). The FRB was detected at a Galactic latitude of $b = -20°.021$ with a DM of 790 pc cm^{-3} and a pulse width ~ 9.4 ms.

Perytons

Some doubts on the extragalactic origin of the pulses have been put forward, based on the work of Burke-Spolaor et al. (2011), with the detection of 16 similar highly dispersed pulses from Parkes archive data (Edwards et al., 2001b; Roberts et al., 2002; Crawford et al., 2007; Jacoby et al., 2009b), all deemed as terrestrial in origin (Figure 1.5). However, the source of the events of terrestrial origin are not yet known. Burke-Spolaor et al. (2011) called these terrestrial events "Perytons". Perytons were deemed as terrestrial in origin because, unlike FRBs, Perytons were detected in all 13 beams of the Parkes radio telescope multi-beam receiver and their pulse widths disagree by a factor of ~ 2 (which cannot be accounted for by multi-path scatter broadening) compared with pulse widths of FRBs. The recent results of Thornton et al. (2013) provide excellent evidence that the FRBs are astronomical in origin and are not related to the Perytons.

1.3 Scope of the Thesis

The main aim of this thesis is to search for FRBs associated with GRBs and in the direction of the Galactic Centre, in an attempt to detect FRBs. For this thesis we

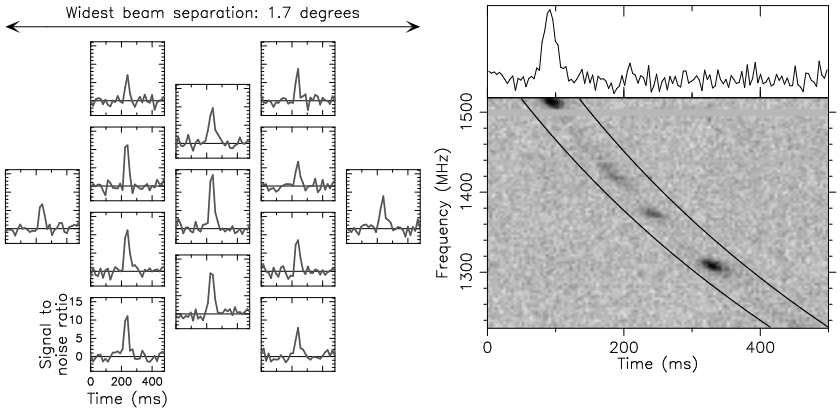

Figure 1.5: Left panel - The dedispersed time series showing Perytons in all the 13 beams of 64-m Parkes radio telescope. Right panel - Dedispersed time series and dynamic spectrum of a Peryton. Figure from (Burke-Spolaor et al., 2011).

utilised the capabilities of existing radio telescopes to perform the observations.

The facility used in this project is the radio telescope located at the Mount Pleasant Radio Observatory operated by University of Tasmania[1] near Hobart, Tasmania. The Mount Pleasant Radio Observatory hosts a 26-m radio telescope. The telescope is equipped with a variety of receivers which operate between 660 MHz and 22 GHz. The large number of available receivers makes the telescope suitable for a variety of research projects.

The FRBs detected so far have been detected by the 64-m Parkes radio telescope and the 300 m Arecibo radio telescope at GHz frequencies (Lorimer et al., 2007; Keane et al., 2012; Thornton et al., 2013; Spitler et al., 2014; Burke-Spolaor and Bannister, 2014). Due to the limited angular resolution of the radio telescopes, the eight FRBs thus far detected could not be localised or associated with a progenitor or host galaxy. Numerous physical mechanisms have been proposed to explain the existence of FRBs, for example GRBs (Lorimer et al., 2007; Zhang, 2013), evaporation of primordial black holes (Keane et al., 2012), magnetar giant flares (Popov and Postnov, 2007; Thornton et al., 2013), accretion induced collapse of a isolated and magnetised supermassive rotating neutron stars into Black Holes (Falcke and Rezzolla, 2013), and binary neutron star mergers (Totani, 2013). However solid relationships between FRBs and proposed progenitor mechanisms have not been established.

[1] www.ra-wiki.phys.utas.edu.au

1.3.1 Searching for FRBs from Gamma-ray Bursts

Gamma-ray Bursts (GRBs) are among the most powerful objects in the Universe. The energy output in the γ-rays is in the order of 10^{51} ergs (assuming isotropic emission) on second time-scales at cosmological distances (Rees and Meszaros, 1994; Ghirlanda et al., 2006). The first GRB was detected by the γ-ray and X-ray detectors on the Vela satellite, which was originally developed and launched to detect nuclear explosions on Earth from space. For many years it was not known if these bursts were local or cosmic in origin. A few years later Klebesadel et al. (1973) reported on 16 GRBs, observed between July 1969-1972, of cosmic origin. Figure 1.6 shows an artist's illustration of a bright GRB occurring in a star formation region.

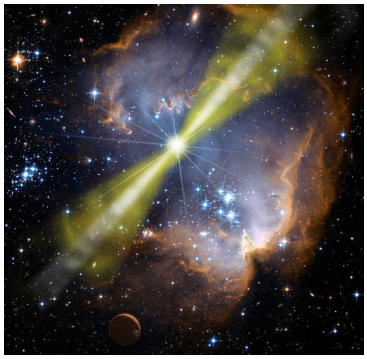

Figure 1.6: Artists illustration of the bright GRB occurring in a star formation region. Photo Credit: NASA/Swift/Mary Pat Hrybyk-Keith and John Jones

A great breakthrough came to the field of GRBs with the launch of the Compton Gamma Ray observatory (CGRO) in April 1991, which carried the Burst and Transient Source Experiment (BATSE), designed to detect GRBs. The two main advances that resulted from BATSE were: (1) the identification of two different populations of GRBs, based on duration and spectral hardness[2](Kouveliotou et al., 1993); and (2) evidence that GRBs are distributed isotropically and homogeneously across the sky (Kouveliotou et al., 1993). In 2004, NASA launched the Swift satellite, its fast slewing capabilities allowing the study of more distant objects, giving rise to a more detailed picture of the evolution of the GRB afterglow emission.

[2]The hardness of X-ray is defined as its penetrating ability. It depends on the wavelength of the X-rays not on the number of X-ray photons. The hardness ratios are commonly used in X-ray photometry to indicate spectral properties. They are usually defined as the ratio of counts in two different wave bands.

Types of GRBs

Two classes of GRBs were identified from the first BATSE catalogue based on duration and X-ray spectral hardness. The catalogue showed a bimodality in the distribution of their durations, which was defined by T_{90} (Kouveliotou et al., 1993), the time during which the cumulative counts in the detector increases from 5% to 95% above the background rate. Therefore, based on the bimodal distribution of the duration obtained from the catalogue, the bursts were separated into long GRBs ($\geq$ 2s) and short GRBs ($\leq$ 2s). The X-ray spectral hardness ratios for the short GRBs were seen to be predominately high while the long GRBs were low. Therefore from the temporal and spectral properties of these bursts, they were naturally separated into *short-hard* GRBs and *long-soft* GRBs.

The short GRBs are thought to originate from the merger of two compact objects, such as neutron star - neutron star (NS-NS) or neutron star - black hole (NS-BH) pairs. Figure 1.7 demonstrates the evolution of the compact binary NS merger leading to short GRB. Figure 1.7 is modified from Bartos et al. (2013). NS-NS binary in-spirals may be observable for a few seconds to minutes. Upon merging, binaries with total mass $M_{binary} > 3M_{\odot}$ promptly collapse into a Black Hole, if $M_{NS1} = M_{NS2}$. For non-equal mass NS binaries ($M_{NS1} \neq M_{NS2}$), the BH will be surrounded by an accretion disk (Rezzolla et al., 2010). The NS binaries with mass $M_{NS,max} < M_{binary} < 3M_{\odot}$ form a hyper-massive NS with strong differential rotation. The hyper-massive NS survives for a few milliseconds to a second and eventually collapses into a BH, potentially with a accretion disk. Very low mass binaries could form a stable NS or a Magnetar (Giacomazzo and Perna, 2013). The accretion stage is the stage where the binary merger eventually leads to a short GRB (Metzger et al., 2008), although the formation and evolution of the hyper-massive NS (a proto-magnetar) following the merger has also been proposed as the central engine for short GRBs (Fan et al., 2013; Zhang, 2013).

Long GRBs are thought to originate from the collapse of massive, metal-poor stars (Woosley and MacFadyen, 1999). Figure 1.8 demonstrates the evolution of a massive star ($M > 30M_{\odot}$) leading to a long GRB. The generally accepted model for the creation of the long GRBs is also known as the collapsar model (Woosley and MacFadyen, 1999), since it is based on the collapse of the iron core of the massive star to form a BH and an accretion disk.

For the collapsar model to work, the star should have enough angular momentum so that when the inner iron core collapses to form a BH, the outer layer of the star has sufficient outward centrifugal force to form an accretion disk. The

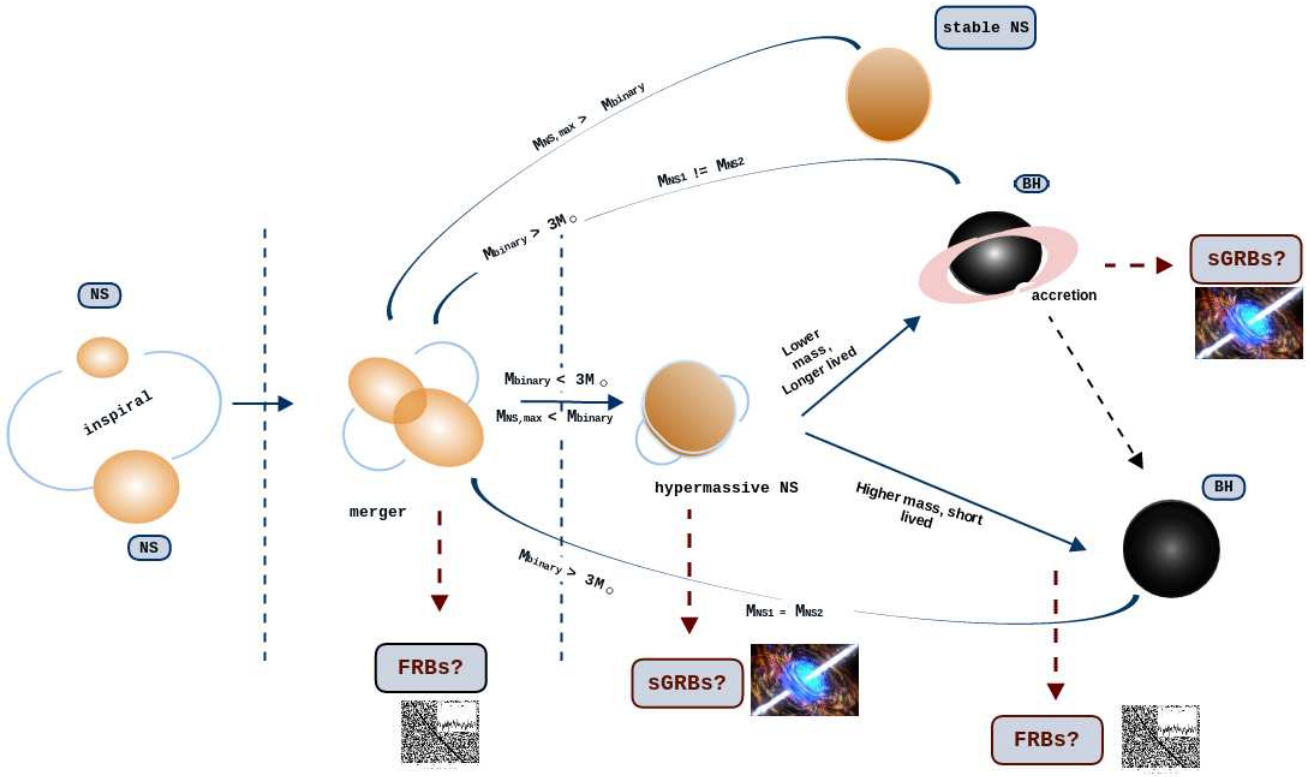

Figure 1.7: The evolution of a compact binary NS merger leading to a short GRB. This figure is modified from Bartos et al. (2013). NS-NS inspirals are observable for a few seconds to minutes. Upon merge, binaries with total mass $M_{binary} > 3M_{\odot}$ collapses to Black hole (BH), if $M_{NS1} = M_{NS2}$. For non-equal mass NS binaries ($M_{NS1} \neq M_{NS2}$), the forming BH will be surrounded by an accretion disk. The NS binaries with mass $M_{NS,max} < M_{binary} < 3M_{\odot}$ form a hypermassive NS with strong differential rotation. The hypermassive NS survives for a few millisecond to seconds and eventually collapses into a BH, potentially with an accretion disk. Very low mass binaries will form a stable NS or a Magnetar.

core grows as it accretes the rest of the star at a very high rate ($\sim 0.1-1\,M_{\odot}\,s^{-1}$). The accretion declines to the point where a jet can form and move outwards. The first interaction of the jet and the circumstellar environment produces the first γ rays and hard X-rays. The jet continues for a few more seconds, fully evacuating the polar column and reaching relativistic speeds. The internal shocks and circumstellar interactions cause the main GRB. It is suggested that the collapsing star also undergoes an intermediate stage to form a NS (proto-magnetar) before collapsing into a BH (Dessart et al., 2008; Metzger et al., 2011).

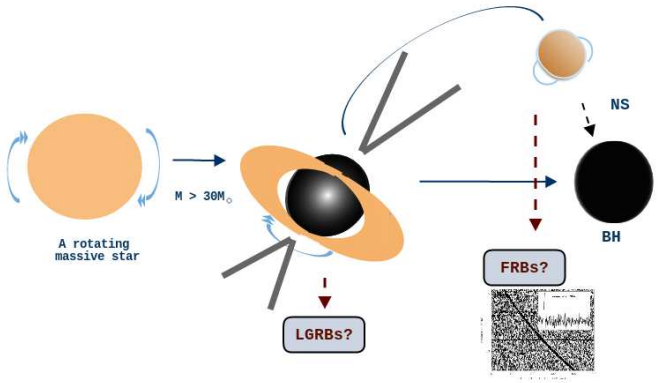

Figure 1.8: The evolution of a rapidly rotating massive star ($M > 30\,M_{\odot}$) leading to a long GRB forming a BH. The evolution is also known as the collapsar model, since it is based on the collapse of the iron core of the massive star to form a BH and an accretion disk. It has been suggested that the collapsing star also undergoes an intermediate stage to form a NS stars (proto-magnetar) before collapsing into a BH (Dessart et al., 2008; Metzger et al., 2011).

A possible GRB-FRB connection

GRBs are proposed to originate from two types of progenitor: due to collapse of the massive star; or due to NS-NS merger, NS-BH mergers. Both of the two methods require large angular momentum and a strong magnetic field to launch a relativistic jet, which is beamed towards Earth and gives rises to the Doppler-boosted emission in $\gamma-$ rays (Rezzolla et al., 2011; Etienne et al., 2012; Gao et al., 2013). There are two types of plausible central engine models proposed for a GRB, described above.

Based on the latter model of the central engine, recently, Zhang (2013) suggested that FRBs could be physically connected to GRBs (both long and short GRBs). They proposed that a FRB can be produced when a supra-massive neutron star undergoes rapid spin down (due to strong magnetic fields) within $10^2 - 10^3$ s of their birth, collapsing into a black hole as it loses centrifugal support. These short duration pulses (FRBs) are proposed to be detectable at radio frequencies ranging from 1.2 to 1.5 GHz, if they are not absorbed by the GRB blast wave in front of the emission region.

Zhang (2013) showed that the steep decay in the X-ray light curve for some GRBs following the stable internal plateaus (top panel Figure 1.9), with the decay index steeper than -3 and even reaching up to -9, requires a steady central engine (a magnetar) which lasts longer than the burst itself. The external shock emissions of these light curves are buried below the internal plateau (dashed lines). But this is in contrast to normal GRB light curves (bottom panel Figure 1.9), where most normal plateaus follow a decay with index of -1, which is dominated by the external shocks and are consistent with the external shock model of GRBs (Gao et al., 2013). The end of the normal plateau may also coincide with the end of the magnetar energy injections, however the internal emissions in these cases may be outshone by the external shock emissions. Such a sharp drop at the end of the internal X-ray plateau marks the sudden end of the central engine, indicating the turn-off of the spinning down magnetar as it collapses into a BH. Zhang (2013) suggested that the break time, shortly after, is the epoch when an FRB is emitted (vertical dotted line Figure 1.9).

1.3.2 Searching for FRBs in the Direction of the Galactic Centre

The Galactic Centre (GC) at the distance of ~ 8.3 kpc (Genzel et al., 2010), offers a unique view of the complex and dynamic nature of galactic nuclei. The centre of our Galaxy is by far the closest galactic nucleus. The GC is a dynamic region in our Galaxy and hence a promising region to search for FRBs. Discovering FRBs from the Galactic Centre (GC) would provide an excellent opportunity to probe the nature of the interstellar medium (ISM) in its vicinity. The density of the ionised medium can be inferred from its imprint on the radio signals. The inner parsec of our Galaxy is one of the most active massive star formation regions in the Galaxy and is believed to contain a large number of massive young stars (Genzel et al., 2010; Wharton et al., 2012). These massive stars are believed

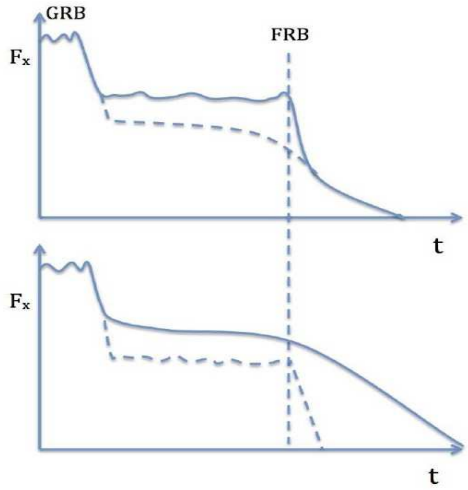

Figure 1.9: The FRB-GRB connection as explained by Zhang (2013). Figure illustrates X-ray light curves plotted as the function of time vs flux. The X-ray lightcurves shown here are a generic representaion for all GRB. Since each stage in the X-ray lightcurve for each GRB occur at varied time scales, specfic time units have not been mentioned. Top panel: shows X-ray light curve for some GRBs which have steep decay curve following the stable internal plateaus. Bottom panel: shows normal X-ray GRB light curve with a normal plateaus. Zhang (2013) showed that in both cases the plateaus may coincide with the end of a magnetar energy injections.

to be the progenitors of the neutron stars where the stars undergo supernova explosions and leave behind neutron stars. Due to the abundance of massive stars, it is assumed to host thousands of neutron stars (Chennamangalam and Lorimer, 2014). Theoretical estimates have suggested that a large population of compact objects in extreme matter states like NS should be orbiting the GC with periods $\leq$ 100 years (Pfahl and Loeb, 2004; Wharton et al., 2012; Chennamangalam and Lorimer, 2014).

The GC, R $\leq$ 200 pc, contains more stars with initial mass around 100 $M_{\odot}$ than anywhere else known in the Galaxy, and also hosts three massive star clusters (Figer, 2009). One of these central clusters contains at least 80 massive stars (Figer, 2008).

Recently, a magnetar (PSR J1745-29) was discovered, it is the only NS discovered in the inner parsec, with the projected distance of 0.12 pc ($3''$) from the GC (Spitler et al., 2014) and (Bower et al., 2014).

1.4 Thesis Outline

Motivated by the discovery of FRBs, advances in observational radio astronomy related to high performance computing and the improved ability to process large datasets quickly, and by the models that suggest at least some FRBs may be connected to GRBs, we outline the structure of this thesis.

Chapter 1 has provided introductory material regarding the motivating factors for this thesis.

Chapter 2 will discuss aspects of the methods used to search for FRBs in connection with GRBs and the Galactic Centre. This chapter will summarise information regarding the signals we expect to detect from FRBs and the techniques employed to make these detections, as well as the hardware and experimental methods used in the thesis.

Chapter 3 contains the main original work of this thesis, the observation of five GRBs, in order to search for related FRB radio emission. This work employed radio telescopes, very large data sets, and specialised signal processing algorithms. This chapter presents a detailed statistical analysis of our results and makes comparisons to previous studies.

Chapter 4 contains material similar to Chapter 3, but describing the search for FRBs in the direction of the Galactic Centre.

Chapter 5 contains a brief set of conclusions.

Chapter 2

Techniques and Instrumentation

Observatory, n.
A place where astronomers conjecture away the guesses of their predecessors.
Ambrose Bierce, *The Devil's Dictionary*, 1911

2.1 Introduction

As discussed in Chapter 1, time domain astronomy is of great interest to the radio astronomy community. With the advent of time domain surveys with data-intensive instruments such as the Square Kilometre Array (SKA: (Dewdney et al., 2010; Huynh and Lazio, 2013)) and its precursor telescopes, current observations with existing telescopes play a key role in exploring different observational strategies for conducting such surveys, and exploring early science. In addition, current experiments demonstrate how time domain data from these surveys can be properly interpreted in the presence of stochastic and systematic uncertainties introduced by the instruments themselves and other non-astronomical radio sources (human-made Radio Frequency Interference, RFI, for example).

In this chapter we describe the telescopes and their subsystems used for the work presented in this thesis and we also discuss the stochastic and systematic errors that affect the search for radio astronomy transient sources.

2.2 Radio Observations

This section presents a brief description of some basic techniques and instrumentation used for the research presented in this thesis. A detailed reference for the

basic techniques of radio astronomy is given in "Radio Astronomy" by Kraus (1988).

2.2.1 Introduction to Radio Telescopes and Their Subsystems

Radio telescope subsystems are generally divided into two parts: the antenna and front-end, consisting of radio frequency (RF) and intermediate frequency (IF) electronics; and the back-end, were the data are sampled, digitised and recorded. In the following sections we give a brief description of these subsystems. More detailed information on radio telescope subsystems can be found in Stanimirovic et al. (2002) and Phillips et al. (2009).

Antennas and the Front-end

Radio antennas range from simple dipole antennas (for example: the Murchison Widefield Array: Tingay et al. (2013)) to parabolic or spherical dishes (for example the 64-m radio dish at Parkes). Dipoles are mainly designed for metre or longer wavelengths. Since arrays of dipoles are impractical at wavelengths $\lambda < 1\,\mathrm{m}$, most high frequency radio telescopes use large parabolic or spherical reflectors to concentrate the radio waves originating from distant radio sources and focus them onto a simple antenna of the appropriate dimensions for the wavelength of interest (known as a feed). The feeds on dishes are generally dipoles or wave-guide horns backed by small reflectors, which are connected to the receivers. The shape of a reflector is chosen such that the plane wave front from a distant source is in phase at a focal point. This implies that the surface must be *rotational* symmetric about its axis.

In the following, we work through several concepts relevant to the different radio telescope sub-systems.

Antenna Pattern An important characteristic of a receiving antenna is its ability to reflect radio waves incident upon it, which is generally described as the effective aperture or effective area $\mathrm{A_e}(\nu, \theta, \phi)$, where ν is frequency and θ and ϕ are the direction coordinates, respectively. The normalised antenna reception pattern $\mathcal{A}$, or the power pattern as it is often called, is defined as, $\mathcal{A}(\nu, \theta, \phi) = \mathrm{A_e}(\nu, \theta, \phi)/\mathrm{A_0}$, where $\mathrm{A_0}$ is the response at the centre of the main lobe of $\mathrm{A_e}(\nu, \theta, \phi)$.

A typical power pattern is shown in Figure 2.1. The power pattern has a primary maximum, called the main lobe and several maxima, called side lobes.

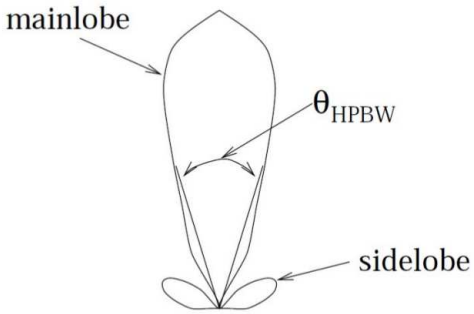

Figure 2.1: Power pattern of a dish antenna. Figure Credit: Chengalur et al. (2007).

The points at which the main lobe power falls to half its central value are called the half power points and the angular distance between these points is called the half power beamwidth (HPBW). The HPBW of the telescope (or angular resolution), $\theta_{\rm HPBW}$, one can achieve at the observing wavelength, $\lambda_{\rm obs}$, with a dish of diameter, D, is $\theta_{\rm HPBW} \sim 1.22\,\lambda_{\rm obs}/{\rm D}$. The larger the telescope, the better the angular resolution. The Arecibo radio telescope, a 300-m dish, is the largest single dish radio telescope currently in operation and has an angular resolution at 1.4 GHz of $\sim 2.5'$.

Flux Density The strength of the radio signal received by a radio telescope from a point source is expressed as the spectral flux density, $\rm S_\nu$, and is measured in $\rm Wm^{-2}Hz^{-1}$ (Goldsmith, 2002)[1]:

$$\rm S_\nu = \int_{source} I_\nu d\Omega, \tag{2.1}$$

where $\rm I_\nu$ is the specific intensity, defined as the spectral flux density emitted per solid angle subtended by the radiating surface, measured in units of $\rm Wm^{-2}Hz^{-1}sr^{-1}$.

Received Power The received power, $\rm P_A$, delivered by the antenna to a matched load in a bandwidth of $\Delta\nu$, for a randomly polarised source of flux density $\rm S_\nu$ is given by (Thompson et al., 2001):

$$\rm P_A = \frac{1}{2}\, S_\nu\, A_e\, \Delta\nu, \tag{2.2}$$

where the factor of 1/2 takes account of the fact the the antenna responds to one half of the power in the randomly polarised wave in a single polarisation feed antenna. $\rm A_e$ for a reflector antenna, for radiation incident on the centre of the

[1]The common radio astronomy unit of flux density is the Jansky (Jy), 1Jy = $10^{-26}\rm Wm^{-2}Hz^{-1}$.

main lobe, is equal to the projected geometric area $A_p = \frac{\pi D^2}{4}$ multiplied by an aperture efficiency η_A (0.3 - 0.8), $A_e = A_p \times \eta_A$.

Antenna Temperature The antenna temperature (T_A) is defined as the blackbody temperature equivalent to the radiation incident on the antenna. That is, consider a telescope observing a point source (i.e a source smaller than the telescope beam size) with flux density S. Replace the feed of the telescope with a resistor. If the temperature of the resistor is adjusted such that the power received is the same as the power received from the point source, then the antenna temperature is equal to the resistor temperature. Based on the Nyquist theorem[2], the measured spectral power is given by $W = kT_A$ (Johnson, 1928).

The minimum detectable T_A is set by the fluctuations in the receiver output caused by thermal noise[3]. This noise is directly proportional to the system temperature (T_{sys}). The system temperature can be written as,

$$T_{sys} = T_A + T_R + T_{sky} + T_{LP}, \tag{2.3}$$

where T_R is the receiver noise and T_{sky} is the contribution of the background sky sources. For example, our Galaxy is a strong emitter of non thermal radiation and is dominant at low frequencies. T_{LP} is the physical temperature of the transmission line between the antenna and the receiver.

System Equivalent Flux Density Two of the most important parameters characterising a radio telescope are the system temperature (T_{sys}) and aperture efficiency (η_A). Both combine to define a quantity called the System Equivalent Flux Density (SEFD). The SEFD is defined as (Thompson et al., 2001),

$$\text{SEFD} = \frac{2\,k\,T_{sys}}{A_e} = \frac{2\,k\,T_{sys}}{A_p\,\eta_A} = \frac{8\,k\,T_{sys}}{\pi\,D^2\,\eta_A}. \tag{2.4}$$

where k is Boltzmann's constant. The SEFD is used to characterise the performance of the system, with low values indicating a more sensitive system.

Telescope Sensitivity The sensitivity of a radio telescope is a measure of the weakest source of radio emission that can be detected; it is related to the system noise and thus the SEFD.

For a radio signal to be detectable, its signal must exceed significantly the noise fluctuations in the receiver system. Hence the sensitivity of the radio telescope

[2]In thermal equilibrium, the power is determined by the physical temperature. This is also called Johnson noise

[3]Thermal noise is the input-equivalent of the sum of noise generated in the receiving system, such as the amplifiers, attenuators, connectors etc and as well as in the noise picked up by the side-lobes and thermal radiation from the atmosphere

is equal to the root mean square (rms) noise fluctuations of the system, which is given by (O'Neil, 2002),

$$\Delta T_{rms} = \frac{K_s T_{sys}}{\sqrt{\Delta\nu \, t \, n_{pol}}}, \tag{2.5}$$

where K_s is the constant of the telescope (dimensionless and close to unity: (O'Neil, 2002)), $\Delta\nu$ is the bandwidth, t is the integration time, and n_{pol} is the number of polarisations. The minimum detectable temperature is typically considered to be 3-5 times the rms noise temperature[4].

The minimum detectable temperature can be converted to a minimum flux density by applying the Rayleigh-Jeans approximation. Consider Planck's Law for blackbody radiation, given by (O'Neil, 2002),

$$I_\nu = \frac{2h\nu^3}{c^2}\left[\frac{1}{e^{h\nu/kT}-1}\right], \tag{2.6}$$

where h is Planck's constant, ν is the frequency frequency in Hz and T is the physical temperature in K. For typical radio observing frequencies (1 GHz), $h\nu/k = 0.048$, hence the applying Rayleigh-Jeans approximation, $e^{h\nu/kT} \sim 1 + h\nu/kT$,

$$I_\nu = \frac{2\nu^2}{c^2}kT = \frac{2kT}{\lambda^2}. \tag{2.7}$$

In the Rayleigh-Jeans approximation, the specific intensity emitted by a source is proportional to its temperature, and inversely proportional to the square of the wavelength.

In the Rayleigh-Jeans domain the T_B is equal to the temperature of the black body $T_B = T$.

Hence, using Equation 2.7 the brightness temperature T_B for any radiation mechanism can be derived as,

$$T_B = \frac{c^2 I_\nu}{2\,\nu^2\,k}. \tag{2.8}$$

For a discrete source of temperature T subtending a solid angle Ω_S, the source flux density (S) in the Rayleigh-Jeans limit is obtained by integrating the source over the source solid angle, which is given by,

$$S = \frac{2\,k}{\lambda^2}\int_{\Omega_S} T(\theta,\phi)\,d\Omega. \tag{2.9}$$

[4]In general we chose the minimum detectable temperature to be 3-5 times the rms noise temperature since the confidence level on the signal is $\sim$ 96-99%. Refer footnote 8 in chapter 3 for more details.

If the brightness temperature of the source is uniform across the solid angle, the above equation reduces to,

$$S = \frac{2\,k\,T}{\lambda^2}\,\Omega_S. \tag{2.10}$$

Equating Equation 2.7 and 2.10 with Equation 2.5,

$$\Delta I_{\nu,\mathrm{rms}} = \frac{2\,k}{\lambda^2}\,\frac{K_s\,T_{sys}}{\sqrt{\Delta\nu\;t\;n_{pol}}}, \tag{2.11}$$

$$\Delta S = \frac{2\,k}{A_e}\,\frac{K_s\,T_{sys}}{\sqrt{\Delta\nu\;t\;n_{pol}}}, \tag{2.12}$$

where $\frac{2\,k}{A_e} \times T_{sys}$ is equal to the SEFD.

So far we have presented an overview of radio telescopes. Further, we gave a brief discussion of key radio astronomical terminologies, including flux density, antenna pattern, antenna temperature and received power. In order to analyse radio telescope system performance, we calculated the sensitivity of the radio telescope to a point source. We discussed the effects of the telescope characteristics on the beam width. Understanding this basic behavior allows us to determine what measurements are needed to calibrate the antenna, and to determine whether the system is performing properly.

The RF Front End The feed antenna mounted on the telescope converts radio waves to a fluctuating voltage. This voltage varies at the same frequency as the radio wave incident on the feed antenna. The fluctuating voltages are weak and are amplified using a low noise amplifier that has a specific frequency response within a band centred at a radio frequency denoted by ν_{RF}. The amplified voltages are then passed through a band-pass filter. The signals are then passed into a mixer, where the frequency of the input signal is changed or down converted. The mixer beats the RF signal with a monochromatic signal of frequency ν_{LO} provided by a local oscillator (LO). The result is an intermediate frequency (IF) signal at the sum and difference of ν_{RF} and ν_{LO}. For down conversion one isolates the frequency difference signal $\nu_{IF} = \nu_{RF} - \nu_{LO}$, known as the IF. The IF signal is then amplified again before it is recorded or otherwise detected or processed. Typically both polarisations of the RF signals are recorded to recover full information from the radio waves. Figure 2.4 shows a block diagram of a typical single-dish radio telescope illustrating the various sections of a radio telescope.

2.2.2 The Digital Back End

The output of the base-band signal is sent to the sampling device. The sampling device samples the voltages at the Nyquist rate $\nu_{\rm Nyq} = 2{\rm B}$, where B is the bandwidth, and then digitizes the sampled signals (Oppenheim et al., 1999). The digitized data can be recorded on a disk for offline processing or can be used to process online. In such a situation, assuming 8-bit samples and a bandwidth of 64 MHz, the combined data rate for two polarisations is 256 MB/s (0.922 TB/hr), which is a large data rate. If the data were re-sampled to 2-bit, the data rate reduces to 64 MB/s (0.2304 TB/hr).

To reduce the amount of data recorded and stored, there are several techniques that are often implemented in large pulsar and single pulse search surveys. The simplest is the generation of filter-bank data. A filter-bank channelises the band using several narrow band-pass filters and the power is detected independently in each channel, then averaged over time. Thus, the data rate drops dramatically compared to recording voltages, but the act of detecting the power and accumulating destroys information. For this thesis, we directly store the sampled and digitised voltages onto disk. The recorded data are then channelised and power is detected offline in post-observation processing to generate our required data products.

Autocorrelation Any radio signal, even random noise, is always correlated with itself. This fact is exploited by auto-correlation spectrometers. Following (Bracewell, 2000), let us consider a function s(t) which has a Fourier transform:

$$\mathrm{S(f)} = \int_{-\infty}^{+\infty} \mathrm{s(t)}\, \mathrm{e}^{-\mathrm{j}\,2\,\pi\,\mathrm{f}\,\mathrm{t}}\, \mathrm{dt}. \tag{2.13}$$

Given the signal s(t), the auto-correlation function $R_{ss}(\tau)$ is defined as the cross correlation of s(t) with itself, at lag τ,

$$\mathrm{R_{ss}}(\tau) = (\mathrm{s(t)} * \bar{\mathrm{s}}(-\mathrm{t}))(\tau) = \int_{-\infty}^{+\infty} \mathrm{s(t+\tau)}\, \bar{\mathrm{s}}(\mathrm{t})\, \mathrm{dt}, \tag{2.14}$$

where $\bar{\mathrm{s}}$ represents the complex conjugate of s and * represents convolution.

The auto-correlation theorem states:

$$|\mathrm{S(f)}|^2 \;=\; \int_{-\infty}^{+\infty} \mathrm{R_{ss}}(\tau)\, \mathrm{e}^{-\mathrm{j}\,2\,\pi\,\mathrm{f}\,\mathrm{t}}\, \mathrm{dt}, \tag{2.15}$$

where $|\mathrm{S(f)}|^2$ is the power spectrum of the original function s(t). Thus, by taking the Fourier transform of the auto-correlation function, we get the power

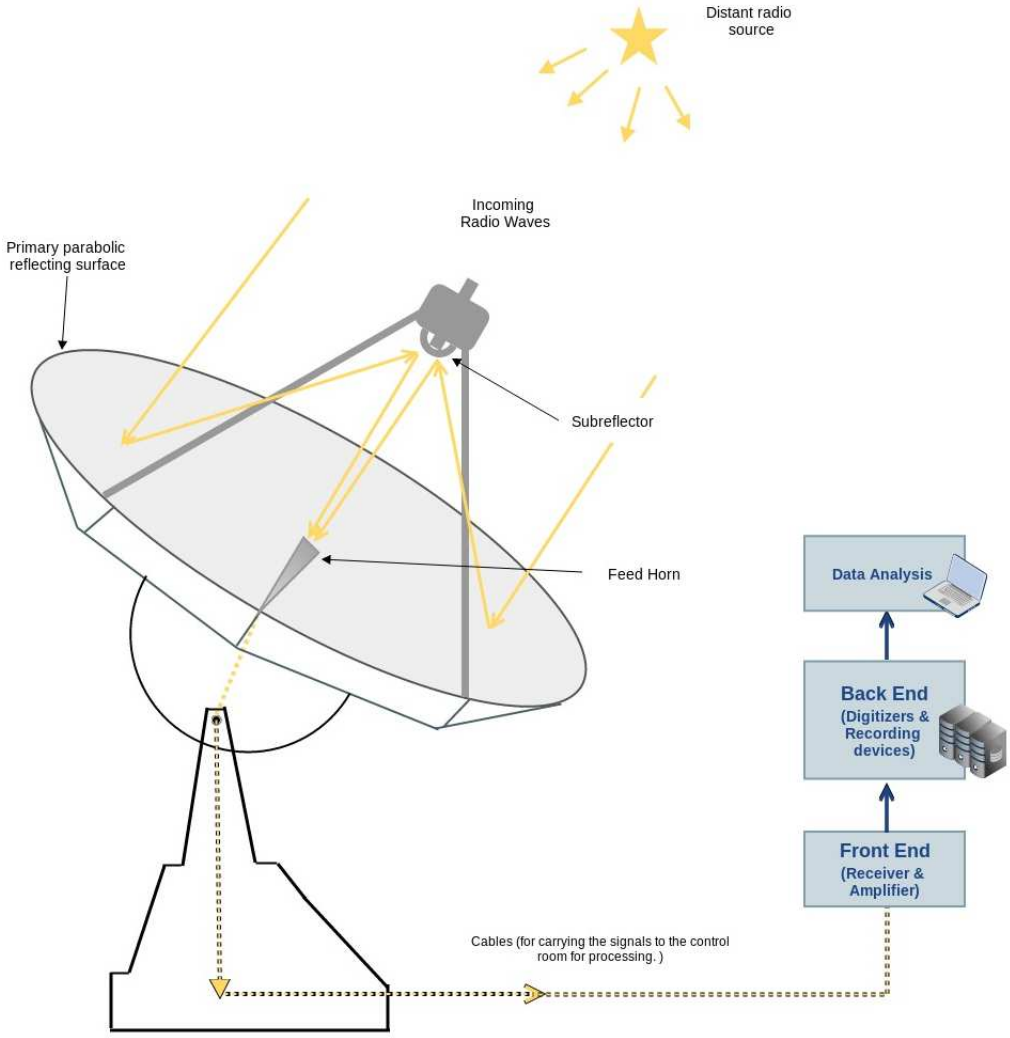

Figure 2.2: Conceptual diagram of a radio telescope and its subsystems. The subsystems are traditionally divided into two: the antenna and the frontend; and the backend.

spectrum, which is a special case of the convolution theorem. In some digital autocorrelators, this is done by applying a finite number of the time lags to the signals and then multiplying the original signal with the delayed signal. The product as a function of lag is then Fourier transformed to derive the power spectrum. Hence, the two fundamental operations required to auto-correlate the recorded voltage signals are the Fourier transform (F) and cross multiplication (X). The order of these operations are interchangeable with almost identical results, depending on the details of implementation, which leads to two correlator architectures, known as XF and FX. For the research in this thesis we use an FX correlator architecture. Figure 2.3 shows the block diagram of an FX digital correlator. The input signals from a single polarisation are channelised by performing Fourier transforms and then multiplying the Fourier transformed data with its own complex conjugate. The multiplication detects the power in each frequency channel produced in the Fourier transform and these powers are then averaged over a timescales appropriate for the required application.

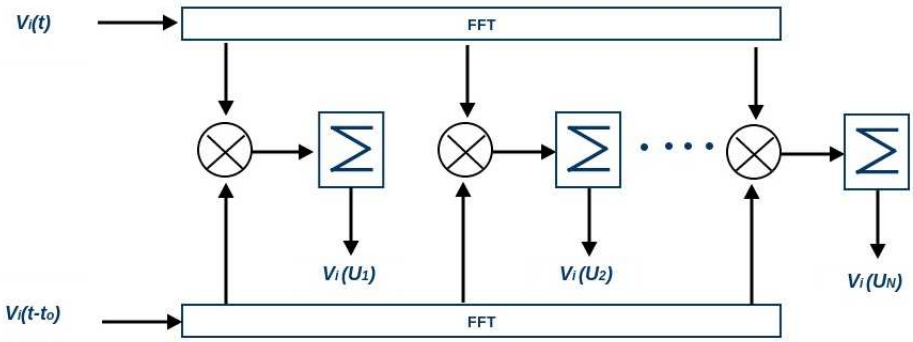

Figure 2.3: Block diagram of an auto-correlation spectrometer. The input signal from a single polarisation is channelised by performing Fourier transforms and multiplied with the delayed version of itself. The results are passed to the accumulator that outputs the averaged data.

2.3 The Hobart Radio Telescope

The Hobart radio telescope, operated by the University of Tasmania, is a 26-m single dish radio telescope located at the Mount Pleasant Radio Observatory near Hobart, Tasmania. This antenna was originally built by NASA for tracking space vehicles, and was installed near Canberra. Later the antenna was moved

to Hobart and is now extensively used for geodetic and astrophysical Very Long Baseline Interferometry (VLBI) observations. However, the XY antenna mount and fast drives mean that it retains its satellite tracking capabilities. The telescope is equipped with a variety of receivers which operate between 660 MHz and 22 GHz[5].

The telescope is equipped with a dual-polarisation, 64 MHz bandwidth baseband recording capability. For this research we used the Australian Long Baseline Array Data Acquisition System (LBA-DAS). The DAS is a sampler and digital filter used at all the LBA stations (Phillips et al., 2009). The DAS receives two independent IF frequencies (right circular polarisation (RCP) and left circular polarisation (LCP)) which are band limited to 64 MHz. The IF signals are digitised at 8 bits and then run through a series of digital filters and samplers where they are re-sampled to 2 bits. The re-sampled data are then recorded on the disk, using the LBA data recorder (LBADR). The LBADR is a standard server grade rack-mountable PC, with addition of a VSIB PCI card, designed by Metsahovi Radio Observatory (Ritakari and Mujunen, 2004). A detailed description of the LBADR is given in Phillips et al. (2009).

Figure 2.4: The 26-m radio telescope located at the Mount Pleasant Radio Observatory operated by University of Tasmania (UTas) near Hobart, Tasmania. Image Credit:JJ Harrison, UTas.

2.4 Single-Pulse Search Methodology

In this section, we describe general issues that must be considered by any survey searching for FRBs. There are various factors that affect the observed flux density and shapes of the radio pulses from an astronomical source. In this section we outline propagation effects and well-known techniques used to correct for them.

[5]www.rawiki.phys.utas.edu.au

2.4.1 Propagation Effects

Radio signals travel a long distance through the intergalactic medium (IGM) and interstellar medium (ISM) before reaching the Earth. The IGM and ISM are highly ionised and non-homogeneous. Hence, the incoming radio signals experience various distortions as they propagate through these media. Here we summarise some of the major propagation effects.

Dispersion

The ISM and IGM disperse radio signals traversing through them. The interaction of the radiation with the electrons along the line-of-sight between the source and the observer results in a frequency-dependent delay in the arrival of the wave. Over a finite bandwidth, the wave-front emitted at lower radio frequencies travels slower through the ISM/IGM, arriving later than those emitted at higher frequencies. This dispersion delay is a fundamental parameter in searches for FRBs, allowing discrimination between astronomical signals and terrestrial signals.

Principle of Cold Plasma Dispersion For the purpose of describing the effects of dispersion on a propagating electromagnetic wave, here we model the ISM as a low-density electron plasma, with plasma frequency, ν_p (Lorimer and Kramer, 2012),

$$\nu_{\rm p} = \sqrt{\frac{{\rm n_e}\,{\rm e}^2}{\pi\,{\rm m_e}}}, \tag{2.16}$$

where $\rm n_e$ is the electron density, e is the electron charge, and $\rm m_e$ is the electron mass, hence,

$$\nu_{\rm p} = \sqrt{\frac{{\rm n_e}\,{\rm e}^2}{\pi\,{\rm m_e}}} \approx 8.97\,{\rm kHz} \times \left(\frac{\rm n_e}{\rm cm^{-3}}\right)^{1/2}.$$

The electrons in the ISM make up a cold plasma having a refractive index, μ (Lorimer and Kramer, 2012),

$$\mu = \sqrt{1 - \left(\frac{\nu_{\rm p}}{\nu_{\rm obs}}\right)^2}, \tag{2.17}$$

where $\nu_{\rm obs}$ is the observing frequency. For propagating radio waves, refractive index $\mu < 1$, the group velocity ${\rm v_g} = {\rm c}\,\mu$ of pulses is less than the vacuum speed of light c, in accord with the requirements of special relativity. For most radio

observations, $\nu_{\rm obs} \gg \nu_{\rm p}$, therefore the group velocity of the low-density electron plasma can be written as (Lorimer and Kramer, 2012),

$$\mathrm{v_g} \approx \mathrm{c}\sqrt{1-\left(\frac{\nu_{\rm p}}{\nu_{\rm obs}}\right)^2}. \tag{2.18}$$

Therefore, a broadband pulse moves through a plasma more slowly at lower frequencies than at higher frequencies. If the distance to the source is d, the dispersion delay t at frequency $\nu_{\rm obs}$ is:

$$\mathrm{t} = \left(\int_0^d \frac{\mathrm{dl}}{\nu_{\rm g}}\right) - \frac{d}{\mathrm{c}}. \tag{2.19}$$

Substituting $\mathrm{v_g} = \mathrm{c}\,\mu$ in the equation 2.19,

$$\mathrm{t} = \left(\int_0^d \frac{\mathrm{dl}}{\mathrm{c}\,\mu}\right) - \frac{d}{\mathrm{c}} \approx \left(\int_0^d \frac{\mathrm{dl}}{\mathrm{c}\sqrt{1-\left(\frac{\nu_{\rm p}}{\nu_{\rm obs}}\right)^2}}\right) - \frac{d}{\mathrm{c}}. \tag{2.20}$$

Here we note that generally $\nu_{\rm p} \ll \nu_{\rm obs}$[6], and the above equation can be approximated as $(1-\mathrm{x})^{-\mathrm{n}} \approx 1 + \mathrm{nx}$, where $\mathrm{x} \ll 1$,

$$\left(\sqrt{1-\left(\frac{\nu_{\rm p}}{\nu_{\rm obs}}\right)^2}\right)^{-1} \approx 1 + \frac{\nu_{\rm p}^2}{2\,\nu_{\rm obs}^2} = 1 + \frac{\mathrm{n_e\,e^2}}{2\,\pi\,\mathrm{m_e}\,\nu_{\rm obs}^2}. \tag{2.21}$$

Substituting equation 2.21 into 2.20 we get,

$$\begin{aligned} \mathrm{t} &= \frac{1}{c}\int_0^d \left(1 + \frac{n_e\,e^2}{2\,\pi\,m_e\,\nu_{obs}^2}\right)\,dl \;-\; \frac{d}{c} \\ &= \frac{e^2}{2\,\pi\,m_e\,c\,\nu_{obs}^2}\int_0^d n_e dl \\ &\equiv\; D \;\times\; \frac{DM}{\nu_{obs}^2}, \end{aligned} \tag{2.22}$$

where DM is the dispersion measure, which is the integrated column density of free electrons towards a source at distance d,

$$\mathrm{DM} = \int_0^d \mathrm{n_e\,dl}. \tag{2.23}$$

[6]A radio wave can only propagate through a tenuous plasma if its frequency exceeds the plasma frequency. Hence $\nu_{\rm obs} \gg \nu_{\rm p}$

This is usually expressed in $\mathrm{pc\,cm^{-3}}$ and $D = \frac{e^2}{2\,\pi\,m_e\,c} = 4.15 \times 10^3\,\mathrm{MHz^2\,pc^{-1}cm^3\,s}$.

The time delay Δt_{DM}, between the arrival of the higher (ν_{hi}) and lower (ν_{lo}) frequencies (in MHz) in an observing bandwidth is given by (Lorimer and Kramer, 2012),

$$\Delta t_{DM} \simeq 4.15 \times 10^6\,\mathrm{ms} \times \left(\nu_{lo}^{-2} - \nu_{hi}^{-2}\right) \times \mathrm{DM}. \tag{2.24}$$

Scattering

Radio signals can be scattered by electrons in the ISM, which causes the signal to arrive along multiple paths (Lorimer and Kramer, 2012). This effectively convolve's the un-scattered pulse profile with a one-sided exponential tail, e^{-t/τ_s}, where τ_s is the scattering time. The scattering of the pulse depends on the fluctuations of the election column density δn_e along the line-of-sight and also on the frequency of observation, $\tau_s \propto \nu^{-\alpha}$, where $\alpha \sim 4$ for Galactic pulsars (Bhat et al., 2004) . The effects of scattering are hard to correct for. The scattering can be estimated by the empirical formula (Bhat et al., 2004),

$$\log \tau_s = -6.46 + 0.154 \log \mathrm{DM} + 1.07\,(\log \mathrm{DM}^2) - 3.86 \log \nu\,(\mathrm{ms}), \tag{2.25}$$

where ν is frequency in GHz.

2.4.2 Radio Signal Model

The intensity of a broadband source can be modeled as (Cordes and McLaughlin, 2003),

$$I(t) = g_r g_d S(t) * h_{DM}(t) * h_d(t) * h_{Rx}(t) + N(t), \tag{2.26}$$

where S(t) is the intensity from the source which is modulated by the factors of g_r and g_d, corresponding to the refractive and diffractive scintillation modulations which are also convolved with the dispersion $h_{DM}(t)$. Pulse broadening from multipath propagation $h_d(t)$, $h_{Rx}(t)$ represents averaging in the receiver and DAS and N(t) represents the receiver noise.

To a large extent the dispersion $h_{DM}(t)$ can be removed from the signals. Pulse broadening due to multipath scattering can dominate the shape of the measured pulses. In that case to obtain detection we time average the data over a large range of pulse widths.

2.4.3 Effective Time Resolution

A delta function pulse emitted at the source will be detected with finite pulse width because it is affected by propagation effects (discussed above) and signal processing effects. The effective time resolution of the pulse can be written as the quadratic sum of dedispersion error, the receiver filter response time, and scattering time (Cordes and McLaughlin, 2003),

$$\Delta t^2 = t^2_{\rm DM} + t^2_{\delta \rm DM} + \Delta t^2_{\Delta\nu} + \tau_{\rm s}^2, \tag{2.27}$$

where $t^2_{\rm DM}$ is the frequency dependent delay (equation 2.24) and $t^2_{\delta \rm DM}$ is the error in the value of the DM by an amount of δDM which leads to smearing $\Delta t_{\delta \rm DM} = \Delta t_{\rm DM}$ (δDM/DM). $\Delta t_{\Delta\nu}$ is the filter response of a individual frequency channel $\Delta t_{\Delta\nu} \sim (\Delta\nu_{\rm MHz})^{-1}$, where $\Delta\nu_{\rm MHz}$ is the resolution of each frequency channel. $\tau_{\rm s}$ is the distortion in the pulse width due to interstellar medium scattering.

2.4.4 Radio Frequency Interference

Human-made Radio Frequency Interference (RFI) is an increasing hindrance for radio observations. Due to RFI, radio observing bands are restricted. Sources of RFI include telecommunications, airport and military radars, satellites, high voltage power lines etc. The signal strengths of RFI are many orders of magnitude stronger than from distant radio sources. RFI are generally narrow band but have a variety of temporal characteristics such as being bursty or slowly varying over seconds or longer. There are RFI which are wide band, which affects the power in the entire frequency band or a substantial amount of it.

RFI Excision Techniques

There are numerous techniques proposed to excise RFI in the data, such as thresholding (Weber et al., 1997; Leshem et al., 2000), using a reference antenna (Barnbaum and Bradley, 1998), spatial filtering (Kocz et al., 2010) and many more. In this thesis we adopt thresholding techniques to excise RFI. In the thresholding technique a channel or a time step is marked as RFI if a specific quantity, such as signal strength exceeds the predetermined threshold (for example 3-5 times rms). In general, thresholding is performed in two stages: first excision of bad frequency channels; and then excision of bad time samples. The affected samples may be set to zero, as in Weber et al. (1997). This is referred to as (time or

frequency) blanking. The threshold is usually applied on the correlated or time averaged data where the interference to noise ratio will be relatively high.

2.4.5 Dedispersion

In principle, dispersion effects can be corrected if the electron column density through which the radiation propagates is known. The degree to which the dispersion can be corrected depends on the methods of the dedispersion used. There are two main approaches to dedispersion: (1) incoherent dedispersion; (2) coherent dedispersion (Hankins and Rickett, 1975).

In the process of incoherent dedispersion, the signal power is largely recovered by splitting the observing frequency band into a large number of independent frequency channels and applying appropriate time delays, Δt_{DM}, to each frequency channel before summing. In this process the signals get degraded due to: (1) the finite computational power limiting the number of DM trials that can used for a given experiment; (2) the incoming signal being smeared over a number of frequency channels.

In the process of coherent dispersion, the voltage data are convolved with the inverse of the transfer function of the dispersive medium. This approach achieves optimum signal to noise (S/N) recovery. However, coherent dedispersion techniques are computationally intensive, making them slow for practical purposes.

Incoherent dedispersion algorithms

Incoherent dedispersion techniques are very popular when processing resources are limited. The tree algorithm is a well known incoherent dedispersion technique, popularly used in early pulsar surveys (Taylor, 1974). The tree algorithm uses the regular structure of time delays and sums the input signal of N frequency channels to generate N dedispersed output signals. This algorithm has certain drawbacks which limits its sensitivity: (1) The dispersion measures for each dedispersed output are fixed to a linear distribution from 0 to diagonal DM. The diagonal DM is the DM at which the gradient of the dispersion curve is one temporal bin per frequency channel; (2) the tree algorithm requires a power of two number of frequency channels. Additional stages are often employed to mitigate these limitations. For example experiments with 96 frequency channels are linearly dedispersed by adding additional dummy channels (32 channels) between the real frequency channels. In this case the total number of channels becomes a power of two number as required.

Another incoherent dedisperser algorithm proposed by D'Addario (2010) and developed for the transient detection system called Tardis is being developed for the Commensal Real-time ASKAP Fast transients (CRAFT) survey (Clarke et al., 2013). The algorithm proposed by D'Addario (2010) involves summing selected samples of the dynamic spectrum. The samples were selected based on the trial dispersion measure, pulse width and spectral indices. The pulse width can include the signal's intrinsic width and also temporal broadening of the signal due to interstellar scattering.

For the research in this thesis, we use an incoherent dedispersion algorithm called DART (a Dedisperser of auto-correlations for Radio Transients) which is also used in the V-FASTR transient detection system (Wayth et al., 2011). DART is specifically designed for data with multiple antennas and multiple frequency bands. The input to DART is the filterbank data ordered by frequency and time. The dedispersed time series are formed by summing the power across the channels, with a delay offset to each channel according to the frequency and the DM. Different polarisations for the same frequencies are also combined at this stage. DART is very flexible compared to the tree algorithm because it supports an arbitrary number and distribution of trial DM steps.

2.4.6 Time Averaging

The intrinsic width of the pulse is generally unknown. Because the observed pulse widths are affected by scattering and dispersion, a large parameter space of pulse widths must be searched. This is done by averaging the time series where the time samples are added iteratively. In the absence of the knowledge of the intrinsic width of the pulse, time averaging is the most effective and efficient approximation to the detection methods.

The signal-to-noise ratio achievable by optimal time averaging can be calculated assuming the intrinsic amplitude and width are $\mathrm{S_i}$ and W_i, respectively, in the absence of extrinsic broadening effects. The broadening conserves the pulse area, so that the peak flux densities for both W and $\mathrm{W_i}$ are related through $\mathrm{S_i} \times \mathrm{W_i} = \mathrm{S} \times \mathrm{W}$, where $\mathrm{S} = \mathrm{m} \times \sigma$ is the detection threshold (Deneva et al., 2009). Hence the minimum detectable intrinsic peak flux density is given by Deneva et al. (2009),

$$\mathrm{S_i} = \left(\frac{\mathrm{W}}{\mathrm{W_i}}\right) \frac{\mathrm{m} \times \mathrm{SEFD}}{\sqrt{\triangle\nu_{\mathrm{MHz}} \times \mathrm{W} \times \mathrm{n_{pol}}}}, \tag{2.28}$$

where SEFD is the system equivalent flux density, $\triangle\nu_{\mathrm{MHz}}$ and W are the bandwidth and integration time, and $\mathrm{n_p}$ is the number of polarisations.

2.5 Single Pulse Search Pipeline

We have developed a single pulse search pipeline. The search pipeline has multiple stages: correlation; time averaging; radio frequency interference (RFI) excision; dedispersion; event detection; and classification of events. A detailed description of the pipeline is discussed in Chapter 3. This processing pipeline is extensively used for the research presented in this thesis.

2.6 Summary

In this chapter, we described radio telescopes and their subsystems. A description of the telescope used for this research was presented. Various issues that affect the flux density and shapes of radio pulses from astronomical objects were discussed. Several techniques employed in FRB searches were also discussed. These techniques are extensively employed in a single pulse pipeline developed for this thesis. A detailed description of the single pulse search pipeline employed to search for FRBs is discussed in Chapter 3.

Chapter 3

A Search for Fast Radio Bursts Associated with Gamma-Ray Bursts

Theories crumble, but good observations never fade.
Harlow Shapey, Director of the Harvard College Observatory.

This Chapter has been published in *The Astrophysical Journal*, 790 (1), 63, as an article entitled 'A Search for Fast Radio Bursts Associated with Gamma-Ray Bursts' by Palaniswamy, D., R. B. Wayth, C. M. Trott, J. N. McCallum, S. J. Tingay, and C. Reynolds (2014).

3.1 Introduction

Gamma-ray bursts (GRBs) are among the most powerful objects in the Universe. The energy output in the γ-rays is in the order of 10^{51} ergs (assuming isotropic emission) on second time-scales at cosmological distances (Rees and Meszaros, 1994; Ghirlanda et al., 2006). GRBs are divided into two classes, short and long, which are usually defined by T_{90} (Kouveliotou et al., 1993), the time during which the cumulative counts in the detector increases from 5% to 95% above the background rate. There are two types of plausible central engine model proposed for GRBs: (1) stellar mass black holes, which accrete material from a remnant star with an extremely high accretion rate ($\sim$ (0.1-1) $M_\odot$ s^{-1}) (Popham et al., 1999; Narayan et al., 2001; Lei et al., 2013); (2) rapidly rotating ($\sim$ ms duration), highly magnetised neutron stars (a proto-magnetar) (Usov, 1992; Rowlinson et al., 2010;

Fan et al., 2013). Based on the latter model of the central engine, Usov and Katz (2000) proposed that GRBs may be accompanied by very bright, short duration ($\leqslant$ ms) radio bursts, which could be observed at frequencies of tens of MHz. Detection of such radio emission from a GRB at a cosmological distance could provide a probe for understanding both the ionised intergalactic medium (IGM) and GRB physics (Palmer, 1993; Ioka, 2003; Ghirlanda et al., 2006). However, Macquart (2007) showed that observations of short duration radio pulses from GRBs at low radio frequencies ($\sim 10 - 100\,\mathrm{MHz}$) would be significantly limited by scattering effects because the radio emission passes through the dense stellar wind of the progenitor or the immediate interstellar medium surrounding the source. Macquart (2007) showed that these propagation effects alter the properties of radiation with brightness temperature $\gg 10^{10}\,\mathrm{K}$, which may hinder the detectability of any radio pulse.

Recently, Zhang (2014) proposed that GRBs (with a magnetar as the central engine) could produce short duration radio pulses when the supra-massive neutron stars undergo rapid spin down (due to strong magnetic fields) within $10^2 - 10^3$ s of their birth, collapsing into black holes as they lose centrifugal support. These short duration radio pulses are proposed to be detectable at radio frequencies ranging from 1.2 to 1.5 GHz, if they are not absorbed by the GRB blast wave in front of the emission region. Zhang (2014) suggests that a small fraction of short duration radio pulses could be physically connected with GRBs.

In recent years, there have been number of detections of non-repeating short duration radio pulses. The dispersion measures (DM) of these pulses are so large that the progenitors are suggested to be extragalactic in origin (Lorimer et al., 2007; Keane et al., 2012; Thornton et al., 2013; Spitler et al., 2014). Seven out of six FRBs mentioned above were detected by the 64-m Parkes radio telescope and its 13-beam receiver, creating concerns about the astrophysical origin of the pulses. Most recently, Spitler et al. (2014) reported a discovery of a seventh FRB in the 1.4 GHz Pulsar ALFA survey with the 300 m Arecibo telescope, the first FRB discovered from a geographical location other than Parkes.

None of the FRBs from Parkes or Arecibo to-date have been associated with a GRB, although the theoretical possibility that they might be connected has motivated several experiments to look for coincident GRB/FRB emission. Bannister et al. (2012, hereafter B12) performed a targeted survey to detect short duration radio pulses from GRBs at 1.4 GHz. B12 observed nine GRBs, both long and short, using a 12 m radio telescope located at the Parkes Observatory. B12 reported the detection of two single radio pulses from two long GRBs with a sig-

nificance of 6.2σ and 6.6σ. The pulses were detected 524 and 1076 seconds after the γ-ray emission from the GRBs. The DMs of the pulses were 195 pc cm^{-3} and 570 pc cm^{-3}, which are large compared to the expected Galactic electron-density contribution (Cordes and Lazio, 2002) to the DM, indicating the possibility that the bursts are extragalactic in origin and possibly from the GRBs.

Similar to the B12 experiment, there have been a number of past and ongoing experiments searching for FRB-like emission from the prompt phase of GRBs at low and high radio frequencies (Obenberger et al., 2014; Staley et al., 2013; Balsano, 1999; Dessenne et al., 1996; Benz and Paesold, 1998; Baird et al., 1975). Baird et al. (1975) observed 19 GRB events at 151 MHz between 1970 and 1973, with a time resolution of 0.3s; they searched for coincident radio pulses with two or more stations over periods -1hr to $+10$hr relative to the GRB event times. Their search failed to locate any astronomical radio pulse above their sensitivity limit of 10^5 Jy. Two other GRBs were observed by Dessenne et al. (1996), who performed an automatic rapid radio follow-up experiment at 151 MHz, with a time resolution of 1.5 s; they reported a non-detection at a sensitivity of 3σ of 73 Jy. Benz and Paesold (1998) observed 7 GRBs between 1992 and 1994, covering a large range of frequencies between 40 and 1000 MHz using three similar spectrometers, with a time resolution of 0.15 s. Although the experiment sensitivity was low (10^5 Jy), the spectral coverage made this experiment very interesting. Similarly, Balsano (1999) observed 32 GRBs at 73.75 MHz from 1997 to 1998 and had a wide range of sensitivity for each GRB. They reported a non detection at sensitivity limit of ~ 200 Jy for integration times of 50 ms.

Most recently, Obenberger et al. (2014) reported the observations of 12 GRBs at 74 MHz, five GRBs at 52 MHz, and 17 GRBs at 37.9 MHz with a time resolution of 5 s. Similarly, Staley et al. (2013) reported the observation of four GRBs at 15 GHz with a time resolution of 0.5 s. Both Staley et al. (2013) and Obenberger et al. (2014) did not detect any FRB-like emission from the observed GRBs.

The sensitivities of the above mentioned experiments were generally low, however they have motivated a number of follow-up experiments including this work and a recent follow up project proposed by Bannister et al (2013) (VLBA project codes BB317 and BB325)[1] to use one or more Very Long Baseline Array (VLBA; Napier et al. (1994)) dishes to automatically follow up GRB alerts during telescope idle time. The VLBA-GRB experiment searches for FRBs using the existing V-FASTR system (Wayth et al., 2011).

[1]https://safe.nrao.edu/wiki/bin/view/VLBA/ProposalsAndDispositions

In this chapter, we describe observations performed at 2.3 GHz using the Hobart 26 m radio telescope to search for FRBs associated with GRBs. We designed our experiment to be similar to the B12 experiment with some improvements. Our aim was to observationally test the possible association of FRBs with GRBs and compare our results with the B12 results. Section 3.2 of this paper describes the observations performed. A detailed description of our single pulse search pipeline and verification is given in section 3.3. In section 3.4 we analyse our results and compare them with the B12 results. Conclusions are presented in section 3.5.

3.2 Observations

We observed the five GRBs listed in Table 3.1 at a central frequency of 2.276 GHz, using the 26 m radio telescope located at the Mount Pleasant Radio Observatory operated by the University of Tasmania[2] near Hobart, Tasmania. A computer at the observatory is configured to receive GRB notifications via email from the Gamma-ray Coordination Network (GCN)[3]. The GCN system distributes the location of the GRBs detected by space-borne observatories such as Integral (Winkler et al., 2003), Swift (Gehrels et al., 2004), Agile (Tavani et al., 2009) and Fermi (Atwood et al., 2009) in real time. A filter is applied to accept notices only from the Swift satellite, hence the GRBs listed in the Table 3.1 are all observed by the Swift satellite. The gamma-ray Burst Alert Telescope (BAT) on Swift first detects the GRB and localizes the burst direction to an accuracy of $\sim 3'$. These are the co-ordinates used by the telescope control system. Given that the radio telescope's primary beam Full Width at Half Maximum (FWHM) for this experiment is about 0.35°, all the observed GRBs in this experiment fall within the beam. Only GRBs that are above the elevation limit (12°) and within the visible range of the telescope ($-90° < \delta < +30°$) are observed. When an accessible GRB is identified, the telescope slews to the listed coordinates and then starts recording data. On average it takes approximately 140 seconds for the telescope to slew to the required location.

Data were recorded using the Australian Long Baseline Array (LBA) Data Acquisition System (DAS)[4] (Phillips et al., 2009). The LBA DAS has a sampler and digital filter which receives two independent analog intermediate frequencies (IFs), the right and left circular polarised signals over a 64 MHz bandwidth. The

[2] www.ra-wiki.phys.utas.edu.au

[3] www.gcn.gsfc.nasa.gov

[4] www.atnf.csiro.au/technology/electronics/docs/lba_das/lba_das.html

Table 3.1: Details of five GRBs observed using the 26 m radio telescope. P_{BAT} is the BAT position uncertainity, T_{BAT} is the time when BAT detected a GRB, T_{alert} is the time when the GCN alert notifications were sent, T_{90} is the GRB duration based on the BAT light curve, T_{rec} is the time when the recorders at 26-m Hobart telescope started recording the data from the source, T_{obs} is the observation duration with the radio telescope and T_{XRT} is the time when X-ray data were recorded by the XRT on Swift.

Source	α (J2000.0)	δ (J2000.0)	P_{BAT} (arcmin)	Trigger Date	T_{BAT} (UT)	T_{alert} (UT)	T_{90} (s)	T_{rec} (UT)	T_{obs} (s)	T_{XRT} (UT + s)
GRB 111212A	$+20^h\ 41^m\ 37^s$	$-68°\ 37'\ 01''$	3	2011-Dec-12	09:23:07	09:24:06	30.86	09:24:50	1200	T_{BAT} + 2856
GRB 120211A	$+05^h\ 51^m\ 00^s$	$-24°\ 45'\ 32''$	3	2012-Feb-11	11:58:28	11:59:29	101	12:03:10	1800	T_{BAT} + 119.5
GRB 120212A	$+02^h\ 52^m\ 25^s$	$-18°\ 01'\ 29''$	3	2012-Feb-11	09:11:22.74	09:11:43	20.42	09:13:20	1800	T_{BAT} + 2676
GRB 120218A†	$+21^h\ 19^m\ 02^s$	$-25°\ 27'\ 00''$	3	2012-Feb-18	00:49:22.14	00:50:17	7	00:52:10	1800	-
GRB 120224A	$+02^h\ 43^m\ 54^s$	$-17°\ 47'\ 32''$	2.4	2012-Feb-24	04:39:56.49	04:40:40	2.06	04:42:00	1800	T_{BAT} + 109.1

† No XRT light curve due to Sun observing constraints. Swift could not slew to the BAT position until 19:14 UT on 20-02-12.

analog IFs are sampled and digitised to 8 bit precision and then re-sampled to 2 bits using digital filters (Phillips et al., 2009) before the digital representation of the voltage is recorded to computer disk. The pointing error of the 26 m telescope across the whole sky is $\backsim 21''$.

For each observation the system equivalent flux density (SEFD) of the telescope was measured to be 800-900 Jy, which is calculated as SEFD $= \frac{8\,\mathrm{k_B}\,\mathrm{T_{sys}}}{\eta_\mathrm{a}\,\pi\,\mathrm{D^2}}$ where $\mathrm{T_{sys}}$ is the system temperature ($92 - 103\,\mathrm{K}$), $\mathrm{k_B}$ is the Boltzmann constant, η_a and D are the antenna efficiency (0.6) and the diameter of a circular aperture antenna (26 m), respectively. The automatic gain control loops were turned off for the duration of the observations. The one sigma flux density sensitivity for the 26 m telescope (to detect a pulse of width 25 ms) is approximately 0.5 Jy, calculated as $\sigma = \frac{\mathrm{SEFD}}{\sqrt{\triangle \mathrm{f}\,\triangle \mathrm{t}\,\mathrm{n_p}}}$ where $\triangle f$ and $\triangle t$ are the bandwidth (64 MHz) and integration time (25 ms), respectively, and $\mathrm{n_p}$ is the number of polarisations (2).

Comparing our experiment and 64-m Parkes radio telescope sensitivities to detect a 1 ms pulse. The 10 sigma flux density sensitivity of our experiment to detect a 1 ms pulse would be 25 Jy. This implies our experiment is sensitive to FRB detected by Lorimer et al. (2007), but not the other FRBs detected by Keane et al. (2012); Thornton et al. (2013) using 64-m Parkes radio telescope and the FRB detected by Spitler et al. (2014) using a 300-m Arecibo radio telescope.

The observations occurred over a period of 30 minutes for each GRB except for GRB 111212A which was observed for 20 minutes. Following observation of the GRB field, the telescope slewed to a nearby calibrator[5] and data were recorded for 20 minutes. A control observation was then undertaken by pointing the telescope at blank sky ($\sim 2^\circ$ away from the GRB position) for approximately 20 minutes and recording the voltage data.

3.3 Processing and Verification

The recorded data were transferred to the petabyte data storage facility at iVEC[6], in Perth. Data processing was performed on the Curtin University Parallel Processor for Astronomy (CUPPA), a 20 node computer cluster operated by Curtin University.

[5] LBA calibrators list- www.atnf.csiro.au/vlbi/observing/fringefinders.html
[6] www.ivec.org/about/

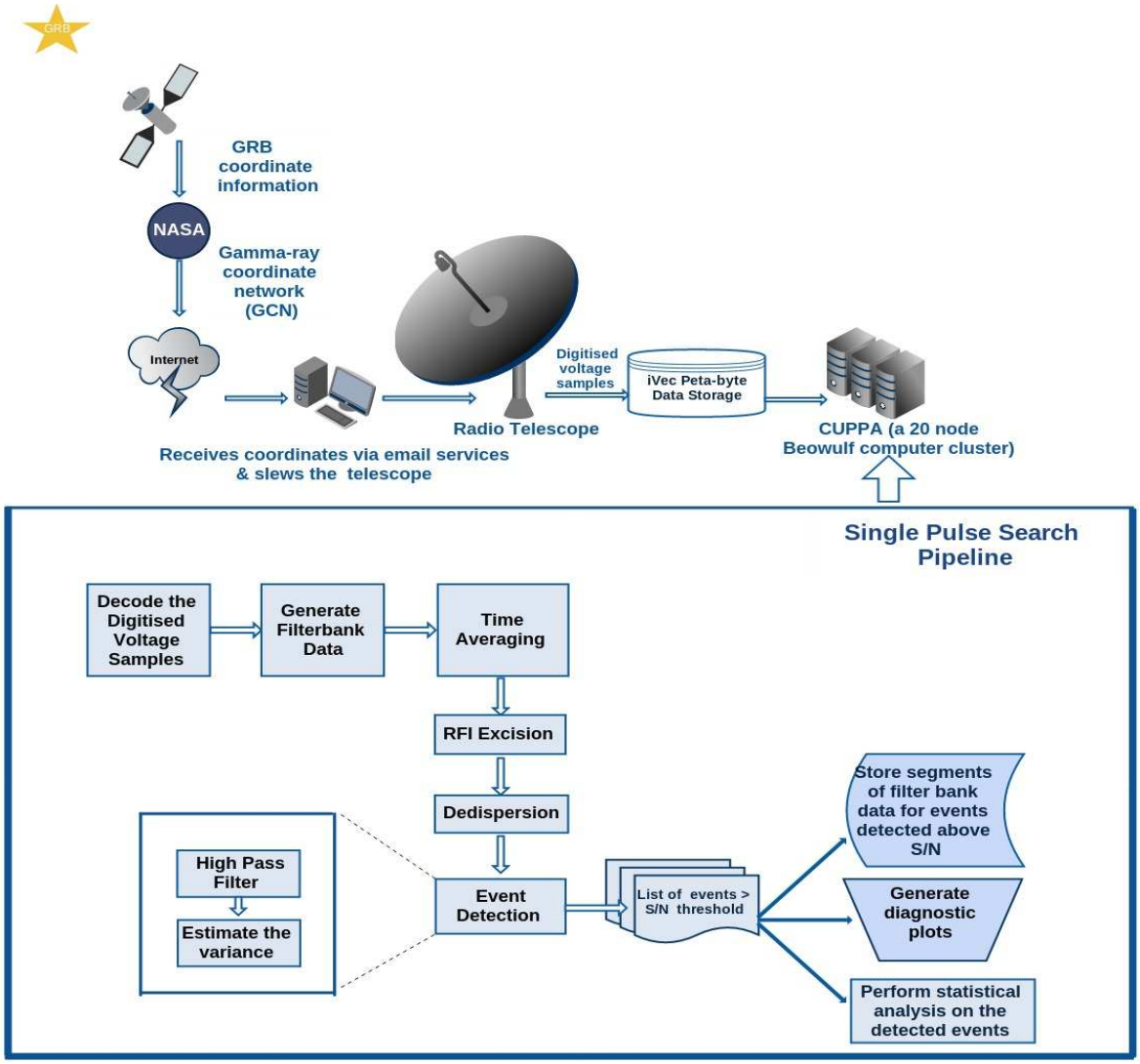

Figure 3.1: *Top panel*: A schematic representation of the system where the space-borne GRB telescope sends the position information for GRBs to our ground-based radio telescope through GCNs. The radio telescope is then slewed to the GRB positions and data are recorded. The recorded data are then transferred to the PetaByte data storage facility at iVEC, in Perth and processed on a 20 node Beowulf computer cluster, CUPPA. *Bottom panel*: Represents the single pulse search pipeline implemented in this paper, to search for FRBs from GRBs. The search pipeline has multiple stages: correlation; time averaging; radio frequency interference (RFI) excision; dedispersion; event detection and classification. In this experiment we generate time averages ranging from 640 μs to 25.60 ms (section 3.1.2). Each averaged time series go through the RFI excision, dedispersion, event detection and clasification stages independently.

3.3.1 Single Pulse Search Pipeline

In this section we describe the data processing pipeline (Figure 3.1) used to search for single short duration radio pulses in our data. The search pipeline has multiple stages: correlation; time averaging; radio frequency interference (RFI) excision; dedispersion; event detection; and classification of events. Several of our tools were reused from the V-FASTR experiment (Wayth et al., 2011) which can read LBA data natively.

Correlation

The first step in the processing pipeline was to pass the data through a spectrometer to form channelised total power for each polarisation. The 2-bit digitised voltage samples from each polarisation were decoded and sent to a software correlator. The correlator is an FX design with a configurable number of spectral channels and averaging time. We used 128 $\times$ 0.5 MHz spectral channels, formed via FFT, and an averaging time of 640 μs. The output of the software correlator was written to files for subsequent processing.

Time Averaging

The intrinsic width of pulses are generally unknown. Because the dispersion and scattering affects the observed width of the pulse, a large parameter space of pulse widths must be searched (Cordes and McLaughlin, 2003). To obtain optimal sensitivity, the correlated time series were averaged for pulse widths ranging from 640 μs to 20.48 ms. This was achieved by averaging 2^n time samples together, where n ranges from 0 to 5, and searching each averaged time series independently. An additional time averaged series was generated at 25.60 ms by averaging 40 time samples together (which is not a power of 2), to match the width used by B12 in their experiment.

RFI Excision

Observations at 2.3 GHz are generally affected by Radio Frequency Interference (RFI) from terrestrial transmitters, radars, satellites etc., which changes the total power as a function of frequency and time. Therefore, identification and excision of RFI was undertaken.

First, we excise the time samples in each frequency channel that were affected by sporadic RFI. The top panel of Figure 3.2 shows an example of sporadic, wide-

band RFI, where the power level in all the frequency channels over short time scales (in this case ~ 4 ms) is much higher when compared to the typical mean power in neighbouring time samples across the frequency band. The top panel of Figure 3.3 shows an example of sporadic narrow-band RFI, where the power level in a frequency channel over a short time (in this case $\sim 640\,\mu$s) is high when compared to the typical mean power in the neighbouring time samples in that frequency channel. Our RFI excision algorithm used a thresholding method to identify samples in the time domain which were affected by RFI. First, we calculated the local variance (σ_l^2) of the time samples in each frequency channel over an adjustable time range (~ 10 sec) and then compared to the power (amplitude) of each time sample. The time samples that exceeded a pre-set threshold (here the threshold was set to $5\sigma_l$) were excised from the time series and replaced with the mean power value estimated for each frequency channel over the band. We conservatively chose a $5\sigma_l$ threshold for RFI excision, because we did not want to clip the thermal noise distribution[7]. The bottom panels of Figures 3.2 and 3.3 show the results of our excision algorithm.

Next, we manually identified and excised persistent narrow-band RFI which are constant in time over a frequency channel. The top panel of Figure 3.2 shows an example of persistent narrow band RFI where the power in a frequency channel is higher compared to the power in the neighbouring channels across the frequency band. The affected channels, including the lower band edge spectral channel (DC channel generally has spurious high power due to sampler offsets), were recorded in a flagging file. The dedisperser (the next stage in the pipeline) reads the flagging files for bad channels and ignored the bad channels in further processing. We repeated the RFI excision process on all the time averaged data series.

Dedispersion

The next step in the pipeline is dedispersion. Any incoming astronomical impulsive radio signal will, in general, be dispersed in time across the spectral channels due to the ionised component of the interstellar and intergalactic media (Lorimer and Kramer, 2012). The intrinsic signal can largely be recovered by incoherent

[7] Assuming the power level in the data follows the normal distribution, the probability of detecting an event above some significant threshold due to thermal noise fluctuations in the data is determined using the cumulative distribution function (see section 3.4.2). Thus the probability of detecting an event $> 5\sigma$ is 2.87×10^{-7} and for $> 3\sigma$ the probability is 1.3×10^{-3}. We have $\sim 2 \times 10^6$ independent samples, therefore, at 5σ we would be effectively clipping ~ 1 sample as a false positive, compared to when a 3σ threshold is chosen we would be effectively clipping $\sim$2600 samples. This could skew the thermal noise distribution in the data.

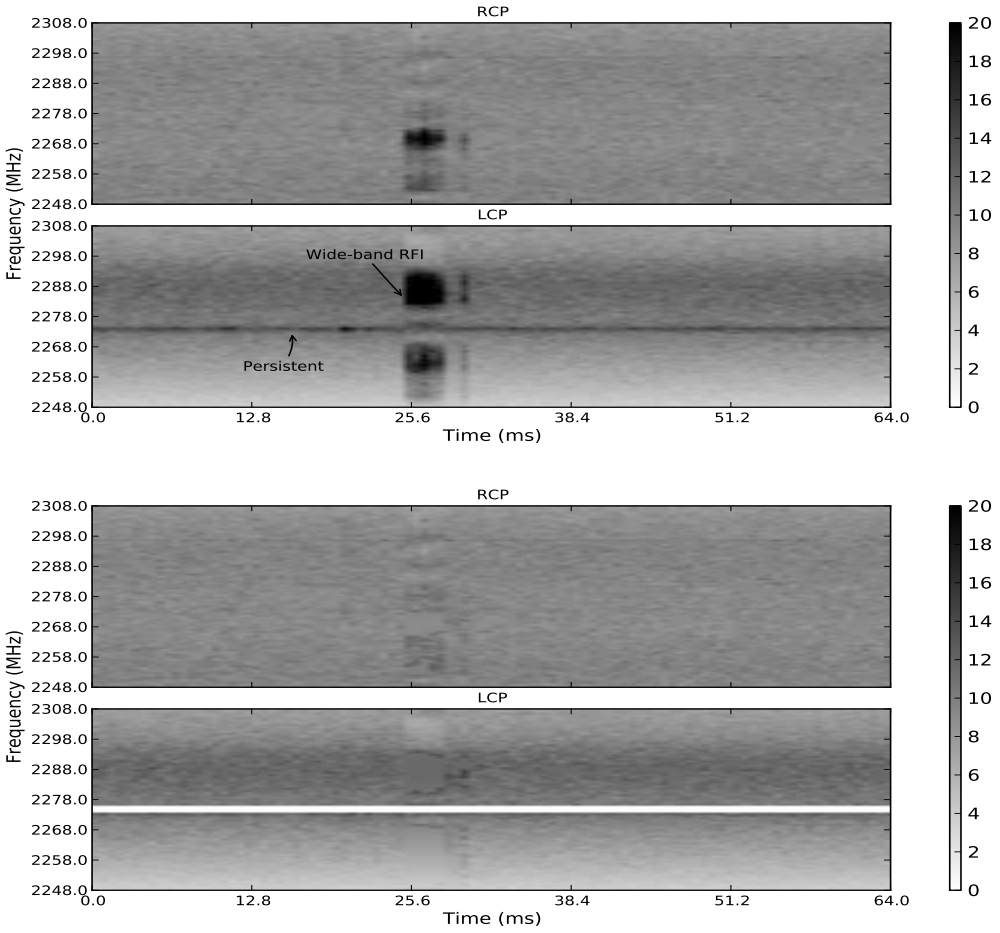

Figure 3.2: Example dynamic spectrum shows RFI excision. Intensity is arbitrary power units. *Top panel*: an example of a wide band RFI and persistent narrow band RFI. *Bottom panel*: shows the results of RFI excision algorithm on the data.

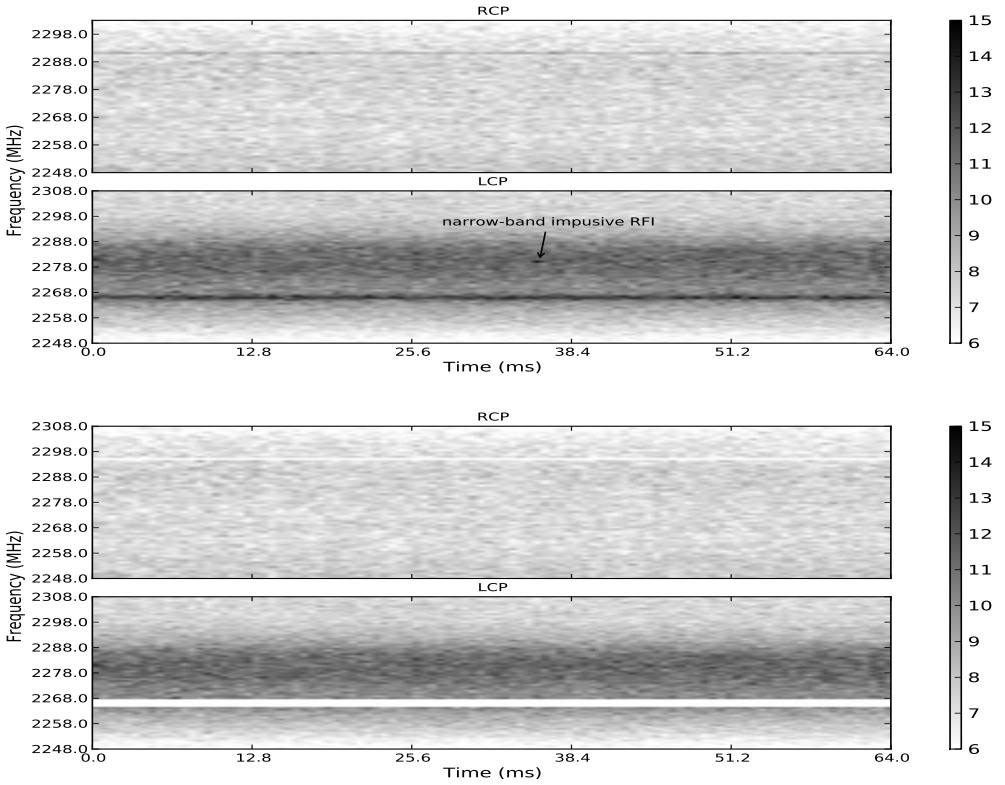

Figure 3.3: Example dynamic spectrum shows RFI excision. Intensity is arbitrary power units. *Top panel*: an example of a narrow band impulsive RFI. *Bottom panel*: shows the results of RFI excision algorithm on the data.

dedispersion, by applying an appropriate time delay for each spectral channel and adding power across all the spectral channels. The time delay between two frequencies is given by $\Delta t = 4.15\,\mathrm{ms} \times \mathrm{DM} \times (\nu_{\mathrm{lo}}^{-2} - \nu_{\mathrm{hi}}^{-2})$, where the DM (pc cm^{-3}) is the integrated column density of free electrons along the line of sight and ν_{lo} and ν_{hi} are the low and high frequencies in GHz, respectively (Lorimer and Kramer, 2012).

We use DART (Dedisperser of Autocorrelations for Radio Transients) to perform the incoherent dedispersion, a detailed description of which is given by Wayth et al. (2011). The incoming data to DART are ordered in frequency and time for each polarisation. The dedispersion process sums the power across channels, with the delay for each channel according to the frequency and DM. At the output, DART combines both polarisations and generates a dedispersed time series for each DM. We dedisperse the data with DM steps as listed in Table 3.2 ranging from 0-5000 pc cm^{-3}. The choice of DM steps was made by setting the time delay (Δt) between highest (ν_{hi}) and lowest (ν_{lo}) spectral channels equal to the data sampling time (integration time). Choosing DM steps smaller than the data sampling time leads to highly correlated time samples, since the dedispersed time series are virtually identical for neighbouring DM steps. DART is flexible when compared to the Taylor tree algorithm (Taylor, 1974), because it can dedisperse the signals beyond the diagonal DM, the DM where the gradient of the dispersion curve is one time sample per spectral channel. The DM steps across the DM range are linearly distributed for the first few DM steps, before progressing geometrically, with a growth rate of 1.02 (i.e $\mathbf{DM_i = DM_i * 1.02}$). This results in equal spacings at lower DM and increasingly larger spacings at higher DM. Table 3.2 summarises the number of DM steps used for each time average.

Table 3.2: For each time average, the table lists the number of DM steps used to dedisperse the data.

Time Averaging (ms)	N_{DM}
0.64	149
1.28	114
2.56	79
5.12	45
10.24	23
20.48	12
25.60	9

Event Detection

The next step in the pipeline is detection. After dedispersion, each time series is searched for events above a defined signal to noise threshold. In the detector, the time series are divided into small time segments (~ 1.3 s). We chose this length of time because visual inspection of the data showed that the total power sometimes changed on time-scales longer than this. If longer time segments were used this would artificially raise the variance estimate. Each time segment is high-pass filtered, by subtracting a 100 timestep moving average from each sample. This reduces any long term power variations due to system temperature (T_{sys}) changes - atmosphere, receiver response etc., which may bias variance estimates on time scales of 100s of samples, while retaining sensitivity to short time scale variations. We note that the high-pass filter window is longer than the expected pulse width of an astronomical event.

Each dedispersed time segment is then searched for single events $> 5\sigma$. The noise level of the time series for each DM step is estimated using the standard deviation. We also tried the robust trimmed estimator, interquartile range (IQR) (Fridman, 2008), to estimate the noise level for each DM step. The number of events detected $> 5\sigma$ from the IQR and standard deviation techniques did not differ. We adopt use the standard deviation because the behaviour of this statistic is well understood when a finite number of samples are used for its estimation.

Classification of Detected Events $> 5\sigma$

The next step in the pipeline is the classification of detected events $> 5\sigma$. Figure 3.4 demonstrates the differences between the signatures of astronomical signals, low level RFI and thermal noise fluctuations in the DM/time plane. An astronomical signal is expected to show reduced S/N for DM steps away from the true DM (Cordes et al., 2004). The astronomical signals are broad band and any signals well above the minimum detection threshold are expected to be seen in multiple DM steps for a given time average and also in the consecutive time averages. Events due to thermal noise fluctuations will be seen at a single DM step and follow Gaussian statistics (most of the events would be close to the S/N threshold). Events due to low-level RFI will appear in multiple DM steps, but do not have the characteristic peaked shape that a bright pulse from an astronomical source would have.

The recorded events $> 5\sigma$ from our detection pipeline for all the time averages were visually examined for signatures of astronomical signals, low level

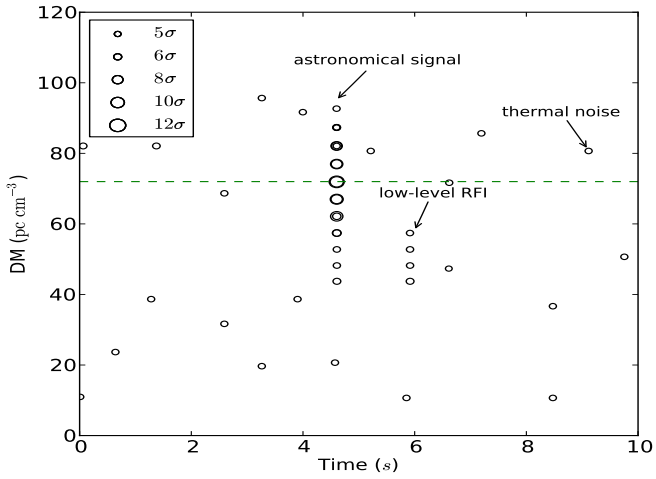

Figure 3.4: An example diagnostic plot that demonstrates the difference between the signatures of astronomical signals,low level RFI and thermal noise fluctuations in the DM/time plane. The astronomical signal shows reduced S/N for DM steps away from the true DM (dashed line). The events due to thermal noise fluctuations appear at a single DM step. The events due to low level RFI are detected across multiple DM steps, but do not have the characteristic peaked shape that a bright pulse from an astronomical source would have. The size of the circles is proportional to the S/N.

RFI and thermal noise fluctuations using the diagnostic plots and were classified respectively.

3.3.2 Single Pulse Search Pipeline Verification

To test our single pulse search pipeline we used archival observations of the pulsar PSR J0835-4510 (the Vela pulsar). Observations were made using the same 26m radio telescope as used for our GRB observations. The data recording system used was also identical to the recorder used for the GRB observations. Vela was observed at a central frequency of 1440 MHz with right and left circular polarisations over a 64 MHz bandwidth. Vela has a steep spectral index, $\alpha = -1.2$ ($S \propto \nu^{\alpha}$), DM = 67.99 pc cm^{-3} and a period of 89.3 ms (Manchester et al., 2005).

The recorded voltage data were correlated at 640 μs time resolution and 128 spectral channels, the same as for the GRB data. The correlated data were dedispersed over a DM range of 0-200 (pc cm^{-3}), with 40 DM steps. The dedispersor output was searched for pulses above the S/N threshold of 5 at 640 μs time averaging and resulting events were examined to determine if they were real pulses from the pulsar in the time/DM plane (Figure 3.5). Individual pulses were detected at DM $\sim$ 67 pc cm^{-3} and at neighbouring DM steps with reduced S/N as expected. Segments of data were written out for each candidate pulse for further investigation. In the follow-up process, candidates were visually inspected via dynamic spectrum plots similar to those shown in Figure 3.6. The dynamic spectrum shows individual dispersed pulses with a period of 89.3 ms in time across the frequency band. Therefore, we have confirmed detection of individual pulses with Vela's period and DM via our single pulse search pipeline.

3.4 Results and Discussion

3.4.1 Results

Here we discuss the results of our search for FRBs associated with GRBs using the single pulse search pipeline. The five GRBs have $T_{90} > 2$ s based on the light curves from BAT. Processing the five data sets and visually inspecting the events via diagnostic plots did not show any signatures of astronomical signals. All the events detected by our detector were between 5σ and 6σ and no events $\geq 6\sigma$ were detected. Table 3.3 lists the number of $> 5\sigma$ events for all the GRBs and time averages, respectively. Figure 3.7 shows an example diagnostic plot which

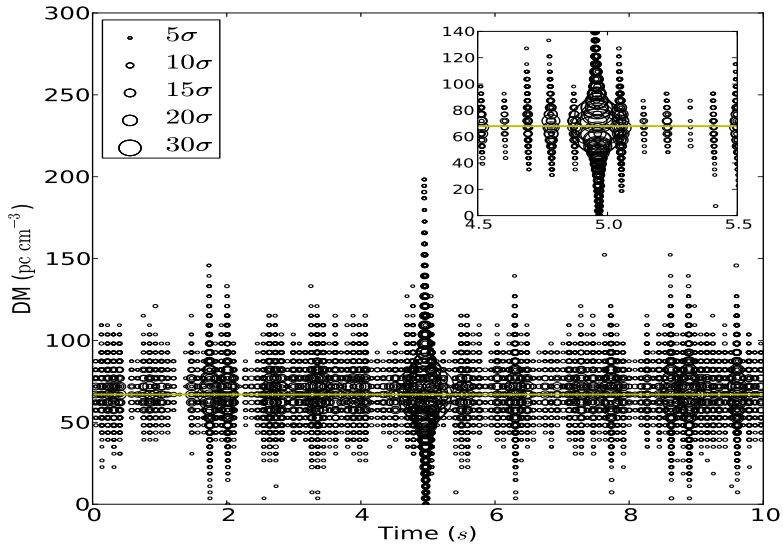

Figure 3.5: Vela pulsar events detected $> 5\sigma$ vs DM (pc cm^{-3}) as a function of time. The size of the circles are proportional to the signal to noise ratio. Single pulses from Vela are detected at the true DM (horizontal line) and across multiple DM steps with reduced S/N.

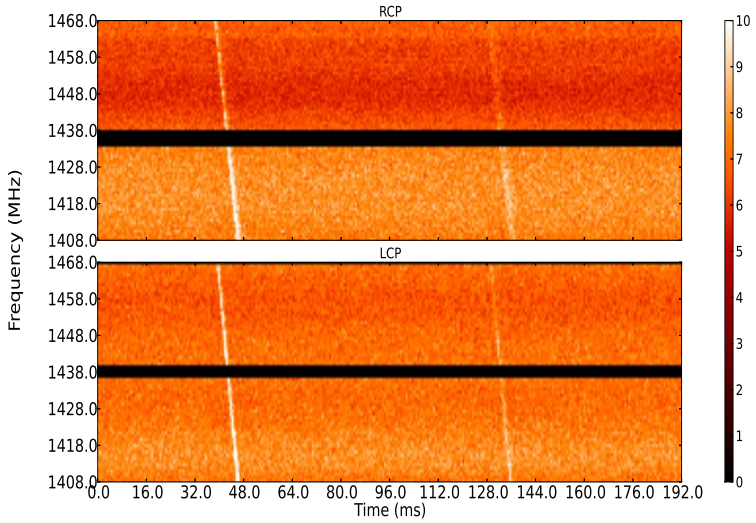

Figure 3.6: Dynamic spectrum for Vela pulsar, time vs frequency. The colorbar represents the channel power in arbitary units. A strong pulse is seen at the left of the plot followed by a relatively weak pulse, correct period for separated by $\sim$ 89.3 ms which is the correct period for Vela.

illustrates the distribution of detected events $> 5\sigma$ for GRB 120211A at 1.28 ms time average.

In the absence of a characteristic signature of a astronomical signal $> 6\sigma$, we performed a statistical analysis on events between $5 - 6\sigma$ to check if they were consistent with expectations due to thermal noise fluctuations. This analysis gives us confidence that our search pipeline is working correctly and highlights the importance of sample variance in determining the significance of an event.

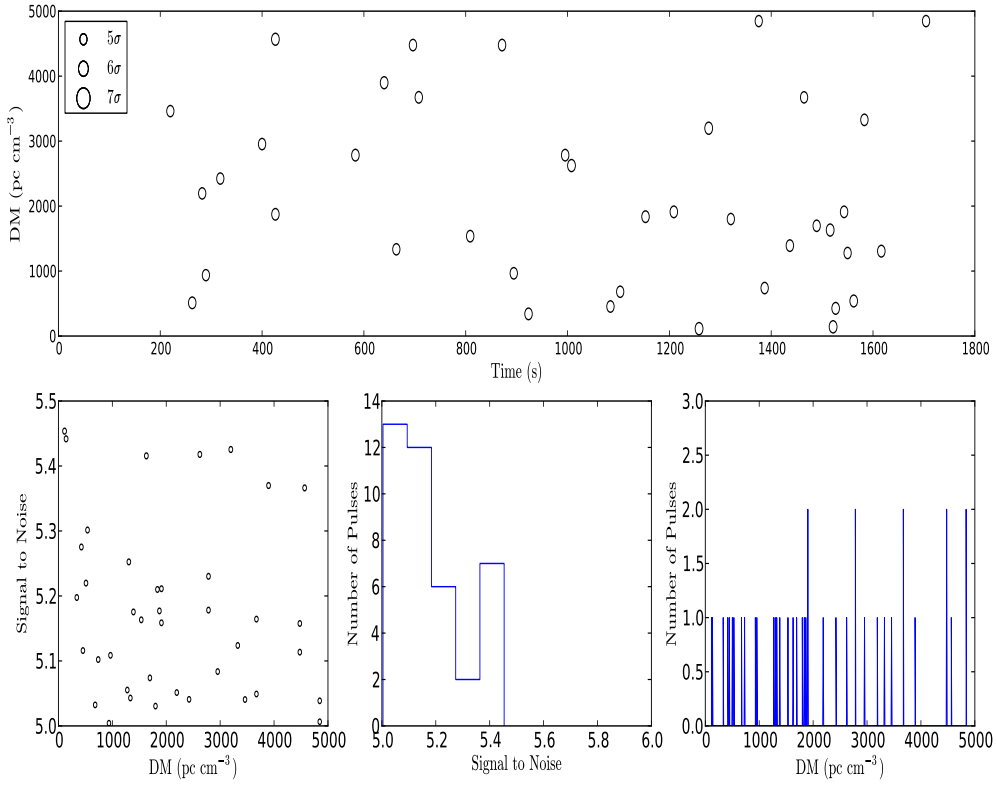

Figure 3.7: Example diagnostic plot which illustrates the distribution of detected events $> 5\sigma$ for GRB 120211A at 1.28 ms time average. *Top panel*: All events with S/N $> 5\sigma$ plotted vs DM and time. The size of circles are proportional to the S/N of the events. *Lower left panel*: Scatter plot of the DM and S/N. *Lower middle panel*: Distribution of the detected events $> 5\sigma$. *Lower right panel*: Number of detected events $> 5\sigma$ vs DM.

3.4.2 Statistical Analysis of the Detected Events $> 5\sigma$

Here we compare the number of events expected due to thermal noise fluctuations to the number of events recorded by our pipeline. The number of events expected due to thermal noise fluctuations, $\mathrm{N_E(I)}$, above the detection threshold is given by,

$$\mathrm{N_E(I} > 5\sigma) = \mathrm{N_t\, N_{DM}\, P(I} > 5\sigma), \tag{3.1}$$

where $\mathrm{N_{DM}}$ is the number of independent DMs, $\mathrm{N_t}$ is the number of independent time samples, and $\mathrm{P(I} > 5\sigma)$ is the probability of an event above 5σ due to thermal noise fluctuations (assuming the power fluctuation due to thermal noise follows the Gaussian distribution), and is given by the cumulative distribution function (CDF),

$$\mathrm{P(I} > 5\sigma) = \int_{5\sigma}^{\infty} \mathcal{N}(\mu, \sigma^2) = \frac{1}{2} + \frac{1}{2}\mathrm{erf}\left[\frac{\mu - 5\sigma}{\sqrt{2}\sigma}\right], \mathrm{labelprob} \tag{3.2}$$

where erf is the error function and $\mathcal{N}(\mu, \sigma^2)$ is the Gaussian distribution with mean μ and variance σ^2.

Independent DM steps In Equation 3.1, we note that the $\mathrm{N_{DM}}$ steps should be independent. Given our choice of step progression we expect $\sim 50\%$ of power samples to be identical between consecutive pairs at lower DM steps (Figure 3.8). Here we perform an analytical calculation showing that the time series in each DM step at the lower end of the DM range can be treated as independent.

Our calculation assumes that a 5σ noise event is detected due to the addition of power sample fluctuations in the time/frequency plane. Based on this assumption we consider the following scenarios: (i) The probability of two consecutive DM steps each having a 5σ event, since $\sim 50\%$ of power samples are identical at the lower DM; and (ii) The probability of two DM steps separated by one DM step each having a 5σ event, since $\sim$ 25 % of power samples are identical at lower DM. In the former case, the probability is reduced by a factor of ~ 100 compared with a single 5σ event in a DM step due to thermal noise fluctuations. In the latter case, the probability indicates that events $> 5\sigma$ are consistent with events due to thermal noise fluctuations reduced by $\sim 10^6$ (a detailed description of the calculation is given in Appendix A). The small probability in the former and latter scenarios implies that 5σ detections in two or more DM steps at the lower end of the DM range are independent.

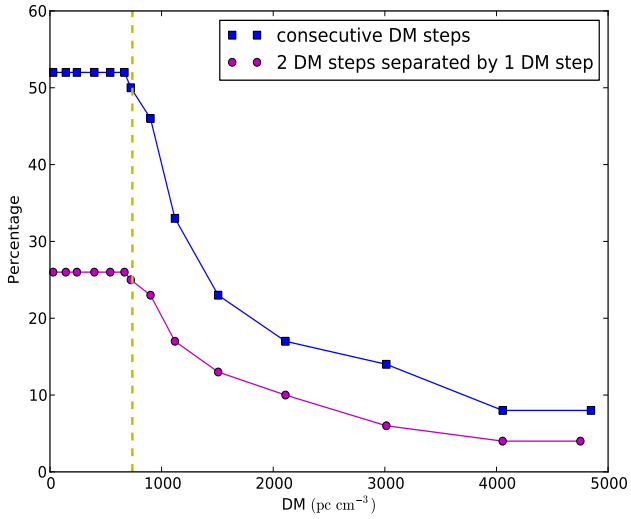

Figure 3.8: Percentage of identical power samples between consecutive DM steps at 640 μs time average.7 At lower DM (where DM steps are linearly distributed) $\sim$ 51- 52 % of power samples are identical between the consecutive DM steps and $\sim$ 26-27 % of power samples are identical between the two DM steps separated by one DM step. However, at the higher DM (where DM steps are exponentially distributed) the number of identical power samples between DM steps reduces, which leads to less correlation in the dedispersed time series. The vertical dashed line represents the transition in the distribution of the DM steps from linear to exponential.

Uncertainties in the Estimation of $\mathrm{N_E(I > 5\sigma)}$

The expected number of events due to thermal noise fluctuations, $\mathrm{N_E(I > 5\sigma)}$, is uncertain due to two effects: (1) Events detected due to thermal fluctuations are stochastic and their number is characterised by the Poisson distribution; (2) the variance measured from the data is a sample estimate, which has inherent uncertainty on the variance as it is being estimated over a finite number of samples. We take these effects into account in order to make our statistical analysis robust.

(1) *Stochasticity of 5σ events*: We note that the thermal noise is stochastic in nature, inducing an uncertainty in the estimation of $\mathrm{N_E(I > 5\sigma)}$ which can be quantified using the Poisson distribution. The probability of observing X events, when λ number of events is expected, is given by

$$\mathrm{Pois(X;\lambda)} = \frac{\lambda^{\mathrm{X}} \exp(-\lambda)}{\mathrm{X!}}. \tag{3.3}$$

For large λ, the Poisson distribution approximates the Gaussian distribution where $\mathrm{X} \sim \mathrm{Pois}(\lambda); \lambda \geqslant 15 \Rightarrow \mathrm{X} \sim \mathcal{N}(\lambda, \lambda)$. Therefore, for $\lambda \geqslant 15$ we use the Gaussian approximation and the uncertainty in the number of events fluctuates around the mean ($\lambda = \mathrm{N_E(I > 5\sigma)}$) with a standard deviation $\sqrt{\mathrm{N_E(I > 5\sigma)}}$. For $\mathrm{N_E(I > 5\sigma)} < 15$, the Gaussian approximation is invalid, and we use Monte Carlo simulations to estimate the uncertainties. This is described in section 3.4.2

(2) *Sample variance in estimating true signal variance*: A finite number of samples (N = 2048 time samples at the intrinsic temporal resolution) is used to estimate the mean and the standard deviation of the data. The true mean and standard deviation of the data are not known. This estimate has an associated uncertainty known as sample variance, because only a finite number of samples is used. The standard error on the estimation of the mean ($\triangle\hat{\mathrm{I}_0}$) and variance ($\triangle\hat{\sigma}^2$) for N independent samples from the true value is given by $\triangle\hat{\mathrm{I}_0} = \frac{\sigma}{\sqrt{\mathrm{N}}}$ and $\triangle\hat{\sigma}^2 = \sqrt{\frac{2}{\mathrm{N}-1}}\,\sigma^2$ respectively. The errors $\triangle\hat{\mathrm{I}_0}$ and $\triangle\hat{\sigma}^2$ are propagated into the expression for the cumulative probability (Equation 3.10) and the variance on the cumulative probability is obtained. For a detection threshold of 5σ, the variance is given by $(\Delta\mathrm{P})^2$,

$$(\Delta\mathrm{P})^2 = \frac{1}{2\pi}\exp(-5^2)\left(\frac{1}{\mathrm{N}} + \frac{5^2}{\mathrm{N}-1}\right), \tag{3.4}$$

where N is the number of time samples. The sample size must be large enough to minimize the sample variance, but should not be so large that the mean changes with in the sample which would artificially increase the variance estimate.

The uncertainty in the expected number of events due to sample variance is propagated to an uncertainty in $N_E(I > 5\sigma)$ using equations 3.1 and 3.6,

$$\Delta_N \equiv N_{DM}\, N_t\, \Delta P. \tag{3.5}$$

The two uncertainties in the estimate of $N_E(I > 5\sigma)$ are independent and Gaussian distributed, and therefore can be combined in quadrature,

$$\delta E^2 = (\sqrt{N_E(I > 5\sigma)})^2 \pm \Delta_N^2. \tag{3.6}$$

Estimating the significance of $N_A(I > 5\sigma)$ in two regimes

In the previous section, we combined the two uncertainties associated with the estimation of $N_E(I > 5\sigma)$ in quadrature, since both uncertainties obey Gaussian approximations. Here we would like to note again that the Gaussian approximation in case 1 is valid only for $N_E(I > 5\sigma) \gtrsim 15$. We observe from the Table 3.3 and 3.4 that for higher time averages ranging $5.12 - 25.5$ ms, $N_E(I > 5\sigma) < 15$, the Gaussian approximation for the uncertainty discussed in the section 3.4.2 is no longer valid. Therefore, for higher time averages ($5.12 - 25.5$ ms), we can not combine both uncertainties in quadrature.

To estimate the significance p of the observed events ($N_A(I > 5\sigma)$), we split the calculations into two regimes: (1) At lower time averages ranging 640μs - 2.56 ms were $N_E(I > 5\sigma) \gtrsim 15$, we calculate p via the Gaussian approximation with mean $N_E(I > 5\sigma)$ and variance δE, given by the equations 3.1 and 3.6 respectively; (2) At higher time averages ($5.12 - 25.5$ ms) where $N_E(I > 5\sigma) < 15$, we use results obtained via Monte Carlo simulation to estimate p. In both regimes, we interpret a $p > 0.05$ to be consistent with the null hypothesis which is that the observed events $N_A(I > 5\sigma)$ are consistent with noise.

In the low time average regime p is given by,

$$p = \frac{1}{2} - \frac{1}{2}\,\mathrm{erf}\left(\frac{N_A(I > 5\sigma) - N_E(I > 5\sigma)}{\sqrt{2}\,\delta E}\right). \tag{3.7}$$

Estimating Significance p via Monte Carlo Simulations for Higher Time Averages

To determine the significance of the observed events ($N_A(I > 5\sigma)$) at higher time averages (when $N_E(I < 5\sigma) < 15$), we use the Monte Carlo (MC) technique and perform 10^4 simulations of random data sets. The simulations were performed on the time averages in the range $5.12 - 25.60$ ms. The results of the simulations

automatically include the combined uncertainty due the thermal noise and sample variance.

Our program generates an array of Gaussian distributed random data sets of duration 30 minutes and n DM steps (where n is given in Table 3.2). The array is then passed through the event detection pipeline (described in detail in Section 3.3).

For each iteration the MC simulation detects events $> 5\sigma$. We performed 10^4 iteration for each time average. Figure 3.9 shows an example histogram for 5.12 and 10.28 ms time averages where we plot the events detected over 10^4 iterations. The values in each bin are normalised to plot the probability density function, such that the integral over the range is unity. The significance (p), is determined by integrating the values in the histogram greater than and equal to $\mathrm{N_A}(\mathrm{I} > 5\sigma)$ value for a given time average. For instance from Table 3.3, the number of events, $\mathrm{N_A}(\mathrm{I} > 5\sigma)$, recorded for GRB120211A is three at 5.12 ms time resolution. The significance of $\mathrm{N_A}(\mathrm{I} > 5\sigma)$ at the 5.12 ms time resolution can be calculated via the histogram summing the values greater than and equal to the bin number three (solid green line Figure 3.9a). The region in the histogram greater than and equal to $\mathrm{N_A}(\mathrm{I} > 5\sigma)$ value is termed the critical region[8] in statistics. Integrating the point probabilities greater than and equal to the critical value gives the significance p (Kay, 1998).

$\mathrm{N_E}(\mathrm{I} > 5\sigma)$ for each higher time average is given by the mean of the distribution, which is calculated by taking the average of values obtained through MC simulations. Here the duration of the random data sets was chosen to be the same as the observation duration for each GRB and blank sky data set.

Applying the Statistical Analysis on the Obtained Results

The statistical analysis was applied to all the GRBs for all averaging times. Table 3.3 presents the results of the analysis. In all cases $p > 0.05$, indicating that our recorded events are consistent with thermal noise fluctuations. In the absence of a characteristic signature of an astronomical pulse $> 6\sigma$, we conclude that the events $> 5\sigma$ are consistent with the expectations due to thermal noise fluctuations. There were no events with a statistically significant S/N.

Another approach to determine the probability of an event occurring due to thermal noise fluctuations is to measure the false positive rate when there is no

[8]Critical region in statistics is the portion of a statistics bloc where a null hypothesis is rejected via the results of a test of the hypothesis.

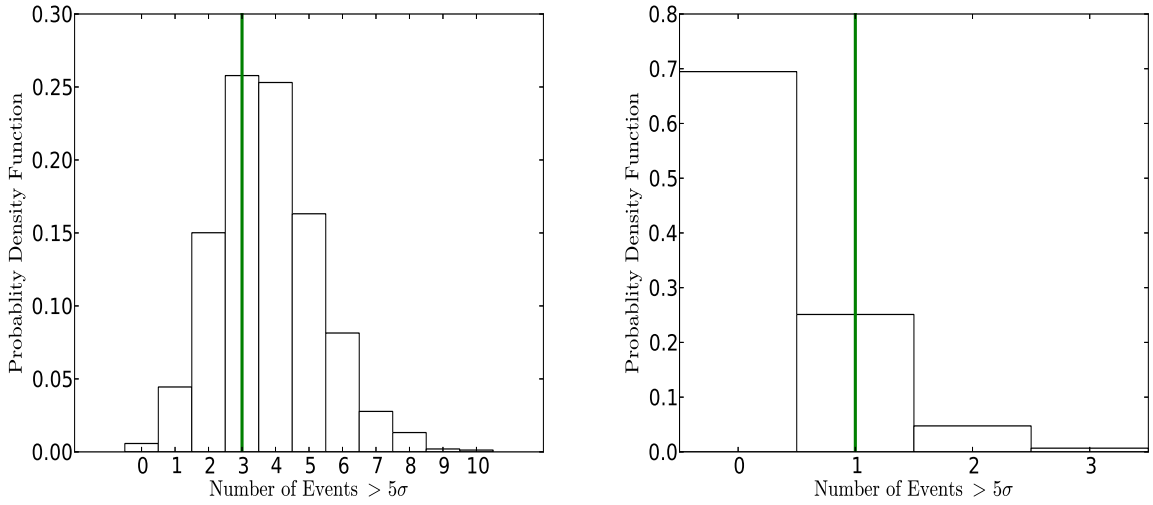

(a) 5.12 ms (b) 10.24 ms

Figure 3.9: *Left panel*: Example histogram obtained through MC simulations for GRB 120211A at 5.12 ms. The solid line in green represents the $N_A(I > 5\sigma)$ for GRB 120211A at 5.12 ms time average. *Right panel*: Example historgram obtained through MC simulations for GRB 120211A at 10.24 ms. The solid line in green represents the $N_A(I > 5\sigma)$ for GRB 120211A at 10.24 ms time average .

GRB in the beam. Observing a patch of blank sky after the GRB observation preserves the noise properties and RFI information, assuming that no source of astronomical impulsive radio emission is in the field of view. We analysed the data from the blank sky observations, which were processed in a manner identical to that described for the GRB data. Table 3.4 shows the results of our analysis for the blank sky datasets. Again, in all the cases $p > 0.05$ indicating that our recorded events are consistent with thermal noise fluctuations.

3.4.3 Discussion

In this section we compare our results with the B12 and other previous experiment results, to gain some understanding of the limits on FRB associated with GRBs and to give a quantitative assessment of the conclusions in B12.

Control Observation on Blank Sky

We have designed our experiment to be similar to B12 and have also made significant improvements. Firstly, unlike B12 we have undertaken control observations using blank patches of sky ~ 2 degrees away from the GRB positions. Secondly, the statistical analysis of the events detected from the blank sky gives estimates for the number of false positives due to thermal noise fluctuations and RFI. This method is more reliable when compared to the method adopted by B12 to account for the false positive rate by randomising the spectral channels, using data from the GRB observations. B12 showed that randomising the spectral channels would preserve the properties of thermal noise fluctuations, narrow band and wide band RFI, but the presence of impulsive RFI that spans multiple channels are destroyed. This will reduce the number of false positive events due to thermal noise fluctuations and RFI. This effect will be high if the rate of impulsive RFI that spans over multiple channels is high, which leads to an inaccurate estimation of false positives. However, the data from blank sky taken ~ 2 degrees away from the GRB positions preserves all the properties of thermal noise fluctuations and RFI including the periodic and aperiodic RFI that spans multiple channels. Also, the data go through the same RFI excision and detection algorithms as those used for the GRB data sets, which should provide a more reliable estimate of the false positive rates.

Table 3.3: A summary of the statistical analysis performed on all the GRB datasets. The subtables (a), (b), (c), (d), (e) list the time averages used in this experiments. The columns are: the source name, $N_E(I > 5\sigma)$ is the expected number of events above the S/N threshold due to thermal noise fluctuations, $N_A(I > 5\sigma)$ is the actual number of events detected above the S/N threshold, $\sqrt{N_E(I > 5\sigma)}$ and Δ_N are the uncertainites on the $N_E(I > 5\sigma)$, δE represents the uncertainities combined in quadrature, p is the significance where for $p > 0.05$ indicates that events $> 5\sigma$ are consistent with events due to thermal noise fluctuations. The significance p for the time averages at and above 5.12 ms were calculated via MonteCarlo simulations as described in section 3.4.2. $N_E(I > 5\sigma)$ for the time averages at and above 5.12 ms were estimated by taking the mean of the PDF in the histograms.

GRB Name	$N_E(I > 5\sigma)$	$N_A(I > 5\sigma)$	$\sqrt{N_E(I > 5\sigma)}$	Δ_N	δE	p
(a) 640 μs						
GRB 111212A†	83	85	9	49	49	0.48
GRB 120211A	125	120	11	70	70	0.53
GRB 120212A	125	125	11	70	70	0.50
GRB 120218A	125	129	11	70	70	0.48
GRB 120224A	125	128	11	70	70	0.48
(b) 1.28 ms						
GRB 111212A†	32	26	6	36	36	0.56
GRB 120211A	48	42	7	54	54	0.54
GRB 120212A	48	48	7	54	54	0.50
GRB 120218A	48	40	7	54	54	0.55
GRB 120224A	48	51	7	54	54	0.48
(c) 2.56 ms						
GRB 111212A†	11	12	3	18	18	0.48
GRB 120211A	16	12	4	26	26	0.56
GRB 120212A	16	22	4	26	26	0.41
GRB 120218A	16	18	4	26	26	0.47
GRB 120224A	16	22	4	26	26	0.56
(d) 5.12 ms						
GRB 111212A†	3	1	-	-	-	0.72
GRB 120211A	4	3	-	-	-	0.80
GRB 120212A	4	3	-	-	-	0.80
GRB 120218A	4	1	-	-	-	0.99
GRB 120224A	4	4	-	-	-	0.54
(e) 10.24 ms						
GRB 111212A†	0	1	-	-	-	0.21
GRB 120211A	0	1	-	-	-	0.30
GRB 120212A	0	0	-	-	-	1.00
GRB 120218A	0	0	-	-	-	1.00
GRB 120224A	0	0	-	-	-	1.00
(e) 20.48 ms						
GRB 111212A†	0	0	-	-	-	1.00
GRB 120211A	0	0	-	-	-	1.00
GRB 120212A	0	0	-	-	-	1.00
GRB 120218A	0	0	-	-	-	1.00
GRB 120224A	0	0	-	-	-	1.00
(e) 25.6 ms						
GRB 111212A†	0	0	-	-	-	1.00
GRB 120211A	0	0	-	-	-	1.00
GRB 120212A	0	0	-	-	-	1.00
GRB 120218A	0	0	-	-	-	1.00
GRB 120224A	0	0	-	-	-	1.00

†GRB 111212A was observed over a period of 20 minutes.

Table 3.4: A summary of the statistical analysis performed on all the blank sky datasets. The subtables (a), (b), (c), (d), (e) list the time averages used in this experiment. The columns are same as for Table 3.3

GRB Name	$N_E(I > 5\sigma)$	$N_A(I > 5\sigma)$	$\sqrt{N_E(I > 5\sigma)}$	Δ_N	δE	p
(a) 640 μs						
GRB 111212A[a]	15	15	4	12	12	0.52
GRB 120211A	83	83	8	49	49	0.50
GRB 120212A[b]	83	-	-	-	-	-
GRB 120218A	83	81	8	49	49	0.52
GRB 120224A	83	90	8	49	49	0.44
(b) 1.28 ms						
GRB 111212A[a]	8	1	3	9	9	0.77
GRB 120211A	32	28	6	36	36	0.54
GRB 120212A[b]	32	-	-	-	-	-
GRB 120218A	32	35	6	36	36	0.48
GRB 120224A	32	37	6	36	36	0.44
(c) 2.56 ms						
GRB 111212A[a]	3	1	1	4	4	0.68
GRB 120211A	11	9	3	18	18	0.54
GRB 120212A[b]	11	-	-	-	-	-
GRB 120218A	11	7	3	18	18	0.58
GRB 120224A	11	9	3	18	18	0.54
(d) 5.12 ms						
GRB 111212A[a]	0	0	-	-	-	1.00
GRB 120211A	3	5	-	-	-	0.14
GRB 120212A[b]	3	-	-	-	-	-
GRB 120218A	3	2	-	-	-	0.55
GRB 120224A	3	2	-	-	-	0.55
(e) 10.24 ms						
GRB 111212A[a]	0	0	-	-	-	1.00
GRB 120211A	0	0	-	-	-	1.00
GRB 120212A[b]	0	-	-	-	-	-
GRB 120218A	0	0	-	-	-	1.00
GRB 120224A	0	0	-	-	-	1.00
(e) 20.48 ms						
GRB 111212A[a]	0	0	-	-	-	1.00
GRB 120211A	0	0	-	-	-	1.00
GRB 120212A[b]	0	-	-	-	-	-
GRB 120218A	0	0	-	-	-	1.00
GRB 120224A	0	0	-	-	-	1.00
(e) 25.6 ms						
GRB 111212A[a]	0	0	-	-	-	1.00
GRB 120211A	0	0	-	-	-	1.00
GRB 120212A[b]	0	-	-	-	-	-
GRB 120218A	0	0	-	-	-	1.00
GRB 120224A	0	0	-	-	-	1.00

[a]Blank sky was observed over a period of 5 minutes.
[b]No blank sky data were recorded due to insufficient storage space at the telescope.

Comparing the experiment parameters with B12

The average response times for our experiments and B12 are comparable. Table 3.5 compares the parameters of the B12 observations and our observations. We calculate that the one sigma flux density for our observations to detect a pulse width of 25 ms is approximately 0.5 Jy and for the B12 observations is 1.07 Jy, indicating that our observations are twice as sensitive as those by B12, (although at different frequencies). The two pulses detected by B12 are of > 5 millisecond duration. Therefore, the difference in the minimum time resolution in both experiments is not likely to be significant.

Table 3.5: Observational parameters of this work and B12

Parameters	12m Parkes	26m Hobart
Central Frequency (MHz)	1340	2276
Bandwidth (MHz)	220	64
Time Resolution (μs)	64	640
# of Channels	600	128
# of Polarisations	2	2
System Equivalent Flux Density-SEFD (Jy)	3800	900
Min detectable flux density-1σ (Jy) @ 25ms	1.07	0.5
Beam Full Width at Half Maximum (deg)	1.28	0.35
Average slew time (s)	175	140
S/N threshold	6	5

The Similarity of the GRB X-ray light curves

Figure 3.10 shows the X-ray light curves for the GRBs observed in our experiment and Figure 5 in B12 shows the X-ray light curves for the two GRBs for which radio pulses were detected by B12. The X-ray flux (F_ν, erg cm^{-2} s^{-1}) is given as $F_\nu \propto \nu^{-\beta_X} t^{-\alpha_X}$ where β_X is the spectral index, α_X is the temporal decay index, t and ν are the time and frequency respectively.

Evaluating Figure 3.10 and Figure 5 in B12, the X-ray telescope (XRT) typically starts observations $\sim 10^2$ s after the prompt γ-rays. The X-ray flux follows a typical pattern which comprises three distinct power-law segments as described by Nousek et al. (2006), Zhang et al. (2006), and O'Brien et al. (2006): (1) initial steep decay slope ($F_\nu \propto t^{-\alpha_X}$ with $3 \lesssim \alpha_{X,1} \lesssim 5$ and $t \sim 10^1 - 10^2$ s); (2) a very shallow decay ($0.5 \lesssim \alpha_{X,2} \lesssim 1.0$ and $t \sim 10^2 - 10^3$ s); and (3) a steep decay ($1.0 \lesssim \alpha_{X,3} \lesssim 1.5$ and $t \sim 10^3 - 10^4$ s). These segments are separated by two corresponding break times, $t_{break,1} \lesssim 500$ s and $10^3 \lesssim t_{break,2} \lesssim 10^4$ s.

Table 3.6 lists the temporal indices ($\alpha_{X,1}$, $\alpha_{X,2}$, $\alpha_{X,3}$) and spectral index (β_X) parameters for all the X-ray light curves in Figure 3.10 and Figure 5 in B12. The temporal indices and spectral indices for all the GRBs listed in the Table 3.6 are consistent with the standard GRB X-ray light curve, indicating that the GRBs are from similar populations (although in many cases we do not see all three power-law segments, due to limited XRT coverage). Therefore we note that the GRBs from which B12 claim FRB emission do not appear different from the GRBs we observed in our experiment.

Detection Statistics

Here we estimate the probability that the combined experiments detected FRB emission, over the combined observations reported in this experiment (hereafter, P14) and in B12. Since many astrophysical objects follow a luminosity function with power-law exponent (Macquart, 2011), we assume GRBs are distributed homogeneously in a static Euclidean Universe and each GRB generates an FRB with differential number density per unit flux given by,

$$\frac{\mathrm{dN}}{\mathrm{dS}} \propto \mathrm{S}^{-\alpha_\mathrm{r}} = \mu \mathrm{S}^{-\alpha_\mathrm{r}}. \tag{3.8}$$

where $\alpha_\mathrm{r} = 2.5$. In order to compare events at different frequencies, we assume the flux density of the FRB has a spectral index β_r over radio frequencies.

Based on these assumptions, we calculate the total probability of our experiment detecting zero events, and B12 detecting two events out of eight. The total probability, $\mathrm{P_{tot}}$, for both experiments is given by the joint probability distribution,

$$\mathrm{P_{tot}} = \prod_{\mathrm{i}=1}^{2} \mathrm{P}(\mathrm{S} > \mathrm{S_{min,B12}}) \times \prod_{\mathrm{i}=1}^{6} \mathrm{P}(\mathrm{S} < \mathrm{S_{min,B12}}) \times \prod_{\mathrm{i}=1}^{5} \mathrm{P}(\mathrm{S} < \mathrm{S_{min,P14}}), \tag{3.9}$$

where S is the flux density and $\mathrm{S_{min,B12}}$ and $\mathrm{S_{min,P14}}$ are the threshold flux densities for the B12 experiment and our experiment, respectively. $\mathrm{P}(\mathrm{S} > \mathrm{S_{min,B12}})$ corresponds to the probability of detecting events $> \mathrm{S_{min,B}}$ and is given by,

$$\mathrm{P}(\mathrm{S} > \mathrm{S_{min,B12}}) = \frac{\int_{\mathrm{S_{min,B12}}}^{\infty} \mu\ \mathrm{S}^{-\alpha_\mathrm{r}}\ \mathrm{dS}}{\int_{\mathrm{S_0}}^{\infty} \mu\ \mathrm{S}^{-\alpha_\mathrm{r}}\ \mathrm{dS}} = \left(\frac{\mathrm{S_{min,B12}}}{\mathrm{S_0}}\right)^{-\alpha_\mathrm{r}+1}, \tag{3.10}$$

where the denominator normalises the distribution for a lower limit on the FRB flux density. We chose $\mathrm{S_0} = 0.189\,\mathrm{Jy}$ to maximise $\mathrm{P_{tot}}$ for $\beta_\mathrm{r} = 0$, hence to maximize the chance that the observed FRBs by B12 are astrophysical. The

Table 3.6: Temporal indices ($\alpha_{X,1}$, $\alpha_{X,2}$, $\alpha_{X,3}$) of the X-ray lightcurves for the GRBs observed in our experiment and for two GRBs for which radio pulses were detected B12. $t_{break,1}$ and $t_{break,2}$ are the break times in second on the X-ray lightcurve. β_X is the spectral index in photon counting (PC) mode (Evans et al., 2009)

Source	$\alpha_{X,1}$	$t_{break,1}$ (s)	$\alpha_{X,2}$	$t_{break,2}$ (s)	$\alpha_{X,3}$	$\beta_X^{\dagger}$
GRB 100704A[a]	3.09 ± 0.58	502	0.38 ± 0.30	1157	0.90 ± 0.08	1.12 ± 0.10
GRB 101011A[a]	2.54 ± 0.70	708	-	-	0.89 ± 0.17	0.81 ± 0.30
GRB 111212A[b]	-	-	-	-	1.49 ± 0.12	1.03 ± 0.14
GRB 120211A	1.74 ± 0.18	521	-0.19 ± 0.25	5082	0.79 ± 0.33	0.22 ± 0.21
GRB 120212A[b]	-	-	-	-	1.01 ± 0.07	1.08 ± 0.16
GRB 120218A[c]	-	-	-	-	-	-
GRB 120224A	7.38	136	0.01 ± 0.10	5348	1.07 ± 0.26	1.22 ± 0.14

a: Two GRBs from B12 experiment for which radio pulses were detected.

b : No XRT prompt phase information was recorded due to Swift satellite orbital constrains. As the Swift satellite is in a low Earth orbit with the orbit period of 94 minutes, it suffers from 50% time off target per orbit.

c : No X-ray light curve due to Sun observing constraints. Swift could not slew to the BAT position until 19:14 UT on 20-02-12.

† : The information on spectral index β_X were obtained from the Swift XRT archive.

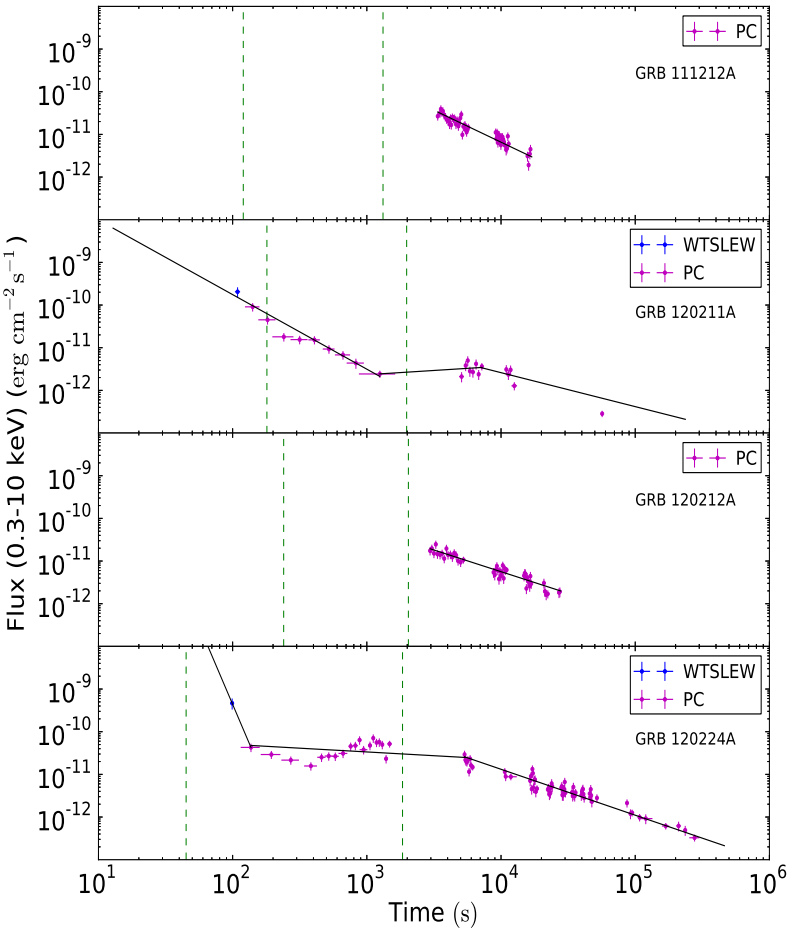

Figure 3.10: The X-ray lightcurves for the four of the five GRBs observed in our experiment. The observation start (T_{on}) and end time are marked as vertical green lines. The black lines are the XRT powerlaw fits. WTSLEW/WT-settling is the window timing mode during the spacecraft slew. PC is the photon counting mode. For GRB 120218A no XRT lightcurve due to sun observing constraints. For GRB 111212A and GRB 120218A no XRT prompt phase information was recorded due to Swift satellite orbital constrains. As the Swift satellite is in a low Earth orbit with the orbit period of 94 minutes, it suffers from 50% time off target per orbit.

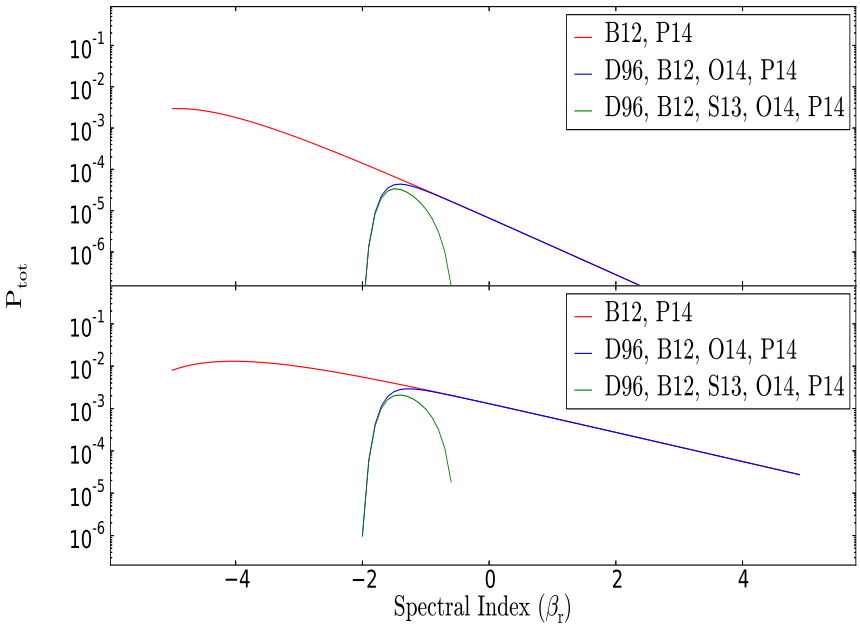

Figure 3.11: *Top panel*: The probability of detecting B12 detecting two events and zero events in other experiments as a function of β_r, spectral index. *Bottom panel*: The probability B12 detecting one real event and zero events in other experiments as a function of β_r, spectral index. S_0 is the low flux density cutoff. The three curves show the limit imposed by adding more experiments at different frequencies. The red solid line depicts the total probability for P14 and B12 experiments for the range of spectral indices. The blue solid line depicts the total probability of B12 finding events while D96, O14 and P14 experiments have found no events. The green solid line depicts the total probability of finding events while S13, D96, O14 and P14 experiments have found no events.

choice of S_0 corresponds to a low flux density cutoff in dN/dS that must exist for the probability of observing an FRB associated with any GRB to not be vanishingly small. Physically this would correspond to a correlation between observed GRB flux density and FRB flux density. Testing the existence of such a correlation is an underlying motivation for this (and similar) experiments.

We note that the observing frequency and S/N threshold are different between our experiment and the B12 experiment (Table 3.5). The intrinsic spectral index is unknown. This difference is accounted for by scaling the flux density with a range of spectral indices $-5 \leq \beta_r \leq +5$, given by,

$$S_{\rm min,B12} = 6\,\sigma_{\rm B12} \left(\frac{\nu_{\rm P14}}{\nu_{\rm B12}}\right)^{\beta_{\rm r}}, \tag{3.11}$$

where $\sigma_{\rm B12}$ is the minimum detectable flux density at 25 ms in B12 (Table 3.5), $\nu_{\rm P14}$ and $\nu_{\rm B12}$ are the central frequencies in our experiment and B12, respectively.

Next, we estimate $P_{\rm tot}$ in two regimes (1) the probability of detecting zero events in our experiment, and B12 detecting two events (from eight); (2) the probability of detecting zero events in our experiment, and B12 detecting one event (from eight). In the second case we calculate the probability using the equation 3.10 just by changing the upper limit on first two terms of equation 3.10. In the former case, the probability < 0.001 (top panel of Figure 3.11, solid red line) and in the latter case the probability $P_{\rm tot} \lesssim 0.01$ (bottom panel of Figure 3.11, solid red line). This indicates that non-detections in our experiment are highly unlikely to be consistent with B12 having obtained two detections.

Next, we now extend the above analysis to include the experiments of Dessenne et al. (1996, hereafter D96), Staley et al. (2013, hereafter S13) and Obenberger et al. (2014, hereafter O14). Table 3.7 list the parameters for these experiments. The total probability of observed results over all five experiments, is given by,

$$\begin{aligned} P_{\rm tot} = &\prod_{\rm i=1}^{2} P(S > S_{\rm min,B12}) \times \prod_{\rm i=1}^{6} P(S < S_{\rm min,B12}) \times \prod_{\rm i=1}^{5} P(S < S_{\rm min,P14}) \\ &\times \prod_{i=1}^{2} P(S < S_{\rm min,D96}) \times \prod_{\rm i=1}^{34} P(S < S_{\rm min,O14}) \times \prod_{\rm i=1}^{4} P(S < S_{\rm min,S13}). \end{aligned} \tag{3.12}$$

Similar to the above analysis, we calculate the total probability in two regimes: (1) the probability of detecting zero events in four different experiments, and B12 detecting two events (from eight); (2) the probability of detecting zero events in four different experiments, and B12 detecting one event (from eight).

To illustrate the effects of adding the low frequency experiments and the high frequency experiments, we combine the experiments in two steps. First, low frequency experiments D96 and O14 are combined with B12 and P14 experiments. Next, both high and low frequency experiments S13, D96 and O14 are combined with B12 and P14 experiments. The blue solid line in the Figure 3.11 depicts the total probability of B12 finding events while D96, O14 and P14 experiments have found no events. The green solid line in the Figure 3.11 depicts the total probability of B12 finding events while S13, D96, O14 and P14 experiment found no events. In both cases the probability of null detection in S13, D96, O14 and P14 experiments, while B12 detecting at least one, is $< 10^{-2}$.

The sensitivities of the S13, D96, O14 experiments are scaled to detect a 25 ms pulse (Table 3.7). In the Figure 3.11, we note a sharp cut-off in the curve, because at this point the low frequency and high frequency experiments have S_{min} values less than S_0, which implies that the probability of detecting an event would be vanishingly small. Hence, the low frequency experiments (D96 and O14) would have easily detected a 25 ms pulse with spectral index $\beta_r < -2$ given their detection thresholds, and the high frequency experiment S13 would have easily detected a 25 ms pulse with the spectral index $\beta_r > -0.5$.

Finally, we to note that including the other previous low frequency experiments, of Baird et al. (1975), Benz and Paesold (1998) and Balsano (1999) in the analysis makes no difference to the results.

3.5 Summary

This experiment searched for FRB-like emission from GRBs at 2.3 GHz. We observed five GRBs using a 26-m radio telescope, automated to quickly respond to GCN notifications and slew to the source position within minutes. We did not detect any sigma events $> 6\sigma$ similar to B12, which motivated this experiment. Our analysis of events detected at $> 5\sigma$ in our experiment shows that they are consistent with thermal noise fluctuations. Non-detections in our experiment agree with the lack of consistency between the event rates presented in Thornton et al. (2013) and GRB event rates.

A joint analysis of our results and four other GRB experiments shows that the B12 results are highly unlikely to be astrophysical. If B12 events are real then the combined analysis constrains the radio spectral index of the events to be $-2 \lesssim \beta \lesssim -0.5$.

Table 3.7: Observation parameters of other GRB experiements.

Parameters	D96	S13†	O14⋆
Central Frequency (MHz)	151	15270	74, 52, 37.9
Bandwidth	700 kHz	6 GHz	75 kHz
Time Resolution (s)	1.5	0.5	5
Min detectable flux density-1σ (Jy) @ 25ms	20	0.026	353, 336, 311
# of GRBs observed	2	4	12, 5, 17
S/N threshold	3	3	5

† The total number of GRBs observed by S13 was 11, out of which only 4 GRBs were observed within 5 min of the GRB notification. Hence we consider only four GRBs in the analysis.

⋆ O14 observed 34 GRBs in total. However the sensitivity of the detector was different for each GRB. Here we have calculated the sensitivity by taking an average over the sensitivities at a given observing frequency.

Chapter 4

A Search for Fast Radio Bursts in the Central Parsec of our Galaxy at 22 GHz

We shall not cease from exploration, and the end of all our exploring will be to arrive where we started and know the place for the first time.
- T. S. Eliot

4.1 Introduction

The centre of our Galaxy is by far the closest galactic nucleus and is a reasonable region to search for FRBs. Detecting FRBs from the central parsec of the Galaxy (the Galactic Centre - GC) would provide an excellent opportunity to probe the nature of the interstellar medium (ISM) in its vicinity. The GC, at a distance of ~ 8.3 kpc (Genzel et al., 2010), offers a unique view of the complex population of galactic nuclei. The central parsec is one of the most active massive star formation regions in the Galaxy and is believed to contain about 200 massive young stars (Genzel et al., 2010; Wharton et al., 2012). These massive stars are believed to be progenitors of neutron stars (NS), where the star undergoes a supernova explosion and leaves behind a NS. Theoretical estimates have suggested that a large population of compact objects in extreme matter states like NS should be orbiting the GC with periods ≤ 100 years (Pfahl and Loeb, 2004; Wharton et al., 2012; Chennamangalam and Lorimer, 2014). Scattering due to the ionised gas within 100 pc of the GC would cause temporal smearing of FRB signals, with a strong dependence on the observing frequency, $\nu_{\rm GHz}^{-4}$, hindering searches at lower

frequencies. For example, at a common pulsar observing frequency, $\nu = 1.4\,\mathrm{GHz}$, the temporal smearing $\tau_{\mathrm{ism}} = 0.116\,\mathrm{s}\left(\frac{\mathrm{D_{scat}}}{100\mathrm{pc}}\right)^{-1}\left(\frac{\nu}{10\mathrm{GHz}}\right)^{-4} \sim 227\,\mathrm{s}$ (Macquart et al., 2010), where $\mathrm{D_{scat}}$ is the distance to the thin scattering screen from the GC (here we assume $\mathrm{D_{scat}} = 133^{+200}_{-81}$ pc obtained from (Lazio and Cordes, 1998)). To overcome scattering effects, higher frequencies are considered more favourable for FRB searches at the GC. However, despite previous studies at higher frequencies (eg. Macquart et al. (2010) at 14.4 GHz, Eatough et al. (2013) at 18 GHz), the lack of FRB detections indicates that scattering towards the inner parsec could be worse than predicted, which calls for observations at even higher frequencies ($> 18\,\mathrm{GHz}$). However, recent work by Spitler et al. (2014) and Bower et al. (2014) on the pulse broadening and the angular scatter broadening of the magnetar PSR J1745-29[1] have shown that the scattering may not be a limitation as previously thought (at least for some lines of sight).

In this work, our primary objective is to search for FRB-like emission from the central parsec of our Galaxy at high time resolution ($64\,\mu\mathrm{s}$) at 22 GHz. To our knowledge this is the first high time resolution experiment searching for FRB-like emission at 22 GHz towards the GC. In section 4.2 we describe the observation details. Section 4.3 gives the description of the single pulse pipeline. In section 4.4 we discuss the results and analysis. Sections 4.5 and 4.6 contain the discussion and conclusions, respectively.

4.2 Observations

We performed a six-hour observation towards Sgr A* (centred on: $\alpha = 17^h\ 45^m\ 40.0332^s$; $\delta = -29^\circ\,00'\,28.069''$) at 22.235 GHz using the 26 m radio telescope located at the Mount Pleasant Radio Observatory operated by University of Tasmania[2] near Hobart, Tasmania.

Data were recorded using the Australian Long Baseline Array (LBA) Data Acquisition System (DAS)[3] (Phillips et al., 2009). The LBA DAS has a sampler and digital filter which receives two independent analog intermediate frequencies (IFs), the right and left circular polarised signals over a 64 MHz bandwidth. The analog IFs are sampled and digitised to 8 bit precision and then re-sampled to 2 bits using digital filters before the digital representation of the voltage is

[1]The only NS discovered in the inner parsec, with the projected distance of 0.12 pc ($3''$) from the GC (Eatough et al., 2013).

[2]www.utas.edu.au/maths-physics/facilities/mt-pleasant-observatory

[3]www.atnf.csiro.au/technology/electronics/docs/lba_das/lba_das.html

recorded to computer disk. The system temperature (T_{sys}) was measured by firing the noise diode every 30 minutes, and ranged between 207 K to 230 K over the entire observing period. Thereby, using T_{sys}, the system equivalent flux density (SEFD) of the telescope was estimated to be 1800-2000 Jy, which is calculated as SEFD $= \frac{8\,k_B\,T_{sys}}{\eta_a\,\pi\,D^2}$, where k_B is the Boltzmann constant, η_a and D are the antenna efficiency (0.6) and the diameter of a circular aperture antenna (26 m), respectively. The automatic gain control loops were turned off for the duration of the observation. The pointing error of the 26 m telescope across the whole sky is $\backsim 21''$. This error is frequently calibrated using a pointing model which calculates a grid-based set of offsets for a strong (> 1 Jy) continuum source with the 8 GHz receivers. Table 4.1 gives a detailed summary of the observational parameters.

Table 4.1: Observation Parameters Summary.

Observing Time (Hr)	6
Centre Frequency (MHz)	22235
Polarisations	2
Bandwidth (MHz)	64
Frequency channels	128
SEFD (Jy)	1800-2000
Integration time (μs)	64
Full width half maximum (FWHM) ($''$)	100
Spatial radius† (pc)	~ 2

†Distance to the GC - 8.3 ± 0.3 kpc (Genzel et al., 2010).

Experiment Sensitivity

The one sigma flux density in a single pulse search, where the effective observing time is equal to the pulse width, is approximately 20 - 22 Jy, calculated as

$$\sigma = \frac{\mathrm{SEFD}}{\sqrt{\triangle\nu_{\mathrm{MHz}} \times \mathrm{W} \times \mathrm{n_{pol}}}} \simeq 20 - 22\ \mathrm{Jy}, \tag{4.1}$$

where SEFD is $1800 - 2000$ Jy, $\triangle\nu_{\mathrm{MHz}}$ and W are the bandwidth (64 MHz) and integration time (64 μs), and n_p is the number of polarisations (2).

4.3 Data Processing

The recorded data ($\sim$ 11 TB) were transferred to the petabyte data storage facility at iVEC[4], in Perth. Data processing was performed on the Curtin University Parallel Processor for Astronomy (CUPPA), a 20 node computer cluster operated by Curtin University. Our primary aim was to search for single pulses at high time resolution ($64\,\mu s$).

Single Pulse Search at High Time Resolution

The data processing was carried out along similar lines to that described in chapter 3. The data processing steps are broadly divided as follows: generating the filterbank data; generating time averages for wide range of pulse widths; radio frequency interference (RFI) identification and excision; dedispersion; event detection; and classification of detected events.

In this experiment, the voltage data were processed to generate filterbank data streams with a time resolution of $64\,\mu$s and 128 spectral channels across the 64 MHz bandwidth. To obtain reasonable sensitivity, the correlated time series were averaged for pulse widths in the range $64\,\mu\text{s} - 4\,\text{ms}$. This is achieved by averaging 2^{n} time samples together, where n ranges from $0 - 6$. The averaged time series are passed through the rest of the data processing pipeline independently.

At 22 GHz, data are rarely affected by RFI. RFI changes the total power as a function of frequency and time. Here we performed the RFI identification and excision on the filterbank data. The RFI excision algorithm searches for wide band, narrow band, and persistent RFI in the time and frequency plane and excises them.

The data were dedispersed with DM steps ranging from 0-10000 pc cm^{-3}. Table 4.2 lists the number of DM steps used to dedisperse the averaged time series. At 22 GHz, the relative dispersion delay across the 64 MHz band is $\sim$ $48\,\mu$s for every 1000 pc cm^{-3}, therefore DM sampling finer than 1000 pc cm^{-3} was not required.

The dedispersed time series were searched for the single-pulse events above the predefined signal to noise (S/N) threshold (6σ)[5]. The time series in each

[4]www.ivec.org/about/

[5]A 6σ threshold was chosen because we wanted to have a higher confidence level. The probability of find a false positive event at 6σ is 9.9×10^{-10} and the probability at 5σ is 2.7×10^{-7}. For example if we have $\sim 2 \times 10^{10}$ independent samples, therefore, at 5σ we would be effectively detecting $\sim$ 5400 sample as a false positive, compared to when a 6σ threshold is

DM step were divided into short time segments ($\sim$ 0.5s) and then searched for events $> 6\sigma$. The noise level for each DM step is estimated using the standard deviation. All the events $> 6\sigma$ from our detection pipeline were visually examined for signatures of astronomical signals. All the events $> 6\sigma$, including the events at DM of 0 pc cm^{-3}, are re-processed with fine time resolution (next stage in the pipeline) so that we gain further DM resolution to differentiate terrestrial and astronomical signals.

In the follow-up process, a small time segment ($\sim$ 1 s) of baseband and filterbank data was saved for each event. Here, first the signal is confirmed by visually inspecting the dedispersed data and then its DM is refined by reprocessing the data with fine time resolution ranging from $8 - 32\,\mu s$. The events that are not broader than the initial time averaging will have the S/N improved by reprocessing with fine time resolution. On the contrary, the signal would be degraded if the events are broader than the initial time averaging. At fine time resolution (8 μs) the dispersion across the 64 MHz band for the DM of 1000 pc cm^{-3} is 48 μs, which implies an astronomical signal would be dispersed across $\sim$ 6 time samples at 8 μs, which should give a reasonable diagnostic to differentiate between a astronomical signal and RFI.

4.4 Results and Analysis

4.4.1 Results from Single Pulse Search Pipeline

Processing the six hours of data, we detected three events $> 6\sigma$. Table 4.3 lists these events. Two high significance pulses imply that they are likely to arise either from a compact source at the GC or RFI from some terrestrial source because the probability of events due to thermal noise fluctuations at 9.2σ and 8.3σ are 10^{-11} and 10^{-7}, respectively. The SNRs of the events peak at the DM of 0 pc cm^{-3}. Since the dispersion at 22 GHz is very small, we do not immediately discard the event at a DM of 0 pc cm^{-3} as RFI. In the next section we perform a statistical analysis on the events detected $> 6\sigma$ to check if they are consistent with expectations due to thermal noise fluctuations.

chosen we would be effectively detecting 0$\pm$1 sample as a false positive.

Table 4.2: For each time average, the table lists the number of DM steps and DM's used to dedisperse the data. The lower panel of the table lists the numbers of DM steps and DM's used in the event follow-up stage.

Time Averages (μs)	N_{DM}	DM steps
64	8	0.00,1331.76,2663.51,3995.27,5327.02,6658.78,7990.53,9322.29
128	4	0.00,2663.51,5327.02,7990.53
256	2	0.00,5327.02
512	1	0.00
1024	1	0.00
2048	1	0.00
4096	1	0.00

Event Follow-up

Time Averages (μs)	N_{DM}	DM steps
8	60	0.00,166.47,332.94,499.41,665.88,832.35,998.82,1165.29, 1331.76,1498.22,1664.69,1831.16,1997.63,2164.10,2330.57,2497.04,2663.51, 2829.98,2996.45,3162.92,3329.39,3495.86,3662.33,3828.80,3995.27,4161.74, 4328.21,4494.67,4661.14,4827.61,4994.08,5160.55,5327.02,5493.49,5659.96, 5826.43,5992.90,6159.37,6325.84,6492.31,6658.77,6825.24,6991.71,7158.18, 7324.65,7491.12,7657.59,7824.06,7990.53,8157.00,8323.47,8489.94,8659.74, 8832.93,9009.59,9189.78,9373.58,9561.05,9752.27,9947.31
16	31	0.00,332.94,665.88,998.82,1331.76,1664.69,1997.63,2330.57, 2663.51,2996.45,3329.39,3662.33,3995.27,4328.20,4661.14,4994.08,5327.02, 5659.96,5992.90,6325.84,6658.78,6991.72,7324.65,7657.59,7990.53,8323.47, 8656.41,8989.35,9322.29,9655.23,9988.16
32	16	0.00,665.88,1331.76,1997.63,2663.51,3329.39,3995.27,4661.14, 5327.02,5992.90,6658.78,7324.65,7990.53,8656.41,9322.29,9988.16

Table 4.3: Events $> 6\sigma$ detected from the single pulse search pipeline.

Events	Time Average (μs)	S/N (σ)	DM (pc cm^{-3})
GC-E1	64	6.3	1331 ± 1332
GC-E2	128	9.2	0 ± 2664
GC-E3	256	8.3	0 ± 5328

Events due to random noise fluctuations

Here we determine the number of events expected $> 6\sigma$ due to thermal noise fluctuations in the data. A detailed description of the statistical methods is given in section 3.4. Here we construct a simple model to estimate the probability of events $> 6\sigma$ due to thermal noise fluctuations, assuming the fluctuations follows a Gaussian distribution and the DM trials used are independent. The probability is given by

$$\mathrm{N_E(I > 6\sigma) = N_t\ N_{DM}\ erfc}\left(\frac{6}{\sigma\sqrt{2}}\right), \tag{4.2}$$

where $\mathrm{N_{DM}}$ is the number of independent DMs, $\mathrm{N_t}$ is the number of independent time samples, and erfc is the complementary error function. Table 4.4 lists the number of events expected $> 6\sigma$ for the time averages ranging from $64\mu\mathrm{s} - 4\mathrm{ms}$, respectively.

Table 4.4: Summary of the statistical analysis performed on the events detected above $> 6\sigma$, assuming the data follow a Gaussian distribution. The columns are: the list of time averages used in this experiments, $\mathrm{N_E(I > 6\sigma)}$ is the expected number of events above the S/N threshold due to thermal noise fluctuations, $\mathrm{N_A(I > 6\sigma)}$ is the actual number of events detected above the S/N threshold.

Time Averages (μs)	$\mathrm{N_E(I > 6\sigma)}$	$\mathrm{N_A(I > 6\sigma)}$
64	3	1
128	1	1
256	1	1
512	0	0
1024	0	0
2048	0	0
4096	0	0

Analysis of GC-E1

GC-E1 was initially detected at 64 μs time resolution, at a significance of 6.3σ. A 64 μs wide single pulse was detected 278.28 minutes from the start of the observation at a DM of 1331 pc cm^{-3}. No events were detected in the consecutive DM steps and in the other time averages (128s – 4ms). In the event follow-up process, the baseband data were re-correlated with finer time resolution (8 - 32 μs) and dedispersed with fine DM resolution (Table 4.2). Figure 4.1 shows the event as originally detected at 64 μs time sampling. No single pulses were detected in the other fine time averages. Statistical analysis shows that the single event detected $> 6\sigma$ is consistent with the number of events expected $> 6\sigma$ due to thermal noise fluctuations (Table 4.4). Hence we conclude that GC-E1 is consistent with thermal noise fluctuations.

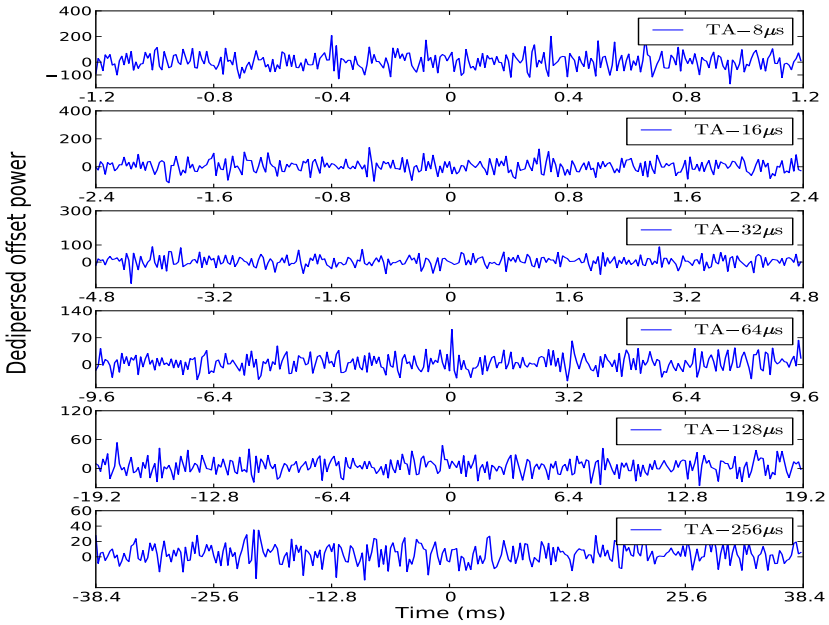

Figure 4.1: GC-E1 detected at 64 μs with a peak S/N ratio at DM of 1324 pc cm^{-3}. No pulses were detected at other time averages between 8 - 256 μs.

Analysis of GC-E2 and GC-E3

GC-E2 was detected at 128 μs time resolution, at a significance of 9.2σ and GC-E3 was detected at 256 μs time resolution, at a significance of 8.5σ, at 12 minutes

and 171.6 minutes, respectively, from the start of the observation at the zeroth DM bin. Both events were detected in several consecutive DM steps and in all time averages with reduced S/N. In the event follow-up process, the baseband data for both events were re-correlated with finer time resolutions, over 8 - 32 μs and dedispersed with finer DM resolution (Table 4.2). Pulses were detected in all the fine time averages (8 - 32 μs) with the peak S/N at DM of 0 pc cm^{-3}.

Figures 4.2a and 4.2b shows the single pulses detected in the time averages over $8 - 256\,\mu$s at the zeroth DM bin. Visual inspection of both events (Figures 4.2a and 4.2b) at the finest time resolution (8 μs) and DM resolution did not show any signatures of astronomical signals. If the signals were from an astronomical source, the S/N of the signal should peak at higher DM steps. Since for both events the S/N peak at DM of 0 pc cm^{-3}, we conclude the events are highly likely to be terrestrial signals. Hence there is no evidence that we have detected any short duration bursts of radio emission from the GC.

4.5 Discussion

4.5.1 Scattering at 22 GHz towards GC

Pulse broadening from multipath propagation through the ISM could have limited the number of events detected in this experiment, since broadening is dependent on the thin scattering screen distance D_{scat}. That is, if the screen is closer to the GC, τ_{ism} increases.

If we assume D_{scat} to be 133^{+200}_{-80} pc, a best estimate of the thin screen scattering distance given by Lazio and Cordes (1998), $\tau_{ism} = 3.56$ ms, which implies that pulses of $\sim$ ms durations are strongly affected due to scattering. On the contrary, assuming the scattering in the direction of the GC magnetar is representative of the entire inner parsec, $D_{scat} = 5\,$kpc (Bower et al., 2014)[6], $\tau_{ism} = 94\mu$s, which is close to our first pass integration time (64μs).

[6]Recent work by Roy (2013) suggests that the scattering medium is asymmetrically distributed. They derived scattering screen diameter towards the GC to be $30'' \pm 2''.3$ which is in contrary to the previously suggested scattering screen diameter ($100''$) by Lazio and Cordes (1998). They suggest that the assumption of single uniform screen for GC toward line of sight is not sufficient to understand the effects of scattering on the detectability.

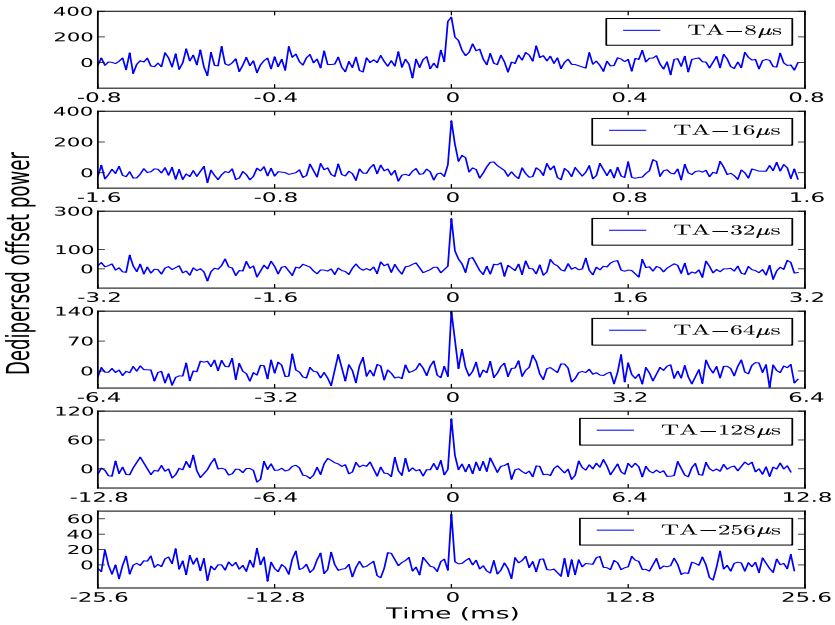

(a) GC-E2

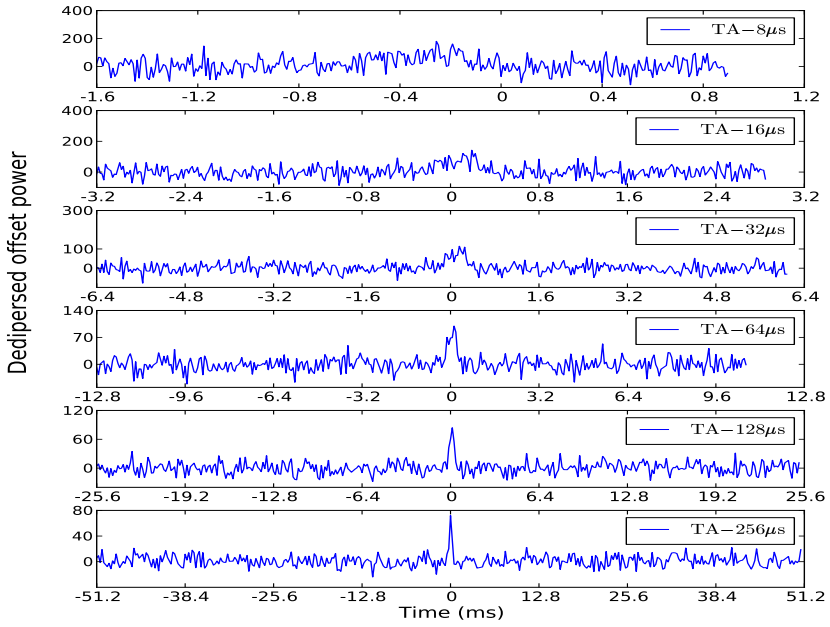

(b) GC-E3

Figure 4.2: Single pulses detected in the time averages ranging 8 - 256 μs, with S/N ratio peak at DM of 0 pc cm^{-3}.

4.5.2 FRB Event Rate

One can compute the number of events per unit time per unit volume, given an observation, a geometry and a scattering regime. This calculation is direction dependent and the volume at the Galactic Centre is a complicated function that depends on the geometry of the Galaxy. The loss in sensitivity due to scattering must also be incorporated in the event rate calculation. This calculation is more complicated compared to the event rate models proposed for extra-galactic FRBs (Deneva et al., 2009; Macquart, 2011; Trott et al., 2013) for the reasons discussed above and beyond the scope of this thesis. Hence this work will be pursued in future.

4.6 Summary

This experiment searched for FRB-like emission from the central parsec of the Galaxy at 22 GHz. We performed a six-hour survey using the 26 m Hobart radio telescope. Data were searched for pulses up to a dispersion measure of 10000 $\mathrm{pc\,cm^{-3}}$ and pulse widths ranging from $64\mu\mathrm{s} - 4\mathrm{ms}$ covering a reasonable search volume for FRBs. We detected three events above our 6σ detection threshold. An analysis of the events indicates no convincing evidence that that events are astrophysical.

In the future we propose to continue observations of Sgr A*. Future experiments should aim to utilise full frequency coverage available at high frequencies. An increased bandwidth would not only provide an improvement in sensitivity, but also better rejection of RFI using the dispersive sweep signature of signal from astronomical sources.

Chapter 5

Conclusions and Scope for Future Work

Space, the final frontier...
- From a popular television series.

In this chapter we summarise the contributions and findings presented in this thesis. In the following section we explore the possible direction this research can be steered towards in the future to improve on the current techniques and observations.

5.1 Conclusions

The recent discoveries of FRBs from the Parkes and Arecibo radio telescopes have provided excellent evidence that FRBs are astronomical in origin and the science return from detecting many more and localising even a small number would be extremely high.

The objective of the present work was to search for FRBs from our Galaxy and extragalactic objects. The first part of this thesis focuses on the search for FRBs possibly associated with gamma-ray bursts (GRBs). The second part focuses on the search for FRBs from the central parsec of our Galaxy.

In Chapter 3 we presented an experiment searching for FRB-like emission from GRBs at 2.3 GHz. We observed five GRBs using a 26-m radio telescope, automated to quickly respond to GCN notifications and slew to the source position within minutes. The data were searched for pulses up to 5000 pc cm^{-3} in dispersion measure and pulse widths ranging from 640 μs to 25.60 ms. We did not

detect any events $> 6\sigma$ similar to Bannister et al. (2012), which motivated this experiment. Non-detections in our experiment agree with the lack of consistency between the event rates presented in Thornton et al. (2013) and GRB event rates. An in-depth statistical analysis of our data shows that events detected above 5σ are consistent with expectations from thermal noise fluctuations. We demonstrate how time domain data from these surveys can be properly interpreted in the presence of stochastic and systematic uncertainties introduced by the instrument themselves and other non-astronomical radio sources (human-made Radio Frequency Interference, RFI, for example). This analysis has provided valuable lessons for similar observations in FRB search surveys in general in the future. This study also highlighted the potential of observing blank patches of the sky $\sim 2^\circ$ away from the GRB positions. And finally we have shown using a joint analysis of our results and four GRB experiments shows that the Bannister et al. (2012) results are highly unlikely to be astrophysical. If Bannister et al. (2012) events are real then the combined analysis constrains the radio spectral index of the events to be $-2 \lesssim \beta \lesssim -0.5$.

In Chapter 4 we presented an experiment searching for FRB-like emission from the central parsec of the our Galaxy at 22 GHz. We performed a six-hour survey using the 26-m Hobart radio telescope. To our knowledge this is the first high time resolution experiment searching for FRB-like emission at 22 GHz towards the GC. Six hours of data were searched for pulses up to a dispersion measure of 10000 $\mathrm{pc\,cm^{-3}}$ and pulse widths ranging from 64μs to 4ms covering a substantial search volume for FRBs. We detected three events above our 6σ detection threshold above X Jy where X is width dependent. An analysis of the events indicates no convincing evidence that the events are astrophysical.

5.2 Scope for Future Work

Several improvements can be made in the observation and analysis of the data. The scope for the future is to continue with the observations of GRBs and increase the observing time on the source from 30 minutes to ~ 2 hours. More observations with better sensitivity, rapid response to the GCN alerts, and wide field-of-view would help put a better observational constraint on the association of FRBs with GRBs. A complete automation of the data aggregation and processing would be a remarkable and profitable improvement that could result in detecting events in almost real time. We also propose to use a second telescope. The use of a second,

geographically isolated antenna could provide an additional RFI rejection system and a coincidence detection with multiple dishes would increase confidence in the detected events and localise the burst.

The scope for the future for the work presented in chapter 4 is to carry out regular monitoring of the central region of the Galactic Centre (GC) for FRBs. The GC is expected to host a large neutron star (NS) population, with many of these NSs expected to be active radio pulsars. The experiments should aim to utilise full frequency coverage available at high frequencies. An increased bandwidth at high frequency would not only provide an improvement in sensitivity, but also better rejection of RFI.

Appendix A

Independent DM Steps

In this section we show that the DM steps used to dedisperse the data in Chapter 3 and 4 are independent for our choice step progression of DM steps.

Data incoming into the dedisperser are discrete samples in frequency and time. The de-dispersion process sums the power samples across spectral channels, with the delay for each channel computed according to the frequency and DM (Figure A.1). Under normal circumstances the power level in each spectral channel follows a Gaussian distribution.

For low DMs, there is a $\sim$50% overlap between the power samples that contribute to consecutive DM trials, at the same time. Here we demonstrate that this overlap does not correspond to a high level of correlation in detections between neighbouring DM steps for a large (e.g 5σ) detection threshold, and therefore that each DM step can be considered independent.

Let us consider a DM trial where the power samples in the channels are normally distributed across the spectrum. The variance of summing $N_{\rm chan}$ independent samples equals $N_{\rm chan}\,\sigma_i^2$ and the standard deviation, $\sigma{=}\sqrt{\rm N_{chan}}\,\sigma_{\rm i}$, where σ_i is the noise level in a given power sample.

The probability of obtaining an event above a threshold, X, due to random addition of power sample fluctuations is given by the CDF;

$$\mathrm{P(I > X}\sigma) = \frac{1}{2} \, - \, \frac{1}{2}\,\mathrm{erf}\left[\frac{\mathrm{X}\,\sigma}{\sqrt{2}\,\sigma}\right], \tag{A.1}$$

Substituting $\sigma = \sqrt{\rm N_{chan}}\,\sigma_{\rm i}$ in Equation A.1, gives the CDF in terms of the noise level in each power sample;

$$\mathrm{P(I > X}\sigma) = \frac{1}{2} \, - \, \frac{1}{2}\,\mathrm{erf}\left[\frac{\mathrm{X}\,\sqrt{\rm N_{chan}}\,\sigma_{\rm i}}{\sqrt{2}\,\sqrt{\rm N_{chan}}\,\sigma_{\rm i}}\right]. \tag{A.2}$$

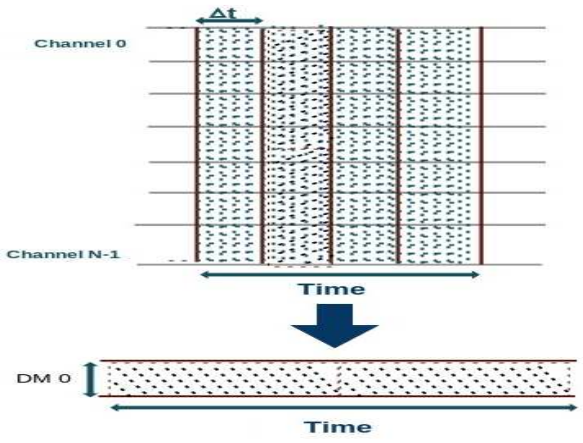

Figure A.1: Top panel: Data incoming into the dedisperser are ordered in frequency and time. The de-dispersion process sums the power samples across spectral channels, with the delay for each channel computed according to the frequency and DM. For DM=0, no delay is applied to the spectral channels and all the power samples are summed to form a time series (Bottom panel).

The probability that we obtain a detection above our experimental threshold (5σ) from an independent DM step is given by,

$$[\mathrm{P}(\mathrm{I} > 5\sigma)] = \frac{1}{2} - \frac{1}{2}\,\mathrm{erf}\left[\frac{5\sqrt{128}\,\sigma_\mathrm{i}}{\sqrt{2}\sqrt{128}\,\sigma_\mathrm{i}}\right] = 2.87 \times 10^{-7}. \tag{A.3}$$

where $N_{\mathrm{chan}} = 128$.

For low DMs, we note that due to our choice of progression in the DM steps, there is a $\sim$50% overlap between the power samples that contribute to consecutive DM trials, at the same time. When there are shared samples between consecutive DM steps, those samples contribute the same power to both DM trials. There are many permutations for how power can be distributed in each set of power samples to combine to yield two detections above Xσ. It can be shown that the power distribution with the highest joint probability over the two DM trials corresponds to the case shown in Figure A.2, where the shared power samples contribute proportionally to the power required to meet the threshold. Under this scenario, *each* of the three sets of $\mathrm{N_{overlap}} = 64$ samples contributes 2.5σ $=2.5\sqrt{\mathrm{N_{chan}}}\sigma_\mathrm{i}$. The probability that each set obtains a detection $> 2.5\sigma$ is given by,

$$\mathrm{P_{set}}(\mathrm{I} > \mathrm{X_{set}}\sigma) = \frac{1}{2} - \frac{1}{2}\,\mathrm{erf}\left[\frac{\mathrm{X_{set}}\sqrt{\mathrm{N_{chan}}}\,\sigma}{\sqrt{2\,\mathrm{N_{overlap}}}\,\sigma}\right], \tag{A.4}$$

with $X_{\rm set} = X N_{\rm overlap}/N_{\rm chan} = 2.5$, giving,

$$\mathrm{P(I > X\sigma)} = \frac{1}{2} - \frac{1}{2}\,\mathrm{erf}\left[\frac{\mathrm{X}\sqrt{\mathrm{N_{overlap}}}}{\sqrt{2\,\mathrm{N_{chan}}}}\right]. \tag{A.5}$$

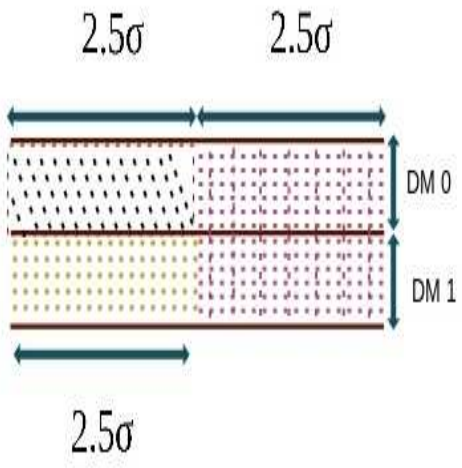

Figure A.2: Figure illustrates that $\sim 50\%$ of power samples at DM of 1 overlaps with DM of 0 represented in dotted pink lines. And rest are the non-overlapping samples in the DM of 0 and 1 repersented in dotted black and yellow lines.

When 50% of samples overlap and the threshold, X = 5, the joint probability of obtaining detections in two consecutive DM trials is given by the product of the probability for each of the three sets;

$$\mathrm{P(I > 5\sigma)} = \left[\mathrm{P_{set}(I > 2.5\sigma\,;\, N_{overlap} = 64)}\right]^3 = 1.7 \times 10^{-9}. \tag{A.6}$$

This is $\sim$100 times smaller than the probability of detecting a single event (Equations A.1-A.3). Therefore, although the power samples contributing to the consecutive DM trials are 50% correlated, due to the improbability of obtaining a single 5σ detection, the joint probability of obtaining two detections is very small. We therefore conclude that the DM trials can be considered statistically independent.

Bibliography

Atwood, W. B., A. A. Abdo, M. Ackermann, W. Althouse, B. Anderson, M. Axelsson, L. Baldini, J. Ballet, D. L. Band, G. Barbiellini, and et al. (2009, June). The Large Area Telescope on the Fermi Gamma-Ray Space Telescope Mission. *The Astrophysical Journal 697*, 1071–1102.

Baird, G. A., T. J. Delaney, B. G. Lawless, D. J. Griffiths, J. R. Shakeshaft, R. W. P. Drever, W. P. S. Meikle, J. V. Jelley, W. N. Charman, and R. E. Spencer (1975, February). A search for VHF radio pulses in coincidence with celestial gamma-ray bursts. *The Astrophysical Journal letter 196*, L11–L13.

Balsano, R. J. (1999). *A search for radio emission coincident with gamma-ray bursts*. Ph. D. thesis, PRINCETON UNIVERSITY.

Bannister, K. W. and G. J. Madsen (2014a, May). A Galactic origin for the fast radio burst FRB010621. *Monthly Notices of the RAS 440*, 353–358.

Bannister, K. W. and G. J. Madsen (2014b, May). A Galactic origin for the fast radio burst FRB010621. *Monthly Notices of the RAS 440*, 353–358.

Bannister, K. W., T. Murphy, B. M. Gaensler, and J. E. Reynolds (2012, September). Limits on Prompt, Dispersed Radio Pulses from Gamma-Ray Bursts. *The Astrophysical Journal 757*, 38.

Barnbaum, C. and R. F. Bradley (1998, November). A New Approach to Interference Excision in Radio Astronomy: Real-Time Adaptive Cancellation. *Astronomical Journal 116*, 2598–2614.

Bartos, I., P. Brady, and S. Márka (2013, June). How gravitational-wave observations can shape the gamma-ray burst paradigm. *Classical and Quantum Gravity 30*(12), 123001.

Bell, M. E., T. Murphy, D. L. Kaplan, P. Hancock, B. M. Gaensler, J. Banyer, K. Bannister, C. Trott, N. Hurley-Walker, R. B. Wayth, J.-P. Macquart, W. Arcus, D. Barnes, G. Bernardi, J. D. Bowman, F. Briggs, J. D. Bunton, R. J. Cappallo, B. E. Corey, A. Deshpande, L. deSouza, D. Emrich, R. Goeke, L. J. Greenhill, B. J. Hazelton, D. Herne, J. N. Hewitt, M. Johnston-Hollitt, J. C. Kasper, B. B. Kincaid, R. Koenig, E. Kratzenberg, C. J. Lonsdale, M. J. Lynch, S. R. McWhirter, D. A. Mitchell, M. F. Morales, E. Morgan, D. Oberoi, S. M. Ord, J. Pathikulangara, T. Prabu, R. A. Remillard, A. E. E. Rogers, A. Roshi, J. E. Salah, R. J. Sault, N. Udaya Shankar, K. S. Srivani, J. Stevens, R. Subrahmanyan, S. J. Tingay, M. Waterson, R. L. Webster, A. R. Whitney, A. Williams, C. L. Williams, and J. S. B. Wyithe (2014, February). A survey for transients and variables with the Murchison Widefield Array 32-tile prototype at 154 MHz. *Monthly Notices of the RAS 438*, 352–367.

Benz, A. O. and G. Paesold (1998, January). A search for prompt radio emission of gamma-ray bursts. *Astronomy and Astrophysics 329*, 61–67.

Bhat, N. D. R. (2011, September). Searches for radio transients. *Bulletin of the Astronomical Society of India 39*, 353–373.

Bhat, N. D. R., J. M. Cordes, F. Camilo, D. J. Nice, and D. R. Lorimer (2004, April). Multifrequency Observations of Radio Pulse Broadening and Constraints on Interstellar Electron Density Microstructure. *The Astrophysical Journal 605*, 759–783.

Bhat, N. D. R., S. J. Tingay, and H. S. Knight (2008, April). Bright Giant Pulses from the Crab Nebula Pulsar: Statistical Properties, Pulse Broadening, and Scattering Due to the Nebula. *The Astrophysical Journal 676*, 1200–1209.

Bower, G. C., A. Deller, P. Demorest, A. Brunthaler, R. Eatough, H. Falcke, M. Kramer, K. J. Lee, and L. Spitler (2014, January). The Angular Broadening of the Galactic Center Pulsar SGR J1745-29: A New Constraint on the Scattering Medium. *The Astrophysical Journal letter 780*, L2.

Bracewell, R. N. (2000). *The Fourier transform and its applications*.

Burgay, M., B. C. Joshi, N. D'Amico, A. Possenti, A. G. Lyne, R. N. Manchester, M. A. McLaughlin, M. Kramer, F. Camilo, and P. C. C. Freire (2006, May). The Parkes High-Latitude pulsar survey. *Monthly Notices of the RAS 368*, 283–292.

Burke-Spolaor, S. and M. Bailes (2010, February). The millisecond radio sky: transients from a blind single-pulse search. *Monthly Notices of the RAS 402*, 855–866.

Burke-Spolaor, S., M. Bailes, R. Ekers, J.-P. Macquart, and F. Crawford, III (2011, January). Radio Bursts with Extragalactic Spectral Characteristics Show Terrestrial Origins. *The Astrophysical Journal 727*, 18.

Burke-Spolaor, S., M. Bailes, S. Johnston, S. D. Bates, N. D. R. Bhat, M. Burgay, N. D'Amico, A. Jameson, M. J. Keith, M. Kramer, L. Levin, S. Milia, A. Possenti, B. Stappers, and W. van Straten (2011, October). The High Time Resolution Universe Pulsar Survey - III. Single-pulse searches and preliminary analysis. *Monthly Notices of the RAS 416*, 2465–2476.

Burke-Spolaor, S. and K. W. Bannister (2014, July). The Galactic Position Dependence of Fast Radio Bursts and the Discovery of FRB 011025. *ArXiv e-prints*.

Camilo, F., S. M. Ransom, J. P. Halpern, J. Reynolds, D. J. Helfand, N. Zimmerman, and J. Sarkissian (2006, August). Transient pulsed radio emission from a magnetar. *Nature 442*, 892–895.

Chengalur, N. J., Y. Gupta, and S. K. Dwarakanath (2007, October). *Low frequency Radio Astronomy.*

Chennamangalam, J. and D. R. Lorimer (2014, May). The Galactic Centre pulsar population. *Monthly Notices of the RAS 440*, L86–L90.

Clarke, N., J.-P. Macquart, and C. Trott (2013, March). Performance of a Novel Fast Transients Detection System. *The Astrophysical Journals 205*, 4.

Cognard, I., J. A. Shrauner, J. H. Taylor, and S. E. Thorsett (1996, February). Giant Radio Pulses from a Millisecond Pulsar. *The Astrophysical Journal 457*, L81.

Cordes, J. M. (2013). Radio bursts, origin unknown. *Science 341*(6141), 40–41.

Cordes, J. M. and T. J. W. Lazio (2002, July). NE2001.I. A New Model for the Galactic Distribution of Free Electrons and its Fluctuations. *ArXiv Astrophysics e-prints*.

Cordes, J. M., T. J. W. Lazio, and M. A. McLaughlin (2004, December). The dynamic radio sky. *New Astronomy Review 48*, 1459–1472.

Cordes, J. M. and M. A. McLaughlin (2003, October). Searches for Fast Radio Transients. *The Astrophysical Journal 596*, 1142–1154.

Crawford, F., J. W. T. Hessels, and V. M. Kaspi (2007, June). Deep Searches for Radio Pulsations and Bursts from Four Southern Anomalous X-Ray Pulsars. *The Astrophysical Journal 662*, 1183–1187.

D'Addario, L. (2010, March). Searching For Dispersed Transient Pulses With ASKAP.

Deneva, J. S., J. M. Cordes, M. A. McLaughlin, D. J. Nice, D. R. Lorimer, F. Crawford, N. D. R. Bhat, F. Camilo, D. J. Champion, P. C. C. Freire, S. Edel, V. I. Kondratiev, J. W. T. Hessels, F. A. Jenet, L. Kasian, V. M. Kaspi, M. Kramer, P. Lazarus, S. M. Ransom, I. H. Stairs, B. W. Stappers, J. van Leeuwen, A. Brazier, A. Venkataraman, J. A. Zollweg, and S. Bogdanov (2009, October). Arecibo Pulsar Survey Using ALFA: Probing Radio Pulsar Intermittency And Transients. *The Astrophysical Journal 703*, 2259–2274.

Dessart, L., A. Burrows, E. Livne, and C. D. Ott (2008, January). The Proto-Neutron Star Phase of the Collapsar Model and the Route to Long-Soft Gamma-Ray Bursts and Hypernovae. *The Astrophysical Journal letter 673*, L43–L46.

Dessenne, C. A.-C., D. A. Green, P. J. Warner, D. J. Titterington, E. M. Waldram, S. D. Barthelmy, P. S. Butterworth, T. L. Cline, N. Gehrels, D. M. Palmer, G. J. Fishman, C. Kouveliotou, and C. A. Meegan (1996, August). Searches for prompt radio emission at 151 MHz from the gamma-ray bursts GRB 950430 and GRB 950706. *Monthly Notices of the RAS 281*, 977–984.

Dewdney, P., J. G. bijdeVaate, K. Cloete, A. Gunst, H. D., R. McCool, N. Roddis, and W. Turner (2010). SKA Memo Series.

Eatough, R. P., H. Falcke, R. Karuppusamy, K. J. Lee, D. J. Champion, E. F. Keane, G. Desvignes, D. H. F. M. Schnitzeler, L. G. Spitler, M. Kramer, B. Klein, C. Bassa, G. C. Bower, A. Brunthaler, I. Cognard, A. T. Deller, P. B. Demorest, P. C. C. Freire, A. Kraus, A. G. Lyne, A. Noutsos, B. Stappers, and N. Wex (2013, September). A strong magnetic field around the supermassive black hole at the centre of the Galaxy. *Nature 501*, 391–394.

Eatough, R. P., M. Kramer, B. Klein, R. Karuppusamy, D. J. Champion, P. C. C. Freire, N. Wex, and K. Liu (2013, March). Can we see pulsars around Sgr $A^{\star}$? The latest searches with the Effelsberg telescope. In J. van Leeuwen (Ed.), *IAU Symposium*, Volume 291 of *IAU Symposium*, pp. 382–384.

Edwards, R. T., M. Bailes, W. van Straten, and M. C. Britton (2001a, September). The Swinburne intermediate-latitude pulsar survey. *Monthly Notices of the RAS 326*, 358–374.

Edwards, R. T., M. Bailes, W. van Straten, and M. C. Britton (2001b, September). The Swinburne intermediate-latitude pulsar survey. *Monthly Notices of the RAS 326*, 358–374.

Etienne, Z. B., V. Paschalidis, and S. L. Shapiro (2012, October). General-relativistic simulations of black-hole-neutron-star mergers: Effects of tilted magnetic fields. *Physical Review D 86*(8), 084026.

Evans, P. A., A. P. Beardmore, K. L. Page, J. P. Osborne, P. T. O'Brien, R. Willingale, R. L. C. Starling, D. N. Burrows, O. Godet, L. Vetere, J. Racusin, M. R. Goad, K. Wiersema, L. Angelini, M. Capalbi, G. Chincarini, N. Gehrels, J. A. Kennea, R. Margutti, D. C. Morris, C. J. Mountford, C. Pagani, M. Perri, P. Romano, and N. Tanvir (2009, August). Methods and results of an automatic analysis of a complete sample of Swift-XRT observations of GRBs. *Monthly Notices of the RAS 397*, 1177–1201.

Falcke, H. and L. Rezzolla (2013, July). Fast radio bursts: the last sign of supramassive neutron stars. *ArXiv e-prints*.

Fan, Y.-Z., Y.-W. Yu, D. Xu, Z.-P. Jin, X.-F. Wu, D.-M. Wei, and B. Zhang (2013, December). A Supramassive Magnetar Central Engine for GRB 130603B. *The Astrophysical Journal letter 779*, L25.

Figer, D. F. (2008, June). Young Massive Clusters. In F. Bresolin, P. A. Crowther, and J. Puls (Eds.), *IAU Symposium*, Volume 250 of *IAU Symposium*, pp. 247–256.

Figer, D. F. (2009). *Massive-star formation in the Galactic center:*, pp. 40–59.

Fridman, P. A. (2008, May). Statistically Stable Estimates of Variance in Radio-Astronomy Observations as Tools for Radio-Frequency Interference Mitigation. *Astronomical Journal 135*, 1810–1824.

Gao, H., W.-H. Lei, Y.-C. Zou, X.-F. Wu, and B. Zhang (2013, December). A complete reference of the analytical synchrotron external shock models of gamma-ray bursts. *New Astronomy Review 57*, 141–190.

Gehrels, N., G. Chincarini, P. Giommi, K. O. Mason, J. A. Nousek, A. A. Wells, N. E. White, S. D. Barthelmy, D. N. Burrows, L. R. Cominsky, K. C. Hurley, F. E. Marshall, P. Mészáros, P. W. A. Roming, L. Angelini, L. M. Barbier, T. Belloni, S. Campana, P. A. Caraveo, M. M. Chester, O. Citterio, T. L. Cline, M. S. Cropper, J. R. Cummings, A. J. Dean, E. D. Feigelson, E. E. Fenimore, D. A. Frail, A. S. Fruchter, G. P. Garmire, K. Gendreau, G. Ghisellini, J. Greiner, J. E. Hill, S. D. Hunsberger, H. A. Krimm, S. R. Kulkarni, P. Kumar, F. Lebrun, N. M. Lloyd-Ronning, C. B. Markwardt, B. J. Mattson, R. F. Mushotzky, J. P. Norris, J. Osborne, B. Paczynski, D. M. Palmer, H.-S. Park, A. M. Parsons, J. Paul, M. J. Rees, C. S. Reynolds, J. E. Rhoads, T. P. Sasseen, B. E. Schaefer, A. T. Short, A. P. Smale, I. A. Smith, L. Stella, G. Tagliaferri, T. Takahashi, M. Tashiro, L. K. Townsley, J. Tueller, M. J. L. Turner, M. Vietri, W. Voges, M. J. Ward, R. Willingale, F. M. Zerbi, and W. W. Zhang (2004, August). The Swift Gamma-Ray Burst Mission. *The Astrophysical Journal 611*, 1005–1020.

Gehrels, N., E. Ramirez-Ruiz, and D. B. Fox (2009, September). Gamma-Ray Bursts in the Swift Era. *47*, 567–617.

Genzel, R., F. Eisenhauer, and S. Gillessen (2010, October). The Galactic Center massive black hole and nuclear star cluster. *Reviews of Modern Physics 82*, 3121–3195.

Ghirlanda, G., G. Ghisellini, and C. Firmani (2006, July). Gamma-ray bursts as standard candles to constrain the cosmological parameters. *New Journal of Physics 8*, 123.

Giacomazzo, B. and R. Perna (2013, July). Formation of Stable Magnetars from Binary Neutron Star Mergers. *The Astrophysical Journal letter 771*, L26.

Goldsmith, P. F. (2002, December). Radio Telescopes and Measurements at Radio Wavelengths. In S. Stanimirovic, D. Altschuler, P. Goldsmith, and C. Salter (Eds.), *Single-Dish Radio Astronomy: Techniques and Applications*, Volume 278 of *Astronomical Society of the Pacific Conference Series*, pp. 45–79.

Hankins, T. H. and J. A. Eilek (2007, November). Radio Emission Signatures in the Crab Pulsar. *The Astrophysical Journal 670*, 693–701.

Hankins, T. H. and B. J. Rickett (1975). Pulsar signal processing. *Methods in Computational Physics 14*, 55–129.

Hewish, A., S. J. Bell, J. D. H. Pilkington, P. F. Scott, and R. A. Collins (1968, February). Observation of a Rapidly Pulsating Radio Source. *Nature 217*, 709–713.

Huynh, M. and J. Lazio (2013, November). An Overview of the Square Kilometre Array. *ArXiv e-prints*.

Ioka, K. (2003, December). The Cosmic Dispersion Measure from Gamma-Ray Burst Afterglows: Probing the Reionization History and the Burst Environment. *The Astrophysical Journal letter 598*, L79–L82.

Jacoby, B. A., M. Bailes, S. M. Ord, R. T. Edwards, and S. R. Kulkarni (2009a, July). A Large-Area Survey for Radio Pulsars at High Galactic Latitudes. *The Astrophysical Journal 699*, 2009–2016.

Jacoby, B. A., M. Bailes, S. M. Ord, R. T. Edwards, and S. R. Kulkarni (2009b, July). A Large-Area Survey for Radio Pulsars at High Galactic Latitudes. *The Astrophysical Journal 699*, 2009–2016.

Johnson, J. B. (1928, Jul). Thermal agitation of electricity in conductors. *Phys. Rev. 32*, 97–109.

Kay, M. S. (1998). *Fundamentals of Statistical signal processing detection theory.*

Keane, E. F., D. A. Ludovici, R. P. Eatough, M. Kramer, A. G. Lyne, M. A. McLaughlin, and B. W. Stappers (2010, January). Further searches for Rotating Radio Transients in the Parkes Multi-beam Pulsar Survey. *Monthly Notices of the RAS 401*, 1057–1068.

Keane, E. F., B. W. Stappers, M. Kramer, and A. G. Lyne (2012, September). On the origin of a highly dispersed coherent radio burst. *Monthly Notices of the RAS 425*, L71–L75.

Klebesadel, R. W., I. B. Strong, and R. A. Olson (1973, June). Observations of Gamma-Ray Bursts of Cosmic Origin. In *Bulletin of the American Astronomical Society*, Volume 5 of *Bulletin of the American Astronomical Society*, pp. 322.

Kocz, J., F. H. Briggs, and J. Reynolds (2010, December). Radio Frequency Interference Removal through the Application of Spatial Filtering Techniques on the Parkes Multibeam Receiver. *Astronomical Journal 140*, 2086–2094.

Kouveliotou, C., C. A. Meegan, G. J. Fishman, N. P. Bhat, M. S. Briggs, T. M. Koshut, W. S. Paciesas, and G. N. Pendleton (1993, August). Identification of two classes of gamma-ray bursts. *The Astrophysical Journal letter 413*, L101–L104.

Kraus, D. J. (1988). *Radio Astronomy*.

Lazio, T. J. W. and J. M. Cordes (1998, November). Galactic Center 6 and 20cm survey (Lazio+, 1998). *VizieR Online Data Catalog 211*, 80201.

Lei, W.-H., B. Zhang, and E.-W. Liang (2013, March). Hyperaccreting Black Hole as Gamma-Ray Burst Central Engine. I. Baryon Loading in Gamma-Ray Burst Jets. *The Astrophysical Journal 765*, 125.

Leshem, A., A.-J. van der Veen, and A.-J. Boonstra (2000, November). Multichannel Interference Mitigation Techniques in Radio Astronomy. *The Astrophysical Journals 131*, 355–373.

Lorimer, D. R., M. Bailes, M. A. McLaughlin, D. J. Narkevic, and F. Crawford (2007, November). A Bright Millisecond Radio Burst of Extragalactic Origin. *Science 318*, 777–.

Lorimer, D. R. and M. Kramer (2012, October). *Handbook of Pulsar Astronomy*.

Lundgren, S. C., J. M. Cordes, M. Ulmer, S. M. Matz, S. Lomatch, R. S. Foster, and T. Hankins (1995, November). Giant Pulses from the Crab Pulsar: A Joint Radio and Gamma-Ray Study. *The Astrophysical Journal 453*, 433.

Macquart, J.-P. (2007, March). On the Detectability of Prompt Coherent Gamma-Ray Burst Radio Emission. *The Astrophysical Journal letter 658*, L1–L4.

Macquart, J.-P. (2011, June). Detection Rates for Surveys for Fast Transients with Next Generation Radio Arrays. *The Astrophysical Journal 734*, 20.

Macquart, J.-P., N. Kanekar, D. A. Frail, and S. M. Ransom (2010, June). A High-frequency Search for Pulsars within the Central Parsec of Sgr A*. *The Astrophysical Journal 715*, 939–946.

Macquart, J.-P. and J. Y. Koay (2013, October). Temporal Smearing of Transient Radio Sources by the Intergalactic Medium. *The Astrophysical Journal 776*, 125.

Manchester, R. N., G. Fan, A. G. Lyne, V. M. Kaspi, and F. Crawford (2006, September). Discovery of 14 Radio Pulsars in a Survey of the Magellanic Clouds. *The Astrophysical Journal 649*, 235–242.

Manchester, R. N., G. B. Hobbs, A. Teoh, and M. Hobbs (2005, August). ATNF Pulsar Catalog (Manchester+, 2005). *VizieR Online Data Catalog 7245*, 0.

Manchester, R. N., A. G. Lyne, F. Camilo, J. F. Bell, V. M. Kaspi, N. D'Amico, N. P. F. McKay, F. Crawford, I. H. Stairs, A. Possenti, M. Kramer, and D. C. Sheppard (2001, November). The Parkes multi-beam pulsar survey - I. Observing and data analysis systems, discovery and timing of 100 pulsars. *Monthly Notices of the RAS 328*, 17–35.

McLaughlin, M. A., A. G. Lyne, D. R. Lorimer, M. Kramer, A. J. Faulkner, R. N. Manchester, J. M. Cordes, F. Camilo, A. Possenti, I. H. Stairs, G. Hobbs, N. D'Amico, M. Burgay, and J. T. O'Brien (2006, February). Transient radio bursts from rotating neutron stars. *Nature 439*, 817–820.

Metzger, B. D., D. Giannios, T. A. Thompson, N. Bucciantini, and E. Quataert (2011, May). The protomagnetar model for gamma-ray bursts. *Monthly Notices of the RAS 413*, 2031–2056.

Metzger, B. D., A. L. Piro, and E. Quataert (2008, October). Time-dependent models of accretion discs formed from compact object mergers. *Monthly Notices of the RAS 390*, 781–797.

Napier, P. J., D. S. Bagri, B. G. Clark, A. E. E. Rogers, J. D. Romney, A. R. Thompson, and R. C. Walker (1994, May). The Very Long Baseline Array. *IEEE Proceedings 82*, 658–672.

Narayan, R., T. Piran, and P. Kumar (2001, August). Accretion Models of Gamma-Ray Bursts. *The Astrophysical Journal 557*, 949–957.

Nousek, J. A., C. Kouveliotou, D. Grupe, K. L. Page, J. Granot, E. Ramirez-Ruiz, S. K. Patel, D. N. Burrows, V. Mangano, S. Barthelmy, A. P. Beardmore, S. Campana, M. Capalbi, G. Chincarini, G. Cusumano, A. D. Falcone, N. Gehrels, P. Giommi, M. R. Goad, O. Godet, C. P. Hurkett, J. A. Kennea,

A. Moretti, P. T. O'Brien, J. P. Osborne, P. Romano, G. Tagliaferri, and A. A. Wells (2006, May). Evidence for a Canonical Gamma-Ray Burst Afterglow Light Curve in the Swift XRT Data. *The Astrophysical Journal 642*, 389–400.

Obenberger, K. S., J. M. Hartman, G. B. Taylor, J. Craig, J. Dowell, J. F. Helmboldt, P. A. Henning, F. K. Schinzel, and T. L. Wilson (2014, April). Limits on Gamma-Ray Burst Prompt Radio Emission Using the LWA1. *The Astrophysical Journal 785*, 27.

O'Brien, P. T., R. Willingale, J. Osborne, M. R. Goad, K. L. Page, S. Vaughan, E. Rol, A. Beardmore, O. Godet, C. P. Hurkett, A. Wells, B. Zhang, S. Kobayashi, D. N. Burrows, J. A. Nousek, J. A. Kennea, A. Falcone, D. Grupe, N. Gehrels, S. Barthelmy, J. Cannizzo, J. Cummings, J. E. Hill, H. Krimm, G. Chincarini, G. Tagliaferri, S. Campana, A. Moretti, P. Giommi, M. Perri, V. Mangano, and V. LaParola (2006, August). The Early X-Ray Emission from GRBs. *The Astrophysical Journal 647*, 1213–1237.

O'Neil, K. (2002, December). Single-Dish Calibration Techniques at Radio Wavelengths. In S. Stanimirovic, D. Altschuler, P. Goldsmith, and C. Salter (Eds.), *Single-Dish Radio Astronomy: Techniques and Applications*, Volume 278 of *Astronomical Society of the Pacific Conference Series*, pp. 293–311.

Oppenheim, A. V., R. W. Schafer, and J. R. Buck (1999). *Disceret-Time Signal Processing* .

Palmer, D. M. (1993, November). Radio Dispersion as a Diagnostic of Gamma-Ray Burst Distances. *The Astrophysical Journal letter 417*, L25.

Perley, R. A., C. J. Chandler, B. J. Butler, and J. M. Wrobel (2011, September). The Expanded Very Large Array: A New Telescope for New Science. *The Astrophysical Journal letter 739*, L1.

Pfahl, E. and A. Loeb (2004, November). Probing the Spacetime around Sagittarius A* with Radio Pulsars. *The Astrophysical Journal 615*, 253–258.

Phillips, C., T. Tzioumis, S. Tingay, J. Stevens, J. Lovell, S. Amy, C. West, and R. Dodson (2009). LBADR: The LBA Data Recorder. In *8th International e-VLBI Workshop*.

Popham, R., S. E. Woosley, and C. Fryer (1999, June). Hyperaccreting Black Holes and Gamma-Ray Bursts. *The Astrophysical Journal 518*, 356–374.

Popov, S. B. and K. A. Postnov (2007, October). Hyperflares of SGRs as an engine for millisecond extragalactic radio bursts. *ArXiv e-prints*.

Readhead, A. C. S. (1994, May). Equipartition brightness temperature and the inverse Compton catastrophe. *The Astrophysical Journal 426*, 51–59.

Rees, M. J. and P. Meszaros (1994, August). Unsteady outflow models for cosmological gamma-ray bursts. *The Astrophysical Journal letter 430*, L93–L96.

Rezzolla, L., L. Baiotti, B. Giacomazzo, D. Link, and J. A. Font (2010, June). Accurate evolutions of unequal-mass neutron-star binaries: properties of the torus and short GRB engines. *Classical and Quantum Gravity 27*(11), 114105.

Rezzolla, L., B. Giacomazzo, L. Baiotti, J. Granot, C. Kouveliotou, and M. A. Aloy (2011, May). The Missing Link: Merging Neutron Stars Naturally Produce Jet-like Structures and Can Power Short Gamma-ray Bursts. *The Astrophysical Journal letter 732*, L6.

Richards, M. T., E. B. Waltman, F. D. Ghigo, and D. S. P. Richards (2003, August). Statistical Analysis of 5 Year Continuous Radio Flare Data from β Persei, V711 Tauri, δ Librae, and UX Arietis. *The Astrophysical Journals 147*, 337–361.

Ritakari, J. and A. Mujunen (2004, June). Gbit/s VLBI and eVLBI with Off-The-Shelf Components. In N. R. Vandenberg and K. D. Baver (Eds.), *International VLBI Service for Geodesy and Astrometry 2004 General Meeting Proceedings*, pp. 182.

Roberts, M. S. E., J. W. T. Hessels, S. M. Ransom, V. M. Kaspi, P. C. C. Freire, F. Crawford, and D. R. Lorimer (2002, September). PSR J2021+3651: A Young Radio Pulsar Coincident with an Unidentified EGRET γ-Ray Source. *The Astrophysical Journal 577*, L19–L22.

Romani, R. W. and S. Johnston (2001, August). Giant Pulses from the Millisecond Pulsar B1821-24. *The Astrophysical Journal letter 557*, L93–L96.

Rowlinson, A., P. T. O'Brien, N. R. Tanvir, B. Zhang, P. A. Evans, N. Lyons, A. J. Levan, R. Willingale, K. L. Page, O. Onal, D. N. Burrows, A. P. Beardmore, T. N. Ukwatta, E. Berger, J. Hjorth, A. S. Fruchter, R. L. Tunnicliffe, D. B. Fox, and A. Cucchiara (2010, December). The unusual X-ray emission of the

short Swift GRB 090515: evidence for the formation of a magnetar? *Monthly Notices of the RAS 409*, 531–540.

Roy, S. (2013, August). Density of Warm Ionized Gas near the Galactic Center: Low Radio Frequency Observations. *The Astrophysical Journal 773*, 67.

Shitov, Y. P., A. D. Kuzmin, D. V. Dumskii, and B. Y. Losovsky (2009, June). Detection of the new rotating radio transient pulsar PSR J2225+35. *Astronomy Reports 53*, 561–563.

Spitler, L. G., J. M. Cordes, J. W. T. Hessels, D. R. Lorimer, M. A. McLaughlin, S. Chatterjee, F. Crawford, J. S. Deneva, V. M. Kaspi, R. S. Wharton, B. Allen, S. Bogdanov, A. Brazier, F. Camilo, P. C. C. Freire, F. A. Jenet, C. Karako-Argaman, B. Knispel, P. Lazarus, K. J. Lee, J. van Leeuwen, R. Lynch, A. G. Lyne, S. M. Ransom, P. Scholz, X. Siemens, I. H. Stairs, K. Stovall, J. K. Swiggum, A. Venkataraman, W. W. Zhu, C. Aulbert, and H. Fehrmann (2014, April). Fast Radio Burst Discovered in the Arecibo Pulsar ALFA Survey. *ArXiv e-prints*.

Spitler, L. G., K. J. Lee, R. P. Eatough, M. Kramer, R. Karuppusamy, C. G. Bassa, I. Cognard, G. Desvignes, A. G. Lyne, B. W. Stappers, G. C. Bower, J. M. Cordes, D. J. Champion, and H. Falcke (2014, January). Pulse Broadening Measurements from the Galactic Center Pulsar J1745-2900. *The Astrophysical Journal letter 780*, L3.

Staley, T. D., D. J. Titterington, R. P. Fender, J. D. Swinbank, A. J. van der Horst, A. Rowlinson, A. M. M. Scaife, K. J. B. Grainge, and G. G. Pooley (2013, February). Automated rapid follow-up of Swift gamma-ray burst alerts at 15 GHz with the AMI Large Array. *Monthly Notices of the RAS 428*, 3114–3120.

Stanimirovic, S., D. Altschuler, P. Goldsmith, and C. Salter (Eds.) (2002, December). *Single-Dish Radio Astronomy: Techniques and Applications*, Volume 278 of *Astronomical Society of the Pacific Conference Series*.

Stankiewicz, R. (2010, April). The Very Long Baseline Array (VLBA). *Journal of the RAS of Canada 104*, 71.

Staveley-Smith, L., W. E. Wilson, T. S. Bird, M. J. Disney, R. D. Ekers, K. C. Freeman, R. F. Haynes, M. W. Sinclair, R. A. Vaile, R. L. Webster, and A. E.

Wright (1996, November). The Parkes 21 CM multibeam receiver. *Publications of the Astronomical Society of Australia 13*, 243–248.

Tavani, M., G. Barbiellini, A. Argan, F. Boffelli, A. Bulgarelli, P. Caraveo, P. W. Cattaneo, A. W. Chen, V. Cocco, E. Costa, F. D'Ammando, E. Del Monte, G. de Paris, G. Di Cocco, G. di Persio, I. Donnarumma, Y. Evangelista, M. Feroci, A. Ferrari, M. Fiorini, F. Fornari, F. Fuschino, T. Froysland, M. Frutti, M. Galli, F. Gianotti, A. Giuliani, C. Labanti, I. Lapshov, F. Lazzarotto, F. Liello, P. Lipari, F. Longo, E. Mattaini, M. Marisaldi, M. Mastropietro, A. Mauri, F. Mauri, S. Mereghetti, E. Morelli, A. Morselli, L. Pacciani, A. Pellizzoni, F. Perotti, G. Piano, P. Picozza, C. Pontoni, G. Porrovecchio, M. Prest, G. Pucella, M. Rapisarda, A. Rappoldi, E. Rossi, A. Rubini, P. Soffitta, A. Traci, M. Trifoglio, A. Trois, E. Vallazza, S. Vercellone, V. Vittorini, A. Zambra, D. Zanello, C. Pittori, B. Preger, P. Santolamazza, F. Verrecchia, P. Giommi, S. Colafrancesco, A. Antonelli, S. Cutini, D. Gasparrini, S. Stellato, G. Fanari, R. Primavera, F. Tamburelli, F. Viola, G. Guarrera, L. Salotti, F. D'Amico, E. Marchetti, M. Crisconio, P. Sabatini, G. Annoni, S. Alia, A. Longoni, R. Sanquerin, M. Battilana, P. Concari, E. Dessimone, R. Grossi, A. Parise, F. Monzani, E. Artina, R. Pavesi, G. Marseguerra, L. Nicolini, L. Scandelli, L. Soli, V. Vettorello, E. Zardetto, A. Bonati, L. Maltecca, E. D'Alba, M. Patané, G. Babini, F. Onorati, L. Acquaroli, M. Angelucci, B. Morelli, C. Agostara, M. Cerone, A. Michetti, P. Tempesta, S. D'Eramo, F. Rocca, F. Giannini, G. Borghi, B. Garavelli, M. Conte, M. Balasini, I. Ferrario, M. Vanotti, E. Collavo, and M. Giacomazzo (2009, August). The AGILE Mission. *Astronomy and Astrophysics 502*, 995–1013.

Taylor, J. H. (1974, June). A Sensitive Method for Detecting Dispersed Radio Emission. *Astronomy and Astrophysicss 15*, 367.

Thompson, A. R., J. M. Moran, and G. W. Swenson, Jr. (2001). *Interferometry and Synthesis in Radio Astronomy, 2nd Edition*.

Thornton, D., B. Stappers, M. Bailes, B. Barsdell, S. Bates, N. D. R. Bhat, M. Burgay, S. Burke-Spolaor, D. J. Champion, P. Coster, N. D'Amico, A. Jameson, S. Johnston, M. Keith, M. Kramer, L. Levin, S. Milia, C. Ng, A. Possenti, and W. van Straten (2013, July). A Population of Fast Radio Bursts at Cosmological Distances. *Science 341*, 53–56.

Tingay, S. J., R. Goeke, J. D. Bowman, D. Emrich, S. M. Ord, D. A. Mitchell,

M. F. Morales, T. Booler, B. Crosse, R. B. Wayth, C. J. Lonsdale, S. Tremblay, D. Pallot, T. Colegate, A. Wicenec, N. Kudryavtseva, W. Arcus, D. Barnes, G. Bernardi, F. Briggs, S. Burns, J. D. Bunton, R. J. Cappallo, B. E. Corey, A. Deshpande, L. Desouza, B. M. Gaensler, L. J. Greenhill, P. J. Hall, B. J. Hazelton, D. Herne, J. N. Hewitt, M. Johnston-Hollitt, D. L. Kaplan, J. C. Kasper, B. B. Kincaid, R. Koenig, E. Kratzenberg, M. J. Lynch, B. Mckinley, S. R. Mcwhirter, E. Morgan, D. Oberoi, J. Pathikulangara, T. Prabu, R. A. Remillard, A. E. E. Rogers, A. Roshi, J. E. Salah, R. J. Sault, N. Udaya-Shankar, F. Schlagenhaufer, K. S. Srivani, J. Stevens, R. Subrahmanyan, M. Waterson, R. L. Webster, A. R. Whitney, A. Williams, C. L. Williams, and J. S. B. Wyithe (2013, January). The Murchison Widefield Array: The Square Kilometre Array Precursor at Low Radio Frequencies. *Publications of the ASA 30*, 7.

Totani, T. (2013, October). Cosmological Fast Radio Bursts from Binary Neutron Star Mergers. *Publications of the ASJ 65*, L12.

Trott, C. M., S. J. Tingay, R. B. Wayth, D. R. Thompson, A. T. Deller, W. F. Brisken, K. L. Wagstaff, W. A. Majid, S. Burke-Spolaor, J.-P. R. Macquart, and D. Palaniswamy (2013, April). A Framework for Interpreting Fast Radio Transients Search Experiments: Application to the V-FASTR Experiment. *The Astrophysical Journal 767*, 4.

Usov, V. V. (1992, June). Millisecond pulsars with extremely strong magnetic fields as a cosmological source of gamma-ray bursts. *Nature 357*, 472–474.

Usov, V. V. and J. I. Katz (2000, December). Low frequency radio pulses from gamma-ray bursts? *Astronomy and Astrophysics 364*, 655–659.

van Haarlem, M. P., M. W. Wise, A. W. Gunst, G. Heald, J. P. McKean, J. W. T. Hessels, A. G. de Bruyn, R. Nijboer, J. Swinbank, R. Fallows, M. Brentjens, A. Nelles, R. Beck, H. Falcke, R. Fender, J. Hörandel, L. V. E. Koopmans, G. Mann, G. Miley, H. Röttgering, B. W. Stappers, R. A. M. J. Wijers, S. Zaroubi, M. van den Akker, A. Alexov, J. Anderson, K. Anderson, A. van Ardenne, M. Arts, A. Asgekar, I. M. Avruch, F. Batejat, L. Bähren, M. E. Bell, M. R. Bell, I. van Bemmel, P. Bennema, M. J. Bentum, G. Bernardi, P. Best, L. Bîrzan, A. Bonafede, A.-J. Boonstra, R. Braun, J. Bregman, F. Breitling, R. H. van de Brink, J. Broderick, P. C. Broekema, W. N. Brouw, M. Brüggen, H. R. Butcher, W. van Cappellen, B. Ciardi, T. Coenen, J. Conway, A. Coolen,

A. Corstanje, S. Damstra, O. Davies, A. T. Deller, R.-J. Dettmar, G. van Diepen, K. Dijkstra, P. Donker, A. Doorduin, J. Dromer, M. Drost, A. van Duin, J. Eislöffel, J. van Enst, C. Ferrari, W. Frieswijk, H. Gankema, M. A. Garrett, F. de Gasperin, M. Gerbers, E. de Geus, J.-M. Grießmeier, T. Grit, P. Gruppen, J. P. Hamaker, T. Hassall, M. Hoeft, H. Holties, A. Horneffer, A. van der Horst, A. van Houwelingen, A. Huijgen, M. Iacobelli, H. Intema, N. Jackson, V. Jelic, A. de Jong, E. Juette, D. Kant, A. Karastergiou, A. Koers, H. Kollen, V. I. Kondratiev, E. Kooistra, Y. Koopman, A. Koster, M. Kuniyoshi, M. Kramer, G. Kuper, P. Lambropoulos, C. Law, J. van Leeuwen, J. Lemaitre, M. Loose, P. Maat, G. Macario, S. Markoff, J. Masters, D. McKay-Bukowski, H. Meijering, H. Meulman, M. Mevius, E. Middelberg, R. Millenaar, J. C. A. Miller-Jones, R. N. Mohan, J. D. Mol, J. Morawietz, R. Morganti, D. D. Mulcahy, E. Mulder, H. Munk, L. Nieuwenhuis, R. van Nieuwpoort, J. E. Noordam, M. Norden, A. Noutsos, A. R. Offringa, H. Olofsson, A. Omar, E. Orrú, R. Overeem, H. Paas, M. Pandey-Pommier, V. N. Pandey, R. Pizzo, A. Polatidis, D. Rafferty, S. Rawlings, W. Reich, J.-P. de Reijer, J. Reitsma, A. Renting, P. Riemers, E. Rol, J. W. Romein, J. Roosjen, M. Ruiter, A. Scaife, K. van der Schaaf, B. Scheers, P. Schellart, A. Schoenmakers, G. Schoonderbeek, M. Serylak, A. Shulevski, J. Sluman, O. Smirnov, C. Sobey, H. Spreeuw, M. Steinmetz, C. G. M. Sterks, H.-J. Stiepel, K. Stuurwold, M. Tagger, Y. Tang, C. Tasse, I. Thomas, S. Thoudam, M. C. Toribio, B. van der Tol, O. Usov, M. van Veelen, A.-J. van der Veen, S. ter Veen, J. P. W. Verbiest, R. Vermeulen, N. Vermaas, C. Vocks, C. Vogt, M. de Vos, E. van der Wal, R. van Weeren, H. Weggemans, P. Weltevrede, S. White, S. J. Wijnholds, T. Wilhelmsson, O. Wucknitz, S. Yatawatta, P. Zarka, A. Zensus, and J. van Zwieten (2013, May). LOFAR: The LOw-Frequency ARray. *ArXiv e-prints*.

Verheijen, M. A. W., T. A. Oosterloo, W. A. van Cappellen, L. Bakker, M. V. Ivashina, and J. M. van der Hulst (2008, August). Apertif, a focal plane array for the WSRT. In R. Minchin and E. Momjian (Eds.), *The Evolution of Galaxies Through the Neutral Hydrogen Window*, Volume 1035 of *American Institute of Physics Conference Series*, pp. 265–271.

Wayth, R. B., W. F. Brisken, A. T. Deller, W. A. Majid, D. R. Thompson, S. J. Tingay, and K. L. Wagstaff (2011, July). V-FASTR: The VLBA Fast Radio Transients Experiment. *The Astrophysical Journal 735*, 97.

Weber, R., C. Faye, F. Biraud, and J. Dansou (1997, November). Spectral detec-

tor for interference time blanking using quantized correlator. *Astronomy and Astrophysicss 126*, 161–167.

Weiler, K. W., N. Panagia, R. A. Sramek, S. D. Van Dyk, C. J. Stockdale, and C. L. Williams (2010). Radio emission from supernovae. *Mem. Societa Astronomica Italiana 81*, 374.

Wharton, R. S., S. Chatterjee, J. M. Cordes, J. S. Deneva, and T. J. W. Lazio (2012, July). Multiwavelength Constraints on Pulsar Populations in the Galactic Center. *The Astrophysical Journal 753*, 108.

Winkler, C., T. J.-L. Courvoisier, G. Di Cocco, N. Gehrels, A. Giménez, S. Grebenev, W. Hermsen, J. M. Mas-Hesse, F. Lebrun, N. Lund, G. G. C. Palumbo, J. Paul, J.-P. Roques, H. Schnopper, V. Schönfelder, R. Sunyaev, B. Teegarden, P. Ubertini, G. Vedrenne, and A. J. Dean (2003, November). The INTEGRAL mission. *Astronomy and Astrophysics 411*, L1–L6.

Woosley, S. E. and A. I. MacFadyen (1999, September). Central engines for gamma-ray bursts. *Astronomy and Astrophysicss 138*, 499–502.

Zhang, B. (2013, October). A possible connection between Fast Radio Bursts and Gamma-Ray Bursts. *ArXiv e-prints*.

Zhang, B. (2014, January). A Possible Connection between Fast Radio Bursts and Gamma-Ray Bursts. *The Astrophysical Journal letter 780*, L21.

Zhang, B., Y. Z. Fan, J. Dyks, S. Kobayashi, P. Mészáros, D. N. Burrows, J. A. Nousek, and N. Gehrels (2006, May). Physical Processes Shaping Gamma-Ray Burst X-Ray Afterglow Light Curves: Theoretical Implications from the Swift X-Ray Telescope Observations. *The Astrophysical Journal 642*, 354–370.